TORQUE PULSATIONS MINIMIZATION IN PM SYNCHRONOUS MOTOR DRIVE

QIAN WEIZHE

B. Eng.

A THESIS SUBMITTED

FOR THE DEGREE OF MASTER OF ENGINEERING

DEPARTMENT OF ELECTRICAL & COMPUTER ENGINEERING

NATIONAL UNIVERSITY OF SINGAPORE

2004

Acknowledgments

First of all, I would like to express my most sincere appreciation and thanks to my supervisor, Prof. Sanjib Kumar Panda, for his guidance and constant encouragement throughout my two years of postgraduate studies. Prof. Panda's wide knowledge and experience in motor drives, and his helpfulness, have made my research work a very pleasant and fulfilling one. I am also grateful and obliged to my co-supervisor, Prof. Jian-Xin Xu, for providing me with many intellectual, innovative insights and suggestions throughout the course of my work. I am highly impressed by his breadth and depth of knowledge and clarity of concepts in almost every area of classical as well as modern control theory.

In addition, I would like to express my appreciation to the laboratory technologists, Mr. Y. C. Woo and Mr. M. Chandra, without whom this research work would have been so much harder to complete.

Many thanks to my colleagues in the EEM Lab - Liu Qinghua, Dong Jing, Wu Mei, Xi Yunxia, Zhang Yanfeng, Shi Chunming, Anshuman Tripathi and S. K. Sahoo, who have made my two years' of research work in this lab a very pleasant one.

Finally, I would like to express my most heartfelt thanks and gratitude to my family, who have always provided me with constant support, concern and prayers.

Contents

Acknowledgement **i**

Summary **vi**

Nomenclature **xi**

List of Figures **xiv**

List of Tables **xx**

1 Introduction **1**

1.1 Electric Drives 1

1.1.1 DC motors 3

1.1.2 AC motors 5

1.1.3 Switched reluctance motors 8

1.2 Description of PMAC Motors 9

1.2.1 Brushless DC motors (BLDCMs) 9

1.2.2 Permanent Magnet Synchronous Motors (PMSMs) 11

1.3 Pulsating Torque in the PMSM 13

1.4 Literature Survey on the Pulsating Torque Minimization Techniques in PMSM 14

1.4.1 Motor design techniques for pulsating torque minimization . 15

1.4.2 Control techniques for pulsating torque minimization 17

1.4.2.1 Pre-programmed stator current control 17

1.4.2.2 Feedback compensation schemes 19
1.4.2.3 Estimators and observers 21
1.5 Scope of the thesis 25

2 Modelling of the PMSM **27**
2.1 Introduction 27
2.2 Machine Equations in the *a*-*b*-*c* Frame 28
2.3 Machine Equations in the *d*-*q* Frame 34
2.4 Modelling of Pulsating Torque 38
2.4.1 Cogging torque 38
2.4.2 Torque ripple due to back-emf harmonics 40
2.4.3 Torque ripple due to dc offset current error 42
2.4.4 Torque ripple due to current scaling error 44
2.5 Conclusion 45

3 Application of LVSC and FILC for Pulsating Torque Minimization in PMSM **47**
3.1 Introduction 47
3.2 The Basic Iterative Learning Control 48
3.3 Configuration and Application of LVSC 53
3.3.1 Problem formulation and LVSC configuration 54
3.3.1.1 Problem formulation 54
3.3.1.2 LVSC configuration 56
3.3.1.3 Fourier series based iterative learning 57
3.3.2 Application of LVSC on the PMSM drive system 60
3.3.2.1 Torque control with LVSC pulsating torque compensation scheme 60

3.3.2.2 Closed-loop PI speed control with LVSC speed ripple compensation 63
3.4 Configuration and Application of FILC 65
3.4.1 FILC algorithm 65
3.4.2 Application of FILC on the PMSM Drive System 66
3.4.2.1 Torque control scheme with FILC pulsating torque compensation 67
3.4.2.2 Closed-loop PI speed control with FILC speed ripple compensation 69
3.5 A High Gain Torque Estimator 71
3.6 Conclusion 74

4 Simulation Results **76**
4.1 Introduction 76
4.2 Simulation Results 78
4.2.1 LVSC pulsating torque compensation scheme 78
4.2.2 LVSC speed ripple compensation scheme 84
4.2.3 FILC pulsating torque compensation scheme 88
4.2.4 FILC speed ripple compensation scheme 92
4.2.5 High gain torque estimator 96
4.3 Conclusion 99

5 Hardware and Software Implementation of the DSP-based PMSM Drive System **101**
5.1 Introduction 101
5.2 Overview of the Drive Implementation 102
5.3 System Hardware 103
5.3.1 DS1102 controller board 103

5.3.2 PWM inverter 104
5.3.3 Integrated interface platform 104
5.3.3.1 Inverter Control Card 105
5.3.3.2 Encoder Interface Card 106
5.3.3.3 Digital I/O and Absolute Encoder Card 107
5.3.3.4 Current Feedback Card 107
5.3.3.5 Torque/Analog Feedback Card 107
5.3.4 Current sensors 108
5.3.5 Loading system 108
5.3.6 Torque transducer 109
5.4 Software Environment 110
5.5 Control Program Algorithm 111
5.6 Conclusion 112

6 Experimental Results 115

6.1 Introduction 115
6.2 LVSC Compensation Schemes 116
6.2.1 LVSC pulsating torque compensation scheme with feedback signals from a torque transducer 116
6.2.2 LVSC pulsating torque compensation scheme with feedback signals obtained from torque estimator 121
6.2.3 LVSC speed ripple compensation scheme 125
6.3 FILC Compensation Schemes 129
6.3.1 FILC pulsating torque compensation scheme with feedback signals obtained from a torque transducer 130
6.3.2 FILC pulsating torque compensation scheme with feedback signals obtained from torque estimator 135
6.3.3 FILC speed ripple compensation scheme 137

6.4 Torque Pulsations Induced by the Load 144
6.5 Conclusion 147

7 Extended Summary and Conclusions **149**
7.1 Conclusions 149
7.2 Future Work 153

Reference **155**

Publications **168**

A Motor Ratings and Parameters **170**

B Architecture of DS1102 **172**

C Inverter **174**

D Interface Platform **176**

E Current Sensor **178**

F Torque Transducer **179**

G System commissioning **181**

Summary

Permanent magnet synchronous motor (PMSM) drives are widely used in robotics and other high-performance industrial servo applications. PMSM drives are preferred over the traditional, mechanically-commutated brush-type DC motor drives because of the absence of mechanical commutators, and therefore increases the life span of the PMSMs. As compared to induction motors, PMSMs are favored for high-performance servo applications because of their higher efficiency, power density and torque-to-inertia ratio, which make them a suitable choice for variable-speed direct-drive applications.

However, PMSMs suffer from parasitic torque pulsations. These torque pulsations are primarily caused by non-sinusoidal flux density distribution in the air-gap, and cogging. In real PMSMs, a perfect sinusoidal flux density distribution around the air gap periphery is difficult to achieve. This non-perfect sinusoidal flux density distribution gives rise to periodic torque ripples when interacts with the sinusoidal stator currents at the fundamental frequency. Cogging torque is due to the variable magnetic reluctance between the stator slots/teeth and the permanent magnet rotor. Secondary sources of torque pulsations in the PMSM drives are current measurement errors in the controller, and phase unbalancing. These torque pulsations result in instantaneous motor torque that pulsates periodically with rotor position. They are reflected back as periodic oscillations in the motor speed, especially at low speeds. At higher operating speeds, these torque pulsations are naturally filtered off by the rotor and load inertia and therefore, are not reflected back in the motor

speed. In the absence of mechanical gears in direct-drive servos, the PMSM drive has to operate at low speeds. This results in speed oscillations that severely limit the performance of the direct-drive servo especially in high-performance tracking applications.

In view of the increasing popularity of PMSM drives in industrial applications, the suppression of pulsating torque in PMSMs has received much attention in recent years, as reported by Jahns *et al* [1]. However, most of the existing approaches to minimize pulsating torque either involve complicated motor constructions that are impractical in low-cost high volume production or require accurate a priori knowledge of the motor parameters for generating the control current to suppress these torque ripples.

In this research work, two new learning control algorithms are proposed with the objective of minimizing periodic torque ripples. Both proposed control schemes make use of the concept of learning control to generate the required stator current that minimizes periodic torque ripples. One of the proposed controllers uses learning variable structure control (LVSC) algorithm, while the other uses frequency-domain iterative learning control (FILC) algorithm to achieve torque pulsations minimization. For the implementation of torque controllers, it is necessary to obtain the instantaneous torque signal either through direct or indirect measurements. However, the torque transducer is physically bulky and is not economically viable to apply in the industrial environments. Therefore, a torque estimator based on the high gain flux observer is implemented to estimate the instantaneous electromagnetic torque. Nevertheless, the torque control scheme based on a torque estimator results in complexity in system implementation. Considering these disadvantages of the torque controller and facing the wide application of speed controller in industrial environment, we have proposed a LVSC and a FILC speed control schemes to minimize torque pulsations. In this closed-loop speed controller, speed error

information is used to provide the compensation current to reduce torque ripples indirectly. Consequently, two LVSC and two FILC compensation schemes are proposed: (1) torque control with LVSC pulsating torque compensation, (2) speed control with LVSC speed ripple compensation, (3) torque control with FILC pulsating torque compensation, and (4) speed control with FILC speed ripple compensation.

As the pulsating torque is periodic in nature, and given the motor parameter uncertainties and non-linearities, the learning control is intuitively an excellent choice to achieve pulsating torque minimization. Furthermore, both LVSC and FILC schemes only involve a few simple algebraic calculations and a dynamic memory bank; hence, their requirements are minimal from the hardware implementation point of view. The learning controller "learns" the desired current profile from past "experience" of the torque (or speed) error signal and the corresponding control signal in the previous sampling interval.

Simulation studies performed in MATLAB environment have verified the effectiveness of the proposed LVSC and FILC schemes in minimizing periodic torque ripples. To further validate the effectiveness of the proposed scheme, experiments have been performed on an integrated DSP-based PMSM drive setup. The performances of the proposed LVSC and FILC torque or speed ripple compensation schemes are compared with those of the conventional feed-forward sinusoidal current controller or closed-loop PI speed control schemes for a range of operating speeds and torques. Experimental results validate that the proposed LVSC and FILC schemes are implementable for real-time control and effectively improve torque and speed ripples by at least 50% as compared to those of the conventional schemes without compensation. However, despite the effectiveness of proposed schemes in suppressing torque ripples, the applications of the LVSC and the FILC in the PMSM drive are still at their infancy stages. Future work is necessary to further improve the scheme on the following issues:

- A more advanced current controller can be designed with larger bandwidth and tracking capabilities so that the inner current controller can track more accurately the reference currents generated by the proposed learning scheme.
- Non-periodic disturbances and harmonics with non-integer multiple of the fundamental frequency exist in the PMSM drive system. These harmonic components can not be eliminated by the iterative learning control.

Nomenclature

θ_m	mechanical rotor angle of the PMSM
ω_m	mechanical rotor speed of the PMSM
τ_m	electromagnetic torque
f_e	frequency of electrical cycle (synchronous frequency)
ω_e	electrical rotor speed of the PMSM
θ_e	electrical rotor angle of the PMSM
i_{as}, i_{bs}, i_{cs}	phase a, b and c stator currents
i_{0s}	zero-sequence stator current
I_s	peak value of stator current
t	time
ϕ_s	phase angle between the stator voltage and current
F_s	rotating stator MMF
N_{se}	number of effective turns per phase in stator winding
v_{as}, v_{bs}, v_{cs}	phase a, b and c stator voltages
r_s	stator resistance (Ω/phase)
$\lambda_{as}, \lambda_{bs}, \lambda_{cs}$	phase a, b and c flux linkages
v_f	phase voltage in fictitious rotor coil
i_f	phase current in fictitious rotor coil
L_f	self inductance of fictitious rotor coil
λ_f	flux linkage in fictitious rotor coil
L_a, L_b, L_c	phase a, b and c self inductances

M_{ij}	$i, j = a, b, c$, mutual inductance between stator i- and j-phases
M_{fi}, M_{if}	$i = a, b, c$, mutual inductance between stator i-phase and permanent magnet
λ_{if}	$i = a, b, c$, flux linkage between stator i-phase and permanent magnet
λ_m	amplitude of flux linkage between stator and permanent magnet
P_p	number of pole-pairs
τ_{cog}	cogging torque
τ_{self}	self-inductance torque
τ_{mut}	mutual-inductance torque
τ_{emf}	back-emf torque
τ_L	load torque
J	rotor inertia
B	motor damping coefficient
v_{ds}, v_{qs}	d-,q-axes stator voltages
i_{ds}, i_{qs}	d-,q-axes stator currents
$\lambda_{ds}, \lambda_{qs}$	d-,q-axes flux linkages
L_d, L_q	d-,q-axes self inductance
M_{dq}, M_{qd}	mutual inductances between d- and q-axes
M_{df}, M_{qf}	mutual inductances between d- or q-axis and permanent magnet
ψ_d, ψ_q	d-,q-axes flux linkages between stator and permanent magnet
L_s	self inductance in d-q reference frame
u_i	i^{th}-cycle control signal
$\Delta y_i, e_i$	i^{th}-cycle system error
y_i	i^{th}-cycle system output
y_d	desired system output

Γ, Φ	previous-cycle feedback and current-cycle feedback learning gains
α	forgetting factor
R^n	a space of n-tuples of real numbers
$\|z\|$	absolute value of a function z
$\|\mathbf{v}\|$	norm of a vector $\mathbf{v} \in R^n$
$B(D)$	a space of bounded functions on D
$C(D)$	a space of continuous functions on D
$C^n(D)$	a space of n times continuously differentiable functions on D
u_{eq}	equivalent control signal
σ_i	i^{th}-cycle switching surface
$u_{v,i}$	i^{th}-cycle variable structure control signal
$u_{l,i}$	i^{th}-cycle learning control signal
T	electrical cycle period
K_t	torque constant
τ_m^*	desired electromagnetic torque
i_{qs-2}^*	reference compensation current generated by learning controller
$\hat{\tau}_m$	total estimated electromagnetic torque
ψ_d, ψ_q	estimated d-, q-axes flux linkages

List of Figures

1.1 Block diagram of a basic electric drive system 2

1.2 High-performance servo motors 4

1.3 AC versus DC variable speed drives market dynamics 5

1.4 Phase back-emf and current in the BLDCM 9

1.5 Basic BLDCM servo system 10

1.6 Phase back-emf and current in the PMSM 12

1.7 Basic PMSM servo system 12

2.1 Cross-section of a 3-phase, 6-pole, 18-slot, surface-mounted PMSM . 28

2.2 Cross-section of a 3-phase, 6-pole, 18-slot, surface-mounted PMSM . 29

2.3 Trigonometric interpretation of the change of stator variables 36

2.4 Cogging torque production. (a) Net $\tau_{cog} = 0$; (b) Net $\tau_{cog} \neq 0$. . . . 39

2.5 Frequency spectrum of steady-state speed response without compensation under the heavy load. 42

3.1 Iterative learning control configuration 49

3.2 Iterative learning control configuration 53

3.3 Block diagram of Fourier transformation of the learning control signal 59

3.4 Configuration for LVSC torque control scheme 61

3.5 Configuration for closed-loop speed scheme with LVSC speed ripple compensation 64

3.6 Frequency-domain iterative learning control configuration 66

3.7 Configuration for FILC torque control scheme 67

3.8 Configuration for closed-loop speed scheme with FILC speed ripple compensation 70

4.1 PMSM drive scheme employing the proposed LVSC torque control. 79

4.2 Sinusoidal current control scheme: (a) steady-state torque response (TRF=7.60%), and (b) the corresponding frequency spectrum. . . . 80

4.3 Proposed LVSC torque control scheme: (a) steady-state torque response (TRF=0.19%), and (b) the corresponding frequency spectrum. 80

4.4 Sinusoidal current control scheme: (a) steady-state torque response (TRF=9.33%), and (b) the corresponding frequency spectrum. . . . 81

4.5 Proposed LVSC torque control scheme: (a) steady-state torque response (TRF=0.29%), and (b) the corresponding frequency spectrum. 81

4.6 Sinusoidal current control scheme 83

4.7 Proposed LVSC torque control scheme 83

4.8 PMSM drive scheme employing the proposed LVSC speed control. . 84

4.9 Conventional PI speed control scheme: (a) steady-state speed response (SRF=0.2%), and (b) the corresponding frequency spectrum. 86

4.10 Conventional PI speed control scheme with LVSC speed control: (a) steady-state speed response (SRF=0.01%), and (b) the corresponding frequency spectrum. 86

4.11 Conventional PI speed control scheme: (a) steady-state speed response (SRF=0.26%), and (b) the corresponding frequency spectrum. 87

4.12 Conventional PI speed control scheme with LVSC speed control: (a) steady-state speed response (SRF=0.01%), and (b) the corresponding frequency spectrum. 87

4.13 The basic ILC torque control scheme: (a) steady-state torque response (TRF=0.49%), and (b) the corresponding frequency spectrum. 90

4.14 The proposed FILC torque control scheme: (a) steady-state torque response (TRF=0.22%), and (b) the corresponding frequency spectrum. 90
4.15 The basic ILC torque control scheme: (a) steady-state torque response (TRF=1.30%), and (b) the corresponding frequency spectrum. 91
4.16 The proposed FILC torque control scheme: (a) steady-state torque response (TRF=0.90%), and (b) the corresponding frequency spectrum. 91
4.17 Conventional PI speed control scheme with ILC speed control: (a) steady-state speed response (SRF=0.0096%), and (b) the corresponding frequency spectrum. 94
4.18 Conventional PI speed control scheme with FILC speed control: (a) steady-state speed response (SRF=0.002%), and (b) the corresponding frequency spectrum. 94
4.19 Conventional PI speed control scheme with ILC speed control: (a) steady-state speed response (SRF=0.012%), and (b) the corresponding frequency spectrum. 95
4.20 Conventional PI speed control scheme with FILC speed control: (a) steady-state speed response (SRF=0.004%), and (b) the corresponding frequency spectrum. 95
4.21 (a) Actual and estimated torque waveforms (τ=5.31e-3). (b) Estimated torque error. 97
4.22 (a) Actual and estimated torque waveforms (τ=5.31e-4). (b) Estimated torque error. 98
4.23 (a) Actual and estimated torque waveforms (τ=5.31e-2). (b) Estimated torque error. 98

5.1 Photograph of the PMSM and loading mechanism used in experiments 102

5.2 Configuration for the PMSM drive experimental setup 102
5.3 Simplified block diagram of the integrated interface platform 106
5.4 Configuration for the PMSM loading system 109
5.5 Interactions among software during DSP program execution 111
5.6 Flowchart of the main control program 113
5.7 Flowchart of the Interrupt Service Routine 114

6.1 Sinusoidal current control scheme: (a) steady-state torque response (TRF=14.23%), and (b) the corresponding frequency spectrum. . . 118
6.2 Proposed LVSC torque control scheme: (a) steady-state torque response (TRF=2.82%), and (b) the corresponding frequency spectrum. 118
6.3 Sinusoidal current control scheme: (a) steady-state torque response (TRF=15.64%), and (b) the corresponding frequency spectrum. . . 119
6.4 Proposed LVSC torque control scheme: (a) steady-state torque response (TRF=4.10%), and (b) the corresponding frequency spectrum. 119
6.5 Transient torque response when the LVSC compensation scheme is activated. (ω_m=50 rpm, τ_L=1.60 Nm) 120
6.6 The detailed TRFs when PMSM operates at a speed of 50 rpm under different loads without and with LVSC compensation. 120
6.7 Sinusoidal current control scheme: (a) steady-state estimated torque response (TRF=15.0%), and (b) the frequency spectrum. 123
6.8 Proposed LVSC torque control scheme: (a) steady-state estimated torque response (TRF=1.66%), and (b) the corresponding frequency spectrum. 123
6.9 Sinusoidal current control scheme: (a) steady-state estimated torque response (TRF=18.5%), and (b) the corresponding frequency spectrum. 124

6.10 Proposed LVSC torque control scheme: (a) steady-state estimated torque response (TRF=6.28%), and (b) the corresponding frequency spectrum. 124
6.11 Transient torque response when the LVSC compensation scheme is activated. (ω_m=50 rpm, τ_L=1.60 Nm) 125
6.12 Conventional PI speed control scheme: (a) steady-state speed response (SRF=0.65%), and (b) the corresponding frequency spectrum. 127
6.13 LVSC speed control scheme: (a) steady-state speed response (SRF=0.25%), and (b) the corresponding frequency spectrum. 127
6.14 Conventional PI speed control scheme: (a) steady-state speed response (SRF=0.78%), and (b) the corresponding frequency spectrum. 128
6.15 LVSC speed control scheme: (a) steady-state speed response (SRF=0.27%), and (b) the corresponding frequency spectrum. 128
6.16 SRFs of different speeds under a light load of 1.60 Nm without and with LVSC compensation. 129
6.17 Sinusoidal current control scheme: (a) steady-state torque response (TRF=14.23%), and (b) the corresponding frequency spectrum. . . 130
6.18 Basic ILC torque control scheme: (a) steady-state torque response (TRF=4.3%), and (b) the corresponding frequency spectrum.. . . . 131
6.19 Proposed FILC torque control scheme: (a) steady-state torque response (TRF=3.9%), and (b) the corresponding frequency spectrum. 131
6.20 Sinusoidal current control scheme: (a) steady-state torque response (TRF=15.64%), and (b) the corresponding frequency spectrum. . . 133
6.21 Basic ILC torque control scheme: (a) steady-state torque response (TRF=4.8%), and (b) the corresponding frequency spectrum. . . . 134
6.22 Proposed FILC torque control scheme: (a) steady-state torque response (TRF=4.5%), and (b) the corresponding frequency spectrum. 134

6.23 The transient torque response when the FILC compensation scheme is activated (ω_m=50 rpm, τ_L=1.56 Nm). 135
6.24 The transient torque response when the load torque is reduced from 3.83 Nm to 3 Nm with FILC scheme always on. 136
6.25 The detailed TRFs when PMSM operates at different speeds under a heavy load of 5.00 Nm without or with ILC/FILC compensation. 136
6.26 Sinusoidal current control scheme: (a) steady-state estimated torque response (TRF=15.0%), and (b) the corresponding frequency spectrum. 138
6.27 Proposed FILC torque control scheme: (a) steady-state estimated torque response (TRF=3.4%), and (b) the corresponding frequency spectrum. 138
6.28 Sinusoidal current control scheme: (a) steady-state estimated torque response (TRF=18.5%), and (b) the corresponding frequency spectrum. 139
6.29 Proposed FILC torque control scheme: (a) steady-state estimated torque response (TRF=4.0%), and (b) the corresponding frequency spectrum. 139
6.30 Conventional PI speed control scheme: (a) steady-state speed response (SRF=0.65%), and (b) the corresponding frequency spectrum.140
6.31 Basic ILC speed control scheme: (a) steady-state speed response (SRF=0.15%), and (b) the corresponding frequency spectrum. . . . 140
6.32 Proposed FILC speed control scheme: (a) steady-state speed response (SRF=0.10%), and (b) the corresponding frequency spectrum.141
6.33 Conventional PI speed control scheme: (a) Steady-state speed response (SRF=0.78%), and (b) the corresponding frequency spectrum.142

6.34 Basic ILC speed control scheme: (a) Steady-state speed response (SRF=0.47%), and (b) the corresponding frequency spectrum. . . . 142
6.35 Proposed FILC speed control scheme: (a) Steady-state speed response (SRF=0.32%), and (b) the corresponding frequency spectrum. 143
6.36 SRFs of different speeds under a light load of 1.60 Nm without, with ILC and FILC compensation. 143
6.37 Frequency spectrum of torque pulsations induced by the DC generator. 145
6.38 Frequency spectrum of steady-state speed response without compensation under the light load. 145
6.39 Frequency spectrum of steady-state speed response without compensation under the heavy load. 146

B.1 Architecture of DSP DS1102 controller board. 173

C.1 Schematic diagram of MUBW 10-12A7. 174

G.1 Speed response of the PMSM following a step input of rated torque. Time constant, $\tau_c = \Delta t$=2.5 s (x-axis:1 s/div, y-axis:500 rpm/div). . 182

List of Tables

4.1 Torque harmonics with or without LVSC torque control. 82

4.2 Speed harmonics with or without LVSC speed control. 88

4.3 Torque Harmonics with or without ILC/FILC torque control. 92

4.4 Speed harmonics with or without ILC/FILC speed control. 96

6.1 Torque harmonics with or without LVSC torque compensation. . . . 121

6.2 Estimated torque harmonics with/without LVSC torque compensation. 122

6.3 Speed harmonics with or without LVSC speed compensation. 126

6.4 Torque harmonics with or without ILC/FILC torque compensation. 132

6.5 Estimated torque harmonics with or without FILC torque compensation. 137

A.1 Ratings of the PMSM used in this research work 170

A.2 Parameters of the PMSM used in this research work 170

A.3 Ratings and parameters of the DC motor used in this research work 171

E.1 Parameters of current sensors. 178

F.1 Specifications of torque transducer. 180

Chapter 1

Introduction

1.1 Electric Drives

In the present day technology, electric drives have numerous applications ranging from rudimentary motion control to high-precision machine tools and robotics. The electric machine is assigned to do a certain mechanical work in terms of operating a load. Operation of a load is specified in terms of transient or steady torque, speed or position response requirements. In particular, as demand grows for products to be machined to extremely high tolerances and guaranteed quality, high-performance servo drives are extensively used in applications such as position and speed control of robotic manipulators, drives for machine tools, and automobile power steering, etc. A block diagram representation of a basic electric drive is shown in Fig. 1.1. The overall system fundamentally comprises six elements: the power electronic converter, electric motor, the transmission system, the load, the controller, and the electrical and mechanical sensors [2].

The power converter controls the flow of electric power between the motor and the power source such that the motor matches the load requirements. The flow of power in an electric drive can be bi-directional—from the electric power source to the load during motoring, and from the load to the electric power source during regenerative braking. The power electronic converter is a power conditioner and acts as a voltage and frequency changer by using either one or more of a

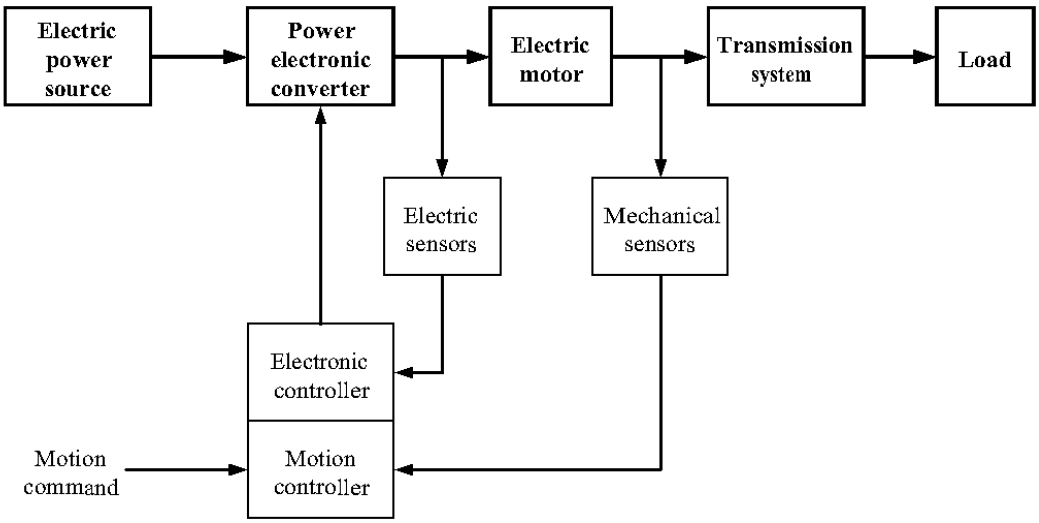

Figure 1.1: Block diagram of a basic electric drive system

chopper, inverter or rectifier. The power electronic switching devices used are mainly phase-controlled thyristors, GTO thyristors, BJTs, power MOSFETs or IGBTs. Depending on the power rating of the converter, a particular type of power semiconductor device is chosen. Pulse-width modulation (PWM) techniques are frequently employed to generate the switching functions for the power converters [3].

Electric motors commonly used in servo drives are: dc commutator, ac synchronous and induction machines. Synchronous and induction machines are characterized by rotating air-gap fields produced by the interaction of the three phase stator currents. Thus, in contrast to dc commutator machines which have space-stationary trapezoidally distributed fields, ac synchronous and induction machines have sinusoidally distributed travelling fields and have no commutators. The transmission system couples the motor to the load either by direct-link as in direct-drive systems, or via gears or motion converters, when there is a need for speed change or rotary-to-linear translation. The load is the driven element.

The control of the converter to match the load requirements with motor capabilities is built by using the low-voltage, low-power control unit. The controller consists of analog and digital integrated circuits and transistors or digital signal

processors (DSPs). The command interfaces the inputs to the controller which, in order to adjust the operating point (torque, speed or position) of the drive by certain control algorithm, makes use of direct feedback sensors, or indirect estimations to provide information about various system parameters for feedback purposes. The control algorithm ensures that the states or output of the servo system accurately tracks the desired trajectory. Where high-performance servos are required, sophisticated control schemes such as fuzzy logic control [4], neural network control [5], vector control [6], direct torque and flux control [7] and feedback linearization control [8] are adopted.

In order to reduce the converter harmonics pollution in the electric power source and to control the power factor at the source, separate sensors are required to measure voltages and currents of the power source. The controller, based on separate commands and sensors, then produces the required performance on the power source side. In general, a dual converter–one on the power source side and one on the motor side with a dc voltage or current link–is required to provide both drive control and power source performance requirements.

There are a variety of servo drives in the market [9]. However, the classification of servo motor drives for a particular application in the fractional hp to 30 hp range can be represented by Fig. 1.2 [10]. The following provides a brief description of the motor drives used in high-performance servo applications as shown in Fig. 1.2.

1.1.1 DC motors

The DC motor operates on the principle of a rotating armature and a stationary field system. Current is supplied to the armature via brushes that are placed along the axis of the commutator. Field excitation produces MMF along the magnetic axis while armature excitation produces MMF along the brush axis. The two MMFs

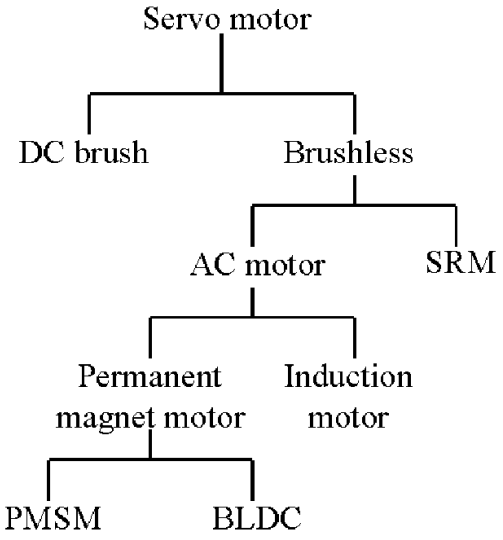

Figure 1.2: High-performance servo motors

in quadrature to each other generate the motor torque that causes the armature to rotate. It is this natural de-coupling nature of the armature and field MMFs that make it easy to control DC motors.

Due to simplicity in their power converter requirement and speed control scheme, DC motors have been the popular choice for variable speed drive applications until the advent of power electronic switching devices in the 1960s which brought about the introduction of the static power electronic converters for AC motors [11]. The power electronic converters allowed a reliable and efficient means to vary the AC supply voltage frequency to drive AC motors for variable speed drive operations. Recently, AC motors became more dominant in the servo industry than their DC counterparts as shown in Fig. 1.3 [12]. The figure shows that AC motors are steadily gaining an increase in their share of the variable speed drives market while DC motors are losing their market proportion.

The decline in demand for DC drives together with the rise in demand for AC drives is because the DC motor suffers from many disadvantages that make them unsuitable for high-performance servo applications. Those disadvantages include [13]:

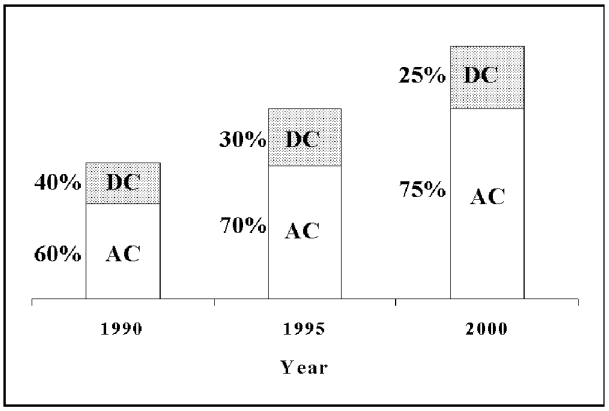

Figure 1.3: AC versus DC variable speed drives market dynamics

- Low reliability and the need for regular maintenance of the commutator.
- Difficulty in producing a totally enclosed motor for some hazardous applications.
- Presence of commutator and brushes constrains the voltage and current ratings, hence restricting its output power rating.
- Relatively low maximum speed due to limitation by mechanical commutator.
- Relatively high cost compared with AC motors.

1.1.2 AC motors

AC motors that are used for high-performance servos generally comprise the induction motor (IM) and the permanent magnet AC (PMAC) motor [10]. AC motors have a relatively simple construction of spatially distributed stator coils and a rotor that is either cage type (in IM) or permanent magnets (in PMAC). In IM, stator excitation gives rise to a sinusoidally rotating stator flux that induces a flux in the rotor. Interaction of the rotor flux with stator currents produces the motor torque. The rotor then rotates with a frequency lagging (slip frequency) behind that of the stator flux. In the case of a PMAC motor, the rotor is a constructed with a high flux density magnetic material like the NdFeB [14]. Thus when the stator

of the PMAC motor is energized, interaction of the PM rotor flux with the stator current in quadrature with the flux produces the torque. The rotor then rotates in synchronism with the rotating stator flux. Applying field-oriented control or vector control [15], the stator phase currents can be de-coupled into the flux and torque producing components (called direct and quadrature-axis components, respectively). Therefore, by controlling each current component respectively, the flux and torque in IMs and PMAC motors can be separately controlled, analogous to the field and armature current control feature of DC motors. However, to achieve field-oriented control, knowledge of the rotor flux vector position is essential. In PMAC motors, a position sensor/encoder is commonly used to determine the rotor position, although the trend is shifting towards sensorless control [16], [17]. As the rotor flux in the IM does not rotate in synchronism with the rotor, it is not possible to use a position sensor to obtain the position of the flux vector directly. Therefore, it is estimated using a flux model with stator voltages, currents and rotor speed as its inputs.

Traditionally, the IM has been the workhorse of the industry for servo applications. IMs are sturdy machines that are very suitable for use in harsh environments. In addition, they are relatively of lower cost when compared with PMAC motors due to the absence of the permanent magnet on the rotor. Furthermore, since the rotor flux in the IM is induced by stator excitation, the rotor flux can also be reduced to a greater extent as compared with the PMAC motor where there is a possibility of permanently demagnetizing the magnets when the demagnetizing currents are too large. This enables the IM to have a larger field weakening range than in the PMAC motor. Therefore, the IM is capable of operating at higher speeds than the PMAC motor.

Nevertheless, PMAC motors are still favored over the IMs for demanding servo applications. This is due to the many advantages the PMAC motors have

over the IMs, which are briefly described in the following [9], [18], [19]:

- PMAC motors have high-energy rare earth permanent magnets on the rotor to provide the air gap flux, while the IMs make use of the movement of rotor windings in the magnetic field to produce rotor MMF or flux. The absence of the rotor cage results in the PMAC motors having a superior torque-to-inertia ratio compared with the IMs of similar size. This property enables the PMAC motors to have a much faster dynamic speed response than the IMs.

- PMAC motors do not require any magnetizing current through the stator as the high flux density permanent magnet rotor provides the constant air gap flux. The stator current is only for torque-production. However, IMs require a source of magnetizing current for excitation. Hence for the same output, PMAC motors operate at a higher power factor than the IMs.

- In PMAC motors (only surface-mounted PM synchronous motors), there is no electrical excitation in the rotor. Hence, rotor losses in the PMAC motors are negligible. On the other hand, in IMs the induced currents in the rotor give rise to rotor losses that can be considerably large depending on the operating slip. This implies that PMAC motors have greater efficiency compared with the IMs.

- The absence of magnetizing current and the high efficiency of the PMAC motors compared with the IMs signify that PMAC drives require lower rated rectifiers and inverters than IM drives to provide the same output capacity.

- In IMs, rotor losses in the form of power dissipation lead to temperature rise in the rotor. As it is not easy to cool the rotor, heat from the rotor is transferred to the load, machine tools and work pieces thus affecting the machine operation. In PMAC motors, however, rotor losses are negligible.

- PMAC motors are relatively smaller in size than the IMs of the same output capacity. This is because in the PMAC motor, there is no rotor cage that is found in the IM. Furthermore, PMAC motors are generally lighter in weight. This means the power density of the PMAC motors are greater than in IMs.

With all the above-mentioned advantages, PMAC motors have found a niche in industries utilizing robotic manipulators and machine tools where excellent dynamic performance and high reliability are mandatory. When efficiency and size are of prime importance as in electric vehicular applications, PMAC motors are the preferred choice.

1.1.3 Switched reluctance motors

Switched reluctance motors (SRMs) are single or multi-phased, doubly salient, singly excited electric motors with windingless or permanent-magnetless rotors. Their concentrated stator coils are turned on and off sequentially through DC voltage pulses, which result in unipolar controlled current that produces the motor torque. In SRMs, knowledge of the rotor position is essential for phase current commutation. Position encoder is used to obtain the rotor position but recently the sensorless control of SRM drives has been receiving much attention [20]. Due to their simple and rugged construction, and high-speed capability, SRMs have been given considerable attention in the last two decades with the hope of producing an alternative brushless electric motor drive at a lower cost and equivalent performance when compared with AC motor drives.

However, SRMs are intrinsically pulsating torque machines. Presence of significantly large torque ripples hinders their use in high-performance servo applications, and is still a major research area today.

1.2 Description of PMAC Motors

PMAC motors fall into the two principal classes: sinusoidally excited (i.e. with a uniformly rotating stator field as in an induction motor) and switched or trapezoidally excited machines (i.e. with a stator field which is switched in discrete steps). The latter one is alternatively known as blushless DC motors, or simply as the switched motors. They have stator windings that are supplied in sequence with near rectangular pulses of current. An excellent review of the PMSM and BLDCM drives can be found in [21]. In this section, however, only the relevant issues of the PMSM and BLDCM drives are mentioned.

1.2.1 Brushless DC motors (BLDCMs)

The BLDCM has stator windings concentrated into narrow-phase belts and a permanent magnet on the rotor. The magnet and the stator windings are shaped such that their interaction produces back-emf that varies trapezoidally with rotor position. To produce constant torque, rectangular-shaped phase currents are applied to the stator. Fig. 1.4 shows the trapezoidal phase back-emf and the rectangular phase current for one electrical cycle in the BLDCM.

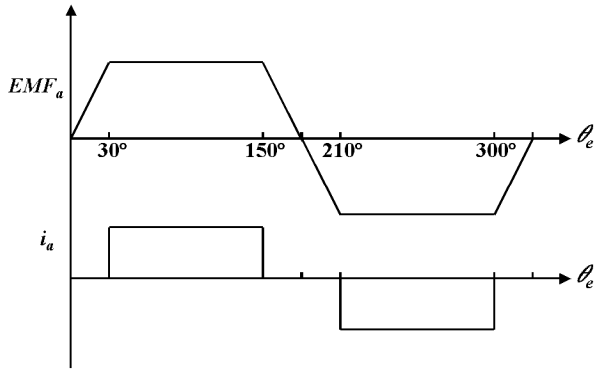

Figure 1.4: Phase back-emf and current in the BLDCM

At any instant, assuming instantaneous current commutation, only two phases are in conduction. A general rectangular current control BLDCM servo system

shown in Fig. 1.5 contains the BLDCM, the PWM inverter, the speed and current controllers, the position and current sensors. An advantage of the BLDCM from the hardware point of view is that only a single current sensor is needed to maintain current regulation in the three phases. This is possible because by measuring the DC link current, I_0, the phase currents in the two conducting phases and the "off" phase can be known, for example, $I_a = I_0$, $I_b = -I_0$ while $I_c = 0$. Another advantage of the BLDCM servo system is that it only requires a low-resolution Hall effect position sensor to achieve self-synchronization. Here, a low-resolution position sensor would suffice because phase commutation occurs at distinct intervals of 60 electrical degrees. Furthermore, control of the inner loop of the BLDCM servo system is very simple, which is only the control of the DC input current [22].

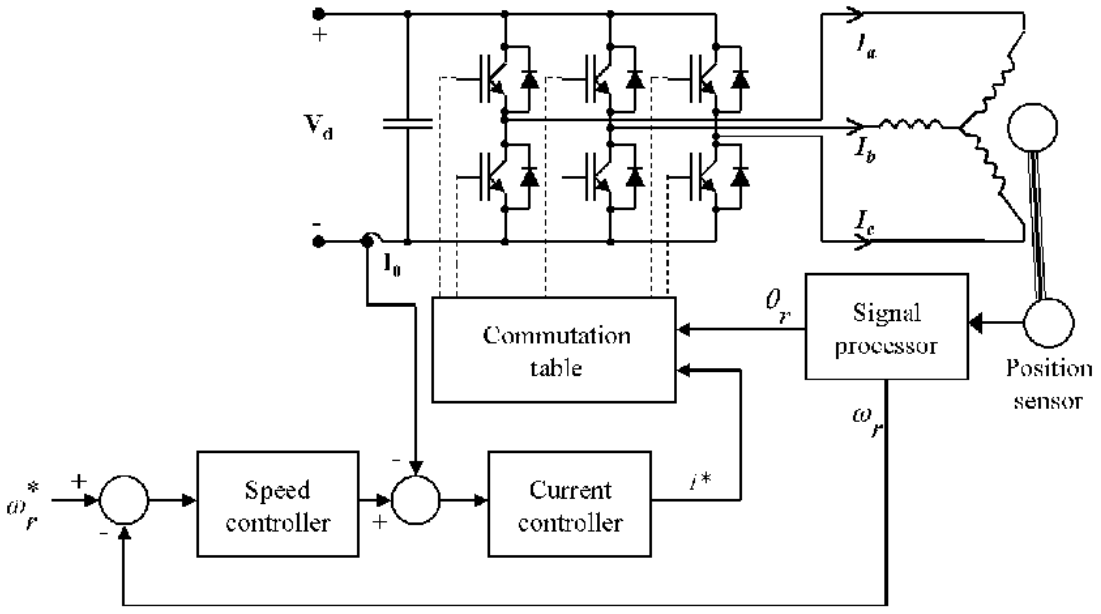

Figure 1.5: Basic BLDCM servo system

However, the simplicity of the BLDCM scheme suffers from several drawbacks. The drawbacks include inherent torque pulsations due to commutation between stator phase currents, limited resolution for position control (the position resolution is 60°) and a limited flexibility for torque ripple control. In a real machine, presence of inductance limits the rate of rise/fall of the phase currents during commutation.

This results in a commutation that requires finite time intervals, during which the torque magnitude may instantaneously fluctuate up to more than 25% of the rated torque [23]. In addition to these, the BLDCM also suffers from torque pulsations that result from cogging and non-ideal back-emf shape (when the constant portion of the trapezoidal back-emf is not 120 electrical degrees). The problem of torque pulsations in BLDCM, especially the commutation torque ripple, has been an intense area of research [22]-[30]. As a consequence of its significant torque ripples and limited-resolution control, the use of the BLDCM remains confined to less demanding speed control systems and low-resolution positioning applications, and not for high-performance servo applications. As this research is focused on the PMSM, which is capable of producing a smoother motor torque than the BLDCM (the magnitudes of the torque ripples in the PMSM are up to only 3% of the rated torque [21]), the analysis on the BLDCM concludes here.

1.2.2 Permanent Magnet Synchronous Motors (PMSMs)

The PMSM has a permanent magnet rotor and stator windings distributed over multiple slots so as to approximate a sinusoidal MMF distribution. The winding arrangement of the stator and the shaping of the magnet result in back-emf that varies sinusoidally with rotor position. To produce constant torque, the stator is fed with sinusoidal shaped stator currents. Fig. 1.6 shows the phase back-emf and sinusoidal stator phase current for one electrical cycle in the PMSM. At any instant, all three phases of the PMSM are in conduction.

The basic drive scheme for the PMSM is shown in Fig. 1.7, where the subscripts d and q indicate quantities in the synchronous reference frame. Compared with the BLDCM, the control system for the PMSM is more demanding, since the six inverter switches in Fig. 1.7 have the added responsibility of sinusoidally shaping the applied excitation waveforms in addition to adjusting their amplitudes

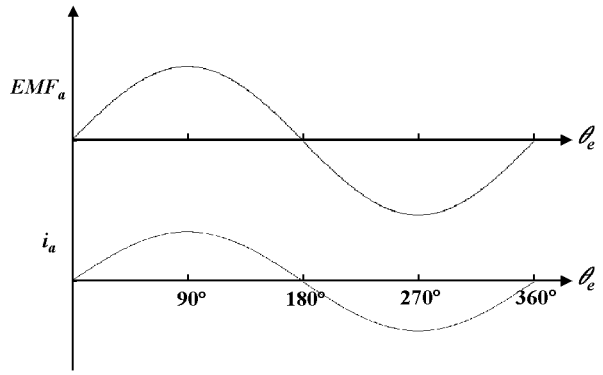

Figure 1.6: Phase back-emf and current in the PMSM

and frequency.

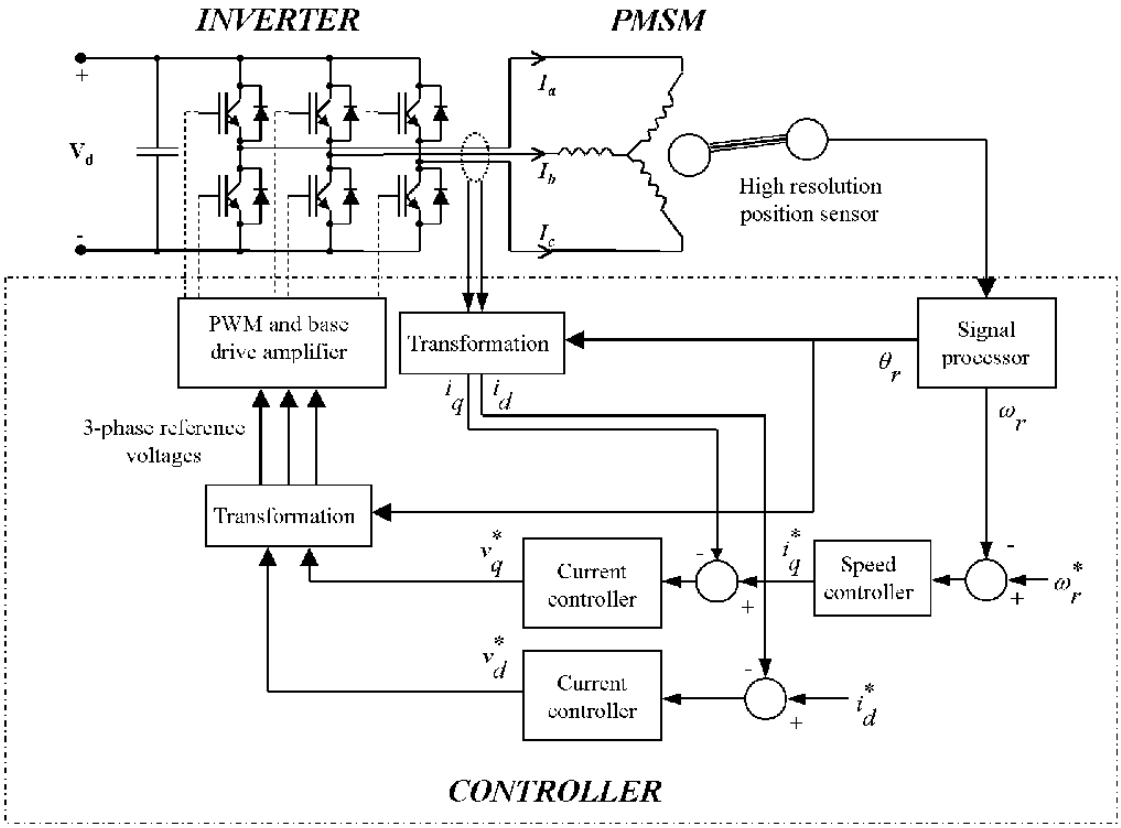

Figure 1.7: Basic PMSM servo system

As three phases are conducting at any instant, two current sensors are required to achieve current regulation. In addition, a high-resolution position sensor is necessary to continuously perform self-synchronization of the motor. However, what sets the PMSM apart from the BLDCM in demanding servo applications is the excellent motion control performance of the PMSM. Compared with the

BLDCM, the PMSM produces a far smoother torque with a superior tracking ability, and possesses a higher speed range [21]. Consequently, PMSM drives are finding expanded use in many high-performance drive applications, especially in the direct-drive of industrial servo systems and robots [31] where torque smoothness and precise tracking are vital.

1.3 Pulsating Torque in the PMSM

Despite the numerous advantages of the PMSM mentioned in the previous sections, PMSMs are still subjected to undesirable torque pulsations [1]. Torque pulsations in the PMSM originate either from the motor structure or from the drive system. Non-ideal flux linkage distribution, harmonics in the self and mutual inductances, variable magnetic reluctance at the stator slots and system phase asymmetries are sources of pulsating torque that originate from the motor structure. On the other hand, current sensor dc offsets, current scaling errors and unbalanced motor phase currents are sources of pulsating torque due to the drive system. Neglecting the torque pulsations resulting from the control system, the main component of torque pulsations is from the non-ideal flux linkage distribution [32]. As a result of these pulsations, the PMSM produces an instantaneous torque that varies periodically with rotor position.

In many high-performance servo applications, presence of any torque pulsation may severely degrade the quality of the work done. For example, the quality of the surface polish using metal-working machining or contouring tools, which is directly dependent on the smoothness of the instantaneous torque delivered to the rotary tool-piece, will deteriorate with the presence of torque pulsations. Similarly, torque pulsations reduce the tracking accuracy of servo motors embedded in robots and satellite trackers. In a direct-drive system, the load is directly coupled to the shaft of the PMSM. The advantage of the direct-drive configuration is the elimina-

tion of the backlash and high friction inherent in a conventional geared drive [33]. Nevertheless, the absence of a high gear ratio requires the motor to operate at low speeds. At high motor speeds, the effects of the torque pulsations are filtered off by the drive system inertia, which acts as a first-order low pass filter. Therefore, torque pulsations are not particularly objectionable for high speed PMSM operation. However, the effects of the torque pulsations become significant at low motor speeds. They are reflected in the motor speed as speed oscillations. Speed oscillations lead to reduced repeatability of the servo and greatly limit the performance of the servo in high-precision tracking applications. Moreover, these speed oscillations produce undesirable mechanical vibrations and acoustic noise in the drive system.

The next section presents the literature review of the pulsating torque minimization techniques proposed by various researchers to date.

1.4 Literature Survey on the Pulsating Torque Minimization Techniques in PMSM

Given the importance of torque smoothness in many PMSM applications, the issue of pulsating torque in the PMSM has been receiving much attention during the past 20 years. A comprehensive review on the approaches for pulsating torque minimization in PMAC motors is given in [1]. These approaches can broadly be classified into two major types of minimization techniques: by (a) proper motor design and (b) active control techniques. The following sub-sections present a survey on these two categories. As this thesis deals with the control aspect of pulsating torque minimization, more focus is given to the latter category while the former is included for completeness of the report.

1.4.1 Motor design techniques for pulsating torque minimization

The most fundamental and effective way to minimize the torque pulsations that are inherently generated within the PMSM is by proper motor design. At this point, it should be established that to attain minimum cogging torque, the variation of air gap magnetic reluctance as seen by the rotor magnets must be minimized. Similarly to attain minimum ripple torque, the harmonic components in the motor back-emf must be minimized.

One of the most popular techniques for cogging torque reduction is stator slot skewing. Studies have demonstrated that skewing the stator slots by one stator tooth pitch can reduce the cogging torque to a very low level [34]-[37]. If stator skewing poses unacceptable manufacturing problems, the alternative approach of skewing the rotor magnetic field distribution by either skewing the rotor magnets [38] or mounting skewed discrete magnet segments on the rotor [39] has also produced similar cogging torque reductions. Skewing also improves the stator winding distribution and substantially reduces the back-emf harmonics hence producing more sinusoidal back-emf [39]. This implies that the ripple torque is reduced as well. However, the drawbacks of skewing are that it results in some loss in the average torque, requires a more complex stator construction, production line set-up, and results in an increase in leakage inductance and stray losses.

Approaches to minimize the air gap magnetic reluctance by minimizing the stator slot openings have also been carried out [34], [40], [41] although these methods have the undesirable effect of complicating the stator construction. In special cases, completely slotless stator configurations have been adopted [42]. Short-pitched stator windings can also be used to reduce the harmonics in the back-emf. Shortening the winding pitch changes the sine term in the Fourier's coefficient which defines the cogging torque thus, able to eliminate a particular cogging torque har-

monic in the winding [43]. In the method proposed in [44], the distribution of the residual magnetic flux density of PM is modified while the pole shape of the armature core is modified in the conventional method so as to achieve cogging torque reduction. Other techniques seek to reduce cogging torque by pushing the harmonic components in the spatial air gap permeance distribution to higher frequencies by either adding dummy slots [45] or dummy teeth [46]. In [37] and [47], it is reported that having fractional-slot pitch stator windings moves the frequency of the cogging torque to a high frequency where it can be easily rejected. The number of stator phases is increased in [43] for the same reason. However, these schemes on stator winding design result in some loss of the average motor torque.

Work on designing the rotor magnets has also been carried out to reduce both cogging and ripple torque. Rotor magnet design techniques for minimizing cogging torque include varying the magnet arc length, varying the magnet strength, shifting the magnet poles and varying the radial shoe depth [48]. To minimize ripple torque, a more sinusoidal flux distribution is generated by proper configuration of the permanent magnets on the rotor [49], [43] and [50].

Nevertheless, until now no motor design technique has been proposed which can completely minimize the pulsating torque for many high-performance applications [48]. Most of the proposed techniques involve a trade-off between pulsating torque reduction and average motor torque production degradation. Another important issue that hinders the feasibility of the motor design techniques is the sensitivity to manufacturing tolerances. Techniques that require a high accuracy of assembly, magnetization, magnet placement or dimensions may prove to be impractical for low-cost high volume production.

1.4.2 Control techniques for pulsating torque minimization

Despite a variety of motor design techniques that are available for minimizing cogging and ripple torque components, the minimization provided by these techniques is not sufficient for many high-performance applications. In many cases, the proposed motor design techniques may not be economical to manufacture in large volumes. Furthermore, the effect of the pulsating torque on the system is dependent on many factors such as the load, the operating speed and the natural frequency of the system. Therefore, solutions that are more flexible to the end-users of the drive system (control engineer) must be implemented. In view of the limitations of the motor design techniques and the need for a more flexible method of pulsating torque minimization, greater emphasis on control techniques has been placed by researchers to achieve pulsating torque reduction. The following subsections review those techniques:

1.4.2.1 Pre-programmed stator current control

One of the most popular approaches to cancel the cogging and ripple torque components in a PMSM is to use pre-programmed excitation signals. In this technique, the phase currents that are required to cancel out the pulsating torque components are first pre-determined as a function of the desired torque and rotor angular position.

Among those pre-programmed current algorithms reported, an important approach comes from recognizing that the instantaneous torque contributed by each machine phase is proportional to the product of back-emf and phase current. Consequently, the optimized current can be derived as being proportional to the reciprocal of the back-emf under the appropriated conditions. Application of this technique can be simplified by first transforming all of the key variables into the *d-q* synchronously rotating reference frame which has the benefit of automatically

eliminating the fundamental frequency component from the back-emf inversion process [51]. An alternate approach in the stationary reference frame [52] uses a special formulation of the reference current equations which is conveniently compatible with this inversion technique, using back-emf waveforms which have been calculated by means of finite element analysis. In [53], Favre *et al* proposed an optimization process for harmonic decomposition of the motor torque by using an iterative process. The initial current shape is compared with the harmonics of the measured motor torque, starting from the most dominant harmonic in the torque pulsation, then the amplitude and phase angle of different current harmonics are modified one-by-one in order to successively suppress the existing torque harmonics. Wu *et al* [54] reported a current profiling method, in which normalized back-emf in terms of rotor speed is determined as prior knowledge, and then the optimal currents can be obtained based on these knowledge and desired torque signal.

Other works on pre-programmed current require accurate information of the pulsating torque characteristics. Generally, investigators first establish a pulsating torque model which describes the actual cogging and ripple torques properly, and then currents can be determined according to a certain operating condition and the required torque command. Hanselman [55] extended those prior works to include the case of a finite supply voltage and finite $\frac{di}{dt}$ capability to produce the current excitation for a minimum torque ripple and maximum efficiency operation. Generation of the optimal currents is accomplished by the construction of a look-up table indexed by rotor position, speed and desired average torque. Holtz and Springob [56] reported a scheme in which the slot harmonics and the flux linkage harmonics can be compensated by injecting additional harmonic components into reference currents. The compensation signals are read from two tables, which are already set by a self-commissioning scheme. Colamartino *et al* [57] presented a numerical current pre-determination from force calculation using the finite element

method to obtain a ripple-free instantaneous torque. Park *et al* [58] proposed a method to achieve ripple-free torque control with maximum efficiency based on the *d-q* reference frame that includes the case of three-phase unbalanced conditions.

The concept of "motor identity" is introduced in [59] with the objective of generating an optimal input current that can produce ripple-free and maximum torque output. Unlike in previous techniques, this control technique does not require any parametric model of the motor (back-emf, inductances and resistances) to generate the optimal currents. Instead, it utilizes the motor identity, which is a matrix comprising the experimentally measured quantities of the phase electromagnetic torque and reluctance torque. In [60], an on-line pulsating torque minimization scheme is proposed. However, preliminary identification of the torque harmonics by examining the output of the position controller is necessary. With the extracted values of the torque disturbance model, the reference current can be derived by modifying the output of the linear regulator, based on the measurements of the rotor position to nullify the torque pulsations.

Since these pre-programmed stator current control schemes are based on feed-forward concepts, the effectiveness of these algorithms in practical applications, including sensitivity to imperfect knowledge of motor parameters and parameter fluctuations, is a justifiable concern. Inaccuracy during off-line model identification gives rise to error in the compensation current that may lead to even higher torque pulsations. Un-modelled torque disturbances such as current scaling error or phase alignment errors will also remain uncompensated in these feed-forward schemes [51].

1.4.2.2 Feedback compensation schemes

Taking into consideration the drawbacks of the open-loop feed-forward schemes, researchers have developed sophisticated feedback compensation schemes to achieve

pulsating torque minimization. Estimation and control schemes are employed either in current (torque) or speed (position) loops. Among these popular torque control schemes, adaptive control method has been used widely. In such schemes, the torque pulsations are compensated by adaptive identification of the disturbances hence they eliminate the errors introduced by inaccurate knowledge of motor parameter, inaccurate motor modelling and variations in the motor parameter, which are of prime concern in the feed-forward compensation case.

In closed-loop torque control methods, feedback signals generated either from the estimation of instantaneous torque signals or from the output of a torque sensor have been applied to eliminate the errors caused by imperfect knowledge of motor parameters and parameter fluctuations. In [61], The concept of instantaneous torque control based on variable structure strategy has been introduced with the aim of minimization of torque pulsations and optimal useful torque production. Melkote *et al* [62] designed an adaptive variable structure control to attenuate the pulsating torque. A current level controller is derived for the motor that achieves asymptotic tracking of a reference trajectory while yielding robustness to parametric and dynamic uncertainties in the motor dynamics. In [63], Chung *et al* developed a new instantaneous torque controller combining a variable structure control with a space-vector pulse-width modulation. The proposed control method provides the advantage of reducing the torque pulsation caused by the non-sinusoidal flux distribution. In [64], an adaptive control algorithm for minimization of torque ripple was presented. The information about torque ripple harmonics used in adaptation is extracted from the electrical subsystem, and a current controller is designed to achieve ripple minimization. The controller is based on the principles of energy shaping and damping injection.

Besides torque controller, speed (or position) controller is also used to suppress torque ripples indirectly. In general, such a scheme consists of two control

loops: an inner current control loop plus an outer speed (or position) control loop. A common way to achieve speed (or position) servo operation is to design a controller that produces the torque reference from the difference between the desired and actual speed (or position). Subsequently, this torque reference can be applied in the inner loop to generate q-axis reference current. Bogosyan and Gokasan [65] designed an adaptive linearizing control using two adaptation parameters for the cogging and ripple torque to be cancelled. The compensation current generated from the adaptively estimated flux and cogging torque parameters is added to the output of the simple outer loop speed (or position) controller to produce the resultant q-axis reference current. In their later work [66], an adaptive linearizing control scheme was designed to compensate the parameter and load variations so as to reduce torque ripples. To account for the instability problem inherent to the adaptive schemes, a robust position control loop based on a chattering-free sliding controller is added to the linearizing controller. Lam *et al* [67] proposed a speed ripple compensation scheme using iterative learning control algorithm to cancel pulsating torque indirectly. The proposed learning controller is implemented in conjunction with a conventional PI speed controller so as to further reduce the speed ripple.

1.4.2.3 Estimators and observers

In the closed-loop torque control scheme, instantaneous torque signal is required as the feedback information, which can be obtained either from a high bandwidth torque transducer or from estimations implemented through software. Various estimation techniques for torque and flux have been proposed to compensate the pulsating torque. These techniques are reasonably similar to the adaptive compensation schemes in which the estimation of the system disturbances, such as cogging torque and flux harmonics, is involved. However, unlike the adaptive schemes, es-

timation of the instantaneous torque or flux signal is explicitly performed and used as feedback signal for pulsating torque minimization.

An early work on the torque estimation scheme was presented by Low *et al* [68], where an instantaneous torque control using variable structure control for torque ripple minimization is implemented. The required instantaneous torque feedback signal is estimated from knowledge of the motor parameters (coefficients of the fundamental and harmonics of the flux linkage), measurements of instantaneous q-axis current and rotor position. As the effectiveness of the scheme proposed in [68] depends on the accurate knowledge of the harmonic coefficients, the work is extended to updating the harmonic coefficient values using an on-line recursive least-squares estimator [61]. In [69], two control concepts for torque ripple reduction are presented: current control-based off-line torque estimation and an on-line observer-based torque control. The former technique utilizes off-line measured torque, which includes the torque harmonics, as a function of the rotor angle and current, and computes the required current to generate a constant torque. The latter technique employs a "dead-beat" torque ripple observer modelled as a partial plant observer based on the q-axis current. A simple on-line torque estimation algorithm that directly employs the d-q stator voltage and electromagnetic torque expressions is proposed in [57]. In [70], the fundamental, 6^{th} and 12^{th} harmonic of the torque are estimated on-line using the estimated motor back-emf so as to generate the necessary 6^{th} and 12^{th} harmonics for the feed-forward q-axis current. However, those torque estimation schemes suffer from drawbacks such as: accurate knowledge of the motor parameters is required (in [57], [68], [69], [70]), limited speed range of operation (in [57]) and difficulty to realize real-time implementation due to complex numerical computation involved as well as high sensitivity to noise (in [68]). In order to overcome these disadvantages, Chung *et al* [63] proposed an instantaneous torque control utilizing variable structure torque controller and

model reference adaptive flux observer from which the estimated torque is obtained. However, the performance of this scheme deteriorates from variations in the motor resistance and inductance from their nominal values. Petrovic *et al* [71] proposed an adaptive control scheme that tracks both the *d*-, *q*-axes flux linkage on-line using the adaptive scheme based on the passivity-based controller. Their later work has been reported in [64], which presented an alternative to the estimation of the complete flux (torque) waveforms by parameterizing the flux expressions with a small number of parameters and adapting on these few coefficients.

An alternative to the torque (or current) control scheme to achieve pulsating torque minimization is by using a speed-loop compensating technique in addition to using a torque or flux observer. From the observed values of the torque or flux, the appropriate compensation current is derived and added to the output of the speed controller. Matsui *et al* [72] proposed a torque observer that employs a minimal-order Gopinath observer to achieve compensation of torque ripple and disturbance in the load. Although the scheme has been reported to exhibit superior speed control characteristic and torque ripple reduction, it requires accurate a priori knowledge of the motor torque constant, which may be sensitive to changes in temperature. In [73], the harmonic terms in the *d*-, *q*-axes flux linkages are identified by a Kalman filter and are stored as functions of the rotor angle. Once the identification is carried out, the compensation period starts and the estimated flux linkages are used to compensate the reference torque generated by the speed controller. Unfortunately, this scheme requires accurate knowledge of the basic motor parameters such as resistance and inductance, which are subjected to parameter variations. In another scheme [74], a simple on-line torque ripple control loop is applied to modify the output of the speed controller. The torque ripple signal in this case is obtained from the measured speed ripple. Similarly, Choi *et al* [75] computed the compensation reference torque by utilizing only the information of

the speed ripple. The schemes that obtain the torque ripple signal via speed ripple signal [74], [75] can be applied only in the low motor speed region. At high speeds, the speed ripple is filtered off, and hence no information about torque pulsation can be extracted from motor speed.

Different methodologies have been proposed for torque/flux estimation, and all of them extract information from the electrical subsystem (i.e., current and voltage measurements) to estimate the complete torque waveform. This waveform is then used as feedback signal for the torque controller. Quality of current measurements enables accurate estimation, and control in the faster inner loop is effective in regulation of the output torque to the ripple free reference. On the other hand, this approach can be used only for those ripple components that are observable from currents—cogging torque can not be minimized using this approach. An alternative method is by using a torque transducer, which has a high-bandwidth output, to detect instantaneous torque signal. Nevertheless, this approach will increase the overall cost of a drive system. According to Jahns [21], until now, there is no known method that can completely and effectively minimize these torque ripples under all conditions. As described above, most of the existing torque ripple minimization schemes suffer the disadvantages of being too computationally demanding, involving complex motor design and construction or require exact knowledge of motor parameters.

In this thesis, pulsating torque minimization schemes, using the concepts of the learning variable structure control and the frequency-domain iterative learning control, are presented. The learning controller overcomes the problems of previously published works such that it does not require much computational overhead, is simple to implement, and does not require sufficiently accurate priori knowledge of motor parameters. At this point, it would be useful to clarify that while the learning controller does not require accurate knowledge of motor parameters, the

torque estimator used in this work requires information of motor parameters. The learning controller exploits the inherent periodicity of the torque (or speed) ripple and suppresses them by learning the torque (or speed) ripple profiles and generating the optimal control signals to minimize them. The following section describes the contributions of this thesis and gives a brief outline of the rest of the thesis.

1.5 Scope of the thesis

This thesis presents a pulsating torque minimization technique in the PMSM using either the learning variable structure control (LVSC) or frequency-domain iterative learning control (FILC) scheme. Both control methods are modified algorithms based on iterative learning control (ILC), and designed for repeatable control problems. The ILC is a control approach to the problem of improving the tracking performance using previous experience in the face of design and modelling uncertainties or system non-linearities in response to periodic disturbances. As the pulsating torque is periodic in nature, and given the motor parameter uncertainties and non-linearities, the learning control is intuitively an excellent technique to achieve pulsating torque minimization.

Two compensation schemes employing either LVSC or FILC are proposed in this thesis. They are:

- Torque control with LVSC pulsating torque compensation;
- Speed control with LVSC speed ripple compensation;
- Torque control with FILC pulsating torque compensation;
- Speed control with FILC speed ripple compensation.

In the torque control scheme, instantaneous torque signals are required as the feedback to the controller. In our experimental set-up, although a high-bandwidth

output (500 Hz) torque transducer is available to provide the instantaneous torque signal, a torque estimator is still proposed to enhance the feasibility of scheme implementation in industrial environment. The torque estimator is based on the high gain flux observer proposed by Stotsky *et al* [76].

The applications of the proposed LVSC and FILC schemes on the PMSM drive system are performed on computer simulation using MATLAB software. The results are compared with the drive performance when using the conventional PI controller. The simulation results are then verified experimentally by applying the proposed schemes on a complete DSP-based PMSM drive system. The rest of this thesis is organized as follows:

Chapter 2 describes the mathematical model for the PMSM. The model of the PMSM is described using two reference frames: the *a-b-c* reference frame and the rotor reference frame (synchronously rotating *d-q* reference frame). Sources of pulsating torque and their mathematical formulation are also presented.

Chapter 3 describes the LVSC and the FILC schemes. A brief analysis on the establishment of both schemes are presented. Subsequently, the application of both schemes in the PMSM drive to achieve pulsating torque minimization is explained. This is followed by a description on the scheme to estimate the instantaneous torque signal using the high gain flux estimator.

Chapter 4 presents the computer simulation results of the proposed LVSC and FILC schemes. The simulation programs are written in MATLAB source codes.

Chapter 5 explains the implementation of the complete DSP-based PMSM drive system. A description of the hardware and software realization of the PMSM drive is also given.

Chapter 6 presents the experimental results of the proposed LVSC and FILC schemes.

Chapter 7 concludes this thesis and provides scope for future work.

Chapter 2

Modelling of the PMSM

2.1 Introduction

In this chapter, the mathematical model of the PMSM is presented. First, the stator voltage, flux-linkage and electromagnetic torque equations are described and their derivations are provided. The equations are expressed in two different reference frames: the *a*-*b*-*c* (stationary) stator reference frame and the *d*-*q* (synchronous rotating) reference frame. Subsequently, a brief description and modelling of the pulsating torque components are presented.

A 3-phase, 6-pole, 18-slot, surface-mounted, rare earth-type PMSM is used in this research work. Fig. 2.1 shows the cross-sectional view of the PMSM. The stator windings (labelled $+a$, $-a$, $+b$, $-b$, $+c$, $-c$) in the PMSM are identical windings, displaced by 120°. Ideally, they are sinusoidally distributed, each having N_s equivalent turns per phase and phase resistance r_s. High-energy NdFeB permanent magnets are fixed on the rotor surface by strong epoxy glue. Electromagnetic torque is produced by the interaction of the magnetic field of the permanent magnet rotor with the electromagnetic field generated by the rotating air-gap MMF established by the currents in the stator windings.

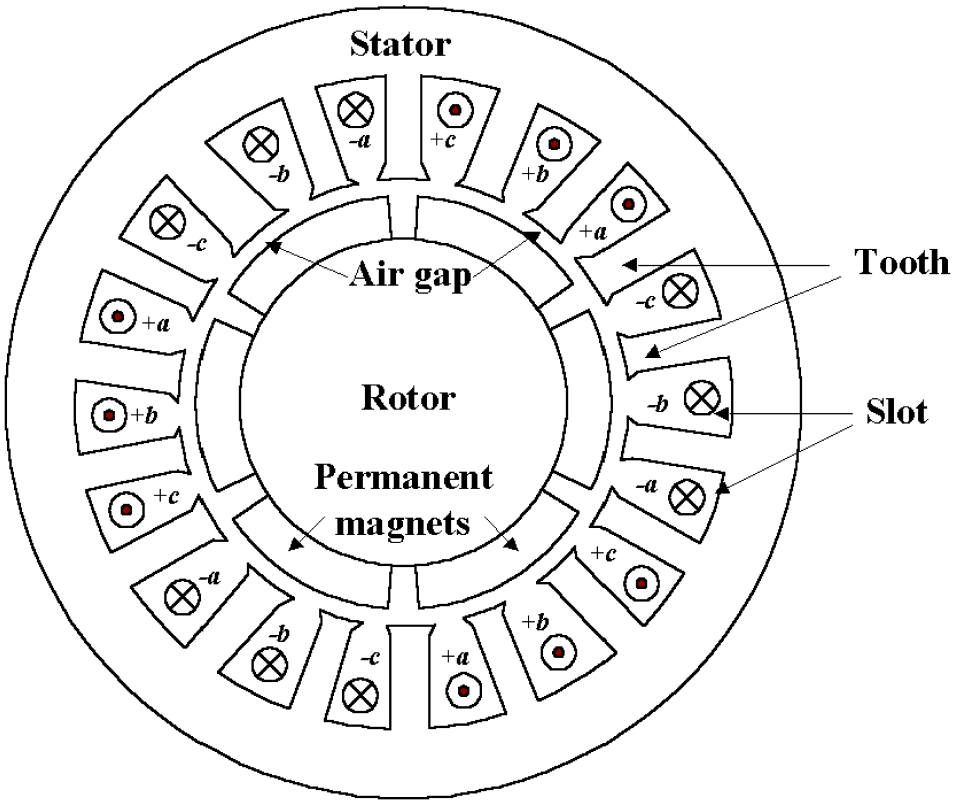

Figure 2.1: Cross-section of a 3-phase, 6-pole, 18-slot, surface-mounted PMSM

2.2 Machine Equations in the a-b-c Frame

In this section, the phase quantities of the stator currents, MMFs, voltages, flux-linkages and electromagnetic torque are described. For simplicity in illustration, a perfectly smooth air gap PMSM with symmetrical 2-pole, 3-phase stator windings is described. Fig. 2.2 shows the cross-sectional view of the PMSM that is a simplified representation of the PMSM shown in Fig. 2.1. The effects of slotting are neglected. The rotor magnets are represented by a 2-pole permanent magnet. The stator windings are shown as a single, multiple-turn full pitch coil. They represent the distributed windings, which at every instant of time produce sinusoidal MMF waves centered on the magnetic axes of the respective phases. From Fig. 2.2, θ_m is the rotor angle, that is, the angle between the rotor flux axis and the stator a-phase winding axis. The mechanical speed of the rotor is denoted by ω_m and its positive direction is assumed to be counter-clockwise in Fig. 2.2. The electromagnetic torque

is denoted by τ_m and its positive direction is the same as rotor speed as shown in Fig. 2.2. The stator voltage is supplied at a frequency f_e, rotating at an angular velocity, $\omega_e = 2\pi f_e$, and θ_e is the rotor electrical angle.

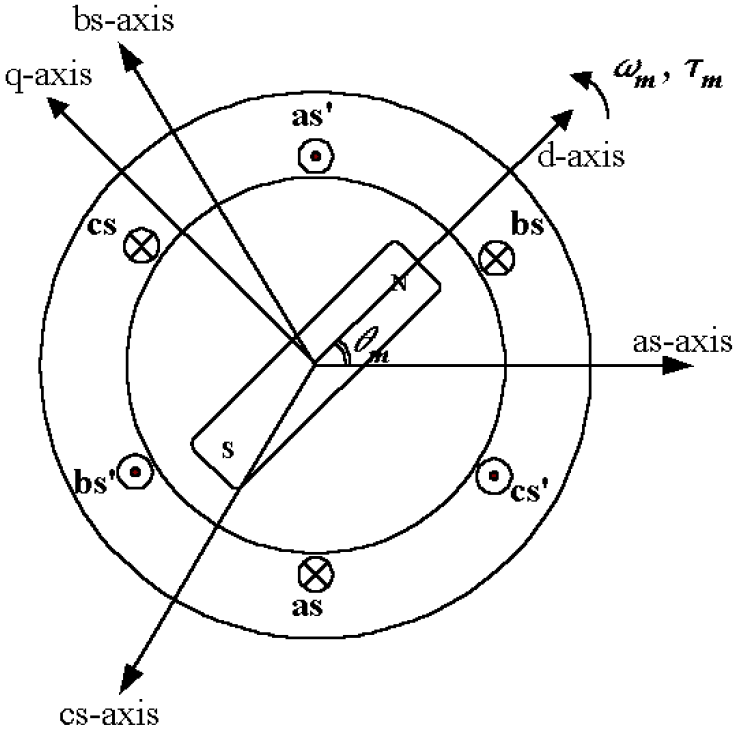

Figure 2.2: Cross-section of a 3-phase, 6-pole, 18-slot, surface-mounted PMSM

The following assumptions are made in the derivation of the mathematical model:

1. saturation is neglected, that is, the magnetic system is operating in its linear region,

2. the motor back-emf is sinusoidal, and

3. eddy currents and hysteresis losses are negligible.

If the stator windings are supplied by a system of 3-phase currents i_{as}, i_{bs} and i_{cs}, which can vary arbitrarily in time but the neutral point is isolated, there can be no zero-sequence currents. Thus,

$$i_{0s} = i_{as} + i_{bs} + i_{cs} = 0, \tag{2.1}$$

where i_{0s} is the instantaneous value of the zero-sequence stator currents.

In steady-state, when the currents are sinusoidal and form a 3-phase balanced system, the phase currents can be expressed as:

$$\begin{aligned} i_{as} &= I_s \cos(\omega_e t - \phi_s) \\ i_{bs} &= I_s \cos(\omega_e t - \phi_s - 2\pi/3) \\ i_{cs} &= I_s \cos(\omega_e t - \phi_s - 4\pi/3), \end{aligned} \tag{2.2}$$

where I_s is the peak value of the stator current, ϕ_s is the phase angle between the stator voltage and current and it is assumed that current is lagging the voltage because of the resistive-inductive nature of the stator windings.

The rotating stator MMF established by the symmetrical 3-phase stator windings carrying balanced 3-phase currents of amplitude I_s is given by [77]:

$$F_s = \frac{N_{se}}{2}\frac{3}{2} I_s \cos(\omega_e t - \phi_s - \theta_m), \tag{2.3}$$

where $N_{se} = N_s k_{ws}$ is the number of effective turns per phase in the stator winding, N_s is the number of turns per phase in the stator winding, k_{ws} is the winding factor and θ_m is the rotor angle previously described.

The stator phase voltages can be expressed in stator co-ordinates as:

$$\begin{aligned} v_{as} &= r_s i_{as} + \frac{d\lambda_{as}}{dt} \\ v_{bs} &= r_s i_{bs} + \frac{d\lambda_{bs}}{dt} \\ v_{cs} &= r_s i_{cs} + \frac{d\lambda_{cs}}{dt}. \end{aligned} \tag{2.4}$$

Equation (2.4) can be written in matrix form as:

$$\boldsymbol{v}_{abcs} = \boldsymbol{r}_s \boldsymbol{i}_{abcs} + \frac{d}{dt}\boldsymbol{\lambda}_{abcs}, \tag{2.5}$$

where $\boldsymbol{f}_{abc} = [\ f_{as} \quad f_{bs} \quad f_{cs}\ ]^T$, $\boldsymbol{f}$ represents either the voltage, current or flux-linkage vector and

$$\boldsymbol{r}_s = \begin{bmatrix} r_s & 0 & 0 \\ 0 & r_s & 0 \\ 0 & 0 & r_s \end{bmatrix}.$$

Assuming that the permanent magnet rotor is a fictitious exciting coil with a constant dc current i_f, self-inductance L_f and flux-linkage λ_f, the rotor voltage equation in rotor co-ordinates is:

$$v_f = \frac{d\lambda_f}{dt}. \tag{2.6}$$

Combining (2.4)-(2.6) yields the voltage equations in both the stator and rotor co-ordinates:

$$\begin{bmatrix} v_{as} \\ v_{bs} \\ v_{cs} \\ v_f \end{bmatrix} = \begin{bmatrix} r_s & 0 & 0 & 0 \\ 0 & r_s & 0 & 0 \\ 0 & 0 & r_s & 0 \\ 0 & 0 & 0 & 0 \end{bmatrix} \begin{bmatrix} i_{as} \\ i_{bs} \\ i_{cs} \\ i_f \end{bmatrix} + \frac{d}{dt} \begin{bmatrix} \lambda_{as} \\ \lambda_{bs} \\ \lambda_{cs} \\ \lambda_f \end{bmatrix} \tag{2.7}$$

or in a concise form:

$$\boldsymbol{v}_t = \boldsymbol{r}_t \boldsymbol{i}_t + \frac{d}{dt}\boldsymbol{\lambda}_t, \tag{2.8}$$

where

$$\boldsymbol{v}_t = \begin{bmatrix} v_{as} \\ v_{bs} \\ v_{cs} \\ v_f \end{bmatrix}, \quad \boldsymbol{r}_t = \begin{bmatrix} r_s & 0 & 0 & 0 \\ 0 & r_s & 0 & 0 \\ 0 & 0 & r_s & 0 \\ 0 & 0 & 0 & 0 \end{bmatrix}, \quad \boldsymbol{i}_t = \begin{bmatrix} i_{as} \\ i_{bs} \\ i_{cs} \\ i_f \end{bmatrix}, \quad \boldsymbol{\lambda}_t = \begin{bmatrix} \lambda_{as} \\ \lambda_{bs} \\ \lambda_{cs} \\ \lambda_f \end{bmatrix}.$$

The flux-linkage $\boldsymbol{\lambda}_t$ in (2.8) can be represented in terms of the inductances and currents by [78]:

$$\begin{bmatrix} \lambda_{as} \\ \lambda_{bs} \\ \lambda_{cs} \\ \lambda_f \end{bmatrix} = \begin{bmatrix} L_a & M_{ab} & M_{ac} & M_{af} \\ M_{ba} & L_b & M_{bc} & M_{bf} \\ M_{ca} & M_{cb} & L_c & M_{cf} \\ M_{fa} & M_{fb} & M_{fc} & L_f \end{bmatrix} \begin{bmatrix} i_{as} \\ i_{bs} \\ i_{cs} \\ i_f \end{bmatrix}, \tag{2.9}$$

where L_i $(i = a, b, c)$ represents the stator i-phase self-inductance, M_{ij} $(i, j = a, b, c)$ represents the mutual inductance between the stator i and j-phases while M_{fi} and M_{if} $(i = a, b, c)$ represent the mutual inductance between stator i-phase and permanent magnet. Assuming linearity of the magnetic field, $M_{ij} = M_{ji}$ $(i, j = a, b, c)$. Equation (2.9) can also be written as:

$$\boldsymbol{\lambda}_t = \boldsymbol{L}_t \boldsymbol{i}_t, \tag{2.10}$$

where $\boldsymbol{i}_t$ is defined as the phase current matrix while $\boldsymbol{L}_t$ is the motor inductance matrix, and

$$\boldsymbol{L}_t = \begin{bmatrix} L_a & M_{ab} & M_{ac} & M_{af} \\ M_{ba} & L_b & M_{bc} & M_{bf} \\ M_{ca} & M_{cb} & L_c & M_{cf} \\ M_{fa} & M_{fb} & M_{fc} & L_f \end{bmatrix}.$$

Extracting the first three rows of the flux-linkage matrix from (2.9) yields the flux linking the stator phases, $\boldsymbol{\lambda}_{abcs}$:

$$\begin{bmatrix} \lambda_{as} \\ \lambda_{bs} \\ \lambda_{cs} \end{bmatrix} = \begin{bmatrix} L_a & M_{ab} & M_{ac} \\ M_{ba} & L_b & M_{bc} \\ M_{ca} & M_{cb} & L_c \end{bmatrix} \begin{bmatrix} i_{as} \\ i_{bs} \\ i_{cs} \end{bmatrix} + \begin{bmatrix} M_{af} i_f \\ M_{bf} i_f \\ M_{cf} i_f \end{bmatrix}. \tag{2.11}$$

Denoting the flux-linkage between the stator phases and the permanent magnet rotor in (2.11) as $\boldsymbol{\lambda}_m$:

$$\boldsymbol{\lambda}_m = \begin{bmatrix} M_{af} i_f \\ M_{bf} i_f \\ M_{cf} i_f \end{bmatrix} = \begin{bmatrix} \lambda_{af} \\ \lambda_{bf} \\ \lambda_{cf} \end{bmatrix}. \tag{2.12}$$

For a 3-phase balanced system, $\boldsymbol{\lambda}_m$ can be represented by:

$$\boldsymbol{\lambda}_m = \lambda_m \begin{bmatrix} \sin(P_p \theta_m) \\ \sin\left(P_p(\theta_m - 2\pi/3)\right) \\ \sin\left(P_p(\theta_m + 2\pi/3)\right) \end{bmatrix}, \tag{2.13}$$

where P_p is the number of pole-pairs, and λ_m is the amplitude of the flux-linkage established by the permanent magnet. For an ideally sinusoidal distributed stator winding, the flux-linkage between the stator and rotor is perfectly sinusoidal, signifying that λ_m is a constant.

In the experimental PMSM, the rotor is assumed to be round with a uniform air-gap. Therefore, the stator inductance matrix in (2.11) can be written as:

$$\boldsymbol{L}_s = \begin{bmatrix} L_{ls} + L_{ms} & -\frac{L_{ms}}{2} & -\frac{L_{ms}}{2} \\ -\frac{L_{ms}}{2} & L_{ls} + L_{ms} & -\frac{L_{ms}}{2} \\ -\frac{L_{ms}}{2} & -\frac{L_{ms}}{2} & L_{ls} + L_{ms} \end{bmatrix}, \tag{2.14}$$

where L_{ls} and L_{ms} represent the leakage and magnetizing inductances of the phases, respectively. The diagonal terms of $(L_{ls} + L_{ms})$ represent the stator phase winding self-inductance L_{ss}. The off-diagonal terms of $-\frac{L_{ms}}{2}$ represent the mutual inductance component. This is because the mutual inductance between the stator

windings displaced by 120° is ($\cos 120° \times L_{ms}$), while if the stator windings were aligned together the mutual inductance is equivalent to L_{ms}.

In the PMSM, the rotor and the stator operate in synchronism. Hence, the rotor rotates at the same angular speed corresponding to the stator supply frequency f_e. From now on, f_e and ω_e will be termed as synchronous frequency and synchronous speed, respectively. Hence, the mechanical speed of the rotor is related to the synchronous speed by:

$$\omega_e = P_p \omega_m. \tag{2.15}$$

Similarly, the mechanical angular position of the rotor is related to the electrical angular position by:

$$\theta_e = P_p \theta_m. \tag{2.16}$$

Finally, the electromagnetic torque τ_m can be calculated from the co-energy derivative with respect to rotor position:

$$\tau_m(i, \theta_e) = \frac{\partial W_{co}(i, \theta_e)}{\partial \theta_e}, \tag{2.17}$$

where W_{co} is the co-energy of the magnetic system. As the magnetic system is assumed to be linear, the field energy and co-energy are equal. From [12]:

$$W_{co} = \int_0^{\boldsymbol{i}_t^T} \boldsymbol{\lambda}_t^T d\boldsymbol{i}_t, \tag{2.18}$$

therefore,

$$\tau_m = \frac{P_p}{2} \boldsymbol{i}_t^T \cdot \frac{d\boldsymbol{L}_t}{d\theta_e} \cdot \boldsymbol{i}_t. \tag{2.19}$$

Using the definition of $\boldsymbol{i}_t$ and $\boldsymbol{L}_t$ in (2.8) and (2.10), (2.19) can be expanded as:

$$\tau_m = \tau_{cog} + \tau_{self} + \tau_{mut} + \tau_{emf}, \tag{2.20}$$

where

$$\tau_{cog} = \frac{P_p}{2} i_f^2 \frac{dL_f}{d\theta_e} \tag{2.21}$$

$$\tau_{self} = \frac{P_p}{2}\left(i_{as}^2 \frac{dL_a}{d\theta_e} + i_{bs}^2 \frac{dL_b}{d\theta_e} + i_{cs}^2 \frac{dL_c}{d\theta_e}\right) \tag{2.22}$$

$$\tau_{mut} = P_p\left(i_{as} i_{bs} \frac{dM_{ab}}{d\theta_e} + i_{bs} i_{cs} \frac{dM_{bc}}{d\theta_e} + i_{cs} i_{as} \frac{dM_{ca}}{d\theta_e}\right) \tag{2.23}$$

$$\tau_{emf} = P_p\left(i_{as} i_f \frac{dM_{af}}{d\theta_e} + i_{bs} i_f \frac{dM_{bf}}{d\theta_e} + i_{cs} i_f \frac{dM_{cf}}{d\theta_e}\right). \tag{2.24}$$

τ_m is considered positive for motor action. τ_{cog} is cogging torque and is a consequence of the variation of self-reluctance of the fictitious field coil as seen by the stator slots. It is independent of stator excitation. τ_{self} and τ_{mut} are torque components due to the variation of self and mutual inductances with θ_e, while τ_{emf} is emf torque and is the product of the back-emf and stator currents. In the case of PMSM, only τ_{emf} contributes significantly to the useful torque.

The motor torque, τ_m, is related to the mechanical speed of the motor, ω_m, by the equation of motion:

$$\tau_m = J\frac{d\omega_m}{dt} + B\omega_m + \tau_L, \tag{2.25}$$

where J is the moment of inertia, B is the coefficient of friction and τ_L is the mechanical load torque.

2.3 Machine Equations in the d-q Frame

In the previous section, the PMSM is modelled in the stationary *a-b-c* reference frame. It can be seen from (2.13) that the stator-rotor mutual flux-linkage varies with rotor position. This signifies that the motor model is non-linear since the motor parameters (flux-linkages) are functions of the states of the motor (rotor position) that vary in a non-linear manner with time. Therefore, it is advantageous to perform a co-ordinate transformations of the motor phase quantities so that the flux-linkages and other motor parameters in the transformed model are constant,

and only the input variables such as voltages and currents vary with time. The co-ordinate transformation applicable in this case is Park's transformation given by [78]:

$$\begin{bmatrix} f_{ds} \\ f_{qs} \\ f_{0s} \end{bmatrix} = \frac{2}{3} \begin{bmatrix} \sin\theta_e & \sin(\theta_e - 2\pi/3) & \sin(\theta_e + 2\pi/3) \\ \cos\theta_e & \cos(\theta_e - 2\pi/3) & \cos(\theta_e + 2\pi/3) \\ 1/2 & 1/2 & 1/2 \end{bmatrix} \begin{bmatrix} f_{as} \\ f_{bs} \\ f_{cs} \end{bmatrix}, \tag{2.26}$$

where f_{ds}, f_{qs} and f_{0s} are the direct, quadrature and zero-sequence quantities, respectively. Equation (2.26) can be written in a more compact form of:

$$\boldsymbol{f}_{dq0s} = \boldsymbol{K}\boldsymbol{f}_{abcs}, \tag{2.27}$$

where $\boldsymbol{f}$ represents any of the stator voltage, current or flux-linkage vector and $\boldsymbol{K}$ is Park's transformation matrix. Fig. 2.3 shows the trigonometric interpretation of the change of stator variables using Park's transformation. The directions of f_{as}, f_{bs} and f_{cs} shown in Fig. 2.3 are the positive direction of the magnetic axes of the stator windings of phases a, b and c, respectively. The direction of f_{ds} is designated to be the positive direction of the rotor permanent magnet flux, while f_{qs} leads f_{ds} by 90 electrical degrees. The zero-sequence variable, f_{0s}, is zero for balanced condition and will be neglected in the following analysis.

Applying Park's transformation on the stator voltage equations in (2.5) yields [78]:

$$\boldsymbol{v}_{dqs} = \boldsymbol{r}_s\boldsymbol{i}_{dqs} + \omega_e\boldsymbol{\lambda}_{qds} + \frac{d}{dt}\boldsymbol{\lambda}_{dqs}, \tag{2.28}$$

where $\boldsymbol{v}_{dqs} = \begin{bmatrix} v_{ds} \\ v_{qs} \end{bmatrix}$, $\boldsymbol{i}_{dqs} = \begin{bmatrix} i_{ds} \\ i_{qs} \end{bmatrix}$, $\boldsymbol{\lambda}_{dqs} = \begin{bmatrix} \lambda_{ds} \\ \lambda_{qs} \end{bmatrix}$ and $\boldsymbol{\lambda}_{qds} = \begin{bmatrix} -\lambda_{qs} \\ \lambda_{ds} \end{bmatrix}$.

Similarly, applying Park's transformation on the stator flux-linkage equation in (2.11):

$$\boldsymbol{\lambda}_{dqs} = \begin{bmatrix} L_d & M_{dq} \\ M_{qd} & L_q \end{bmatrix} \begin{bmatrix} i_{ds} \\ i_{qs} \end{bmatrix} + \begin{bmatrix} M_{df}i_f \\ M_{qf}i_f \end{bmatrix}, \tag{2.29}$$

where L_d, L_q are the d- and q-axes self-inductances, M_{dq} and M_{qd} are the mutual inductances between the d- and q-axes, M_{df} and M_{qf} are the mutual inductances between the d- or q-axis and permanent magnet.

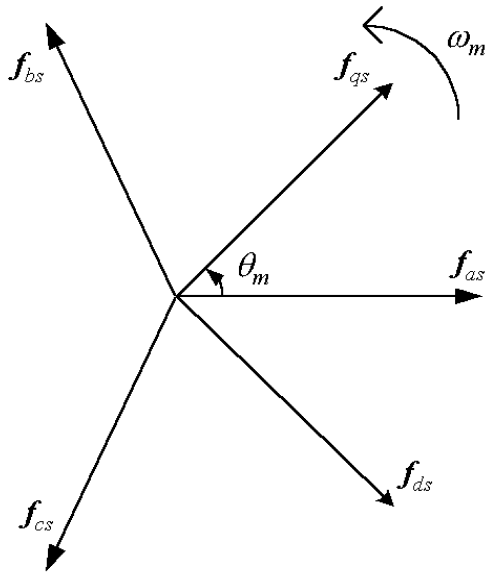

Figure 2.3: Trigonometric interpretation of the change of stator variables

Re-writing (2.28) in expanded form:

$$v_{ds} = r_s i_{ds} - \omega_e \lambda_{qs} + \frac{d\lambda_{ds}}{dt} \tag{2.30}$$

$$v_{qs} = r_s i_{qs} + \omega_e \lambda_{ds} + \frac{d\lambda_{qs}}{dt}, \tag{2.31}$$

where, from (2.29):

$$\lambda_{ds} = L_d i_{ds} + M_{dq} i_{qs} + M_{df} i_f \tag{2.32}$$

$$\lambda_{qs} = M_{qd} i_{ds} + L_q i_{qs} + M_{qf} i_f. \tag{2.33}$$

The Park's transformed inductances, in terms of their average and harmonics components can be represented as [68]:

$$L_d = L_{d0} + L_{d6} \cos 6\theta_e + L_{d12} \cos 12\theta_e + \cdots \tag{2.34}$$

$$L_q = L_{q0} + L_{q6} \cos 6\theta_e + L_{q12} \cos 12\theta_e + \cdots \tag{2.35}$$

$$M_{dq} = M_{dq6} \sin 6\theta_e + M_{dq12} \sin 12\theta_e + \cdots \tag{2.36}$$

$$M_{qd} = M_{qd6} \sin 6\theta_e + M_{qd12} \sin 12\theta_e + \cdots \tag{2.37}$$

$$M_{df} = M_{df0} + M_{df6} \cos 6\theta_e + M_{df12} \cos 12\theta_e + \cdots \tag{2.38}$$

$$M_{qf} = M_{qf6} \sin 6\theta_e + M_{qf12} \sin 12\theta_e + \cdots \tag{2.39}$$

where L_{d0}, L_{d6} and L_{d12} (and L_{q0}, L_{q6} and L_{q12}) are the fundamental, 6^{th} and 12^{th} harmonic components respectively, of the d- (and q-) axis motor self-inductance. Similarly, M_{df0}, M_{df6} and M_{df12} (and M_{qf6}, M_{qf12}) are the fundamental, 6^{th} and 12^{th} harmonic components respectively, of the d- (and q-) axis motor mutual inductance. These harmonic components indicate the extent to which the motor self and mutual inductances vary with rotor position. In surface mounted PMSMs, the effective air gap length is constant (in contrast, the effective air gap length in buried PMSMs varies with rotor position). The variation of the inductance with respect to rotor position is small implying that saliency is negligible. Therefore, the synchronous inductance is constant and independent of rotor position i.e. $L_s = L_d = L_q$. Furthermore, because of the large air gap, the synchronous inductance is small and the effects of the inductance harmonics and armature reaction are negligible [32]. It can therefore be assumed that $L_d = L_{d0} = L_q = L_{q0}$ and $M_{dq} = M_{qd} = 0$.

Therefore, neglecting cogging torque, the electromagnetic torque in (2.20) can be expressed as [63]:

$$\tau_m = \frac{3}{2} P_p \left(\psi_d i_{qs} - \psi_q i_{ds} \right), \tag{2.40}$$

where ψ_d and ψ_q are the d- and q-axes flux-linkage between the stator and PM rotor, respectively, and

$$\psi_d = M_{df} i_f \tag{2.41}$$

$$\psi_q = M_{qf} i_f. \tag{2.42}$$

From [63], as there is no resultant flux-linkage between the q-axis and the PM rotor, thus $\psi_q = 0$. Therefore, substituting (2.32)-(2.39) into (2.30) and (2.31) yields the following stator voltage equations:

$$v_{ds} = r_s i_{ds} + L_{d0} \frac{d}{dt} i_{ds} - \omega_e L_{q0} i_{qs} \tag{2.43}$$

$$v_{qs} = r_s i_{qs} + L_{q0} \frac{d}{dt} i_{qs} + \omega_e L_{d0} i_{ds} + \omega_e \psi_d. \tag{2.44}$$

Applying the method of field-oriented control [6], i_{ds} is controlled to zero and therefore, the expression for the electromagnetic torque in (2.40) simplifies to:

$$\tau_m = \frac{3}{2} P_p \psi_d i_{qs}. \tag{2.45}$$

2.4 Modelling of Pulsating Torque

The issue of pulsating torque in the PMSM, together with a review of the pulsating torque minimization techniques has been described in Chapter 1. As mentioned earlier, torque pulsations in the PMSM owe their origin to the PM motor design and construction, and the drive system. In this section, pulsating torque due to cogging, harmonics in the stator–permanent magnet flux-linkage, dc offset in stator current and current scaling error are described and modelled.

2.4.1 Cogging torque

Cogging torque, τ_{cog}, is produced in the PMSM by the magnetic attraction between the rotor-mounted permanent magnet and the stator teeth, where the rotor-generated magnetic flux seeks a minimum reluctance path to the stator. Cogging torque is independent of stator excitation, as can be seen from (2.21). Fig. 2.4 illustrates the production of cogging torque. In Fig. 2.4 (a), the permanent magnet is aligned with the maximum amount of stator teeth. In this position, the circumferential attractive forces produced by the magnetic flux entering the stator teeth cancel out and therefore, no net τ_{cog} is produced. However, in Fig. 2.4 (b), the rotor has been slightly tilted in the anti-clockwise direction. The circumferential attractive forces do not completely cancel so as to re-align the rotor to where the magnetic path between the north pole of the magnet and the stator tooth has a minimum reluctance (minimum air-gap length). Therefore, a net τ_{cog} is produced in the clockwise direction. Here, τ_{cog} is negative in direction as it tries to return

the rotor to the position as shown in Fig. 2.4 (a).

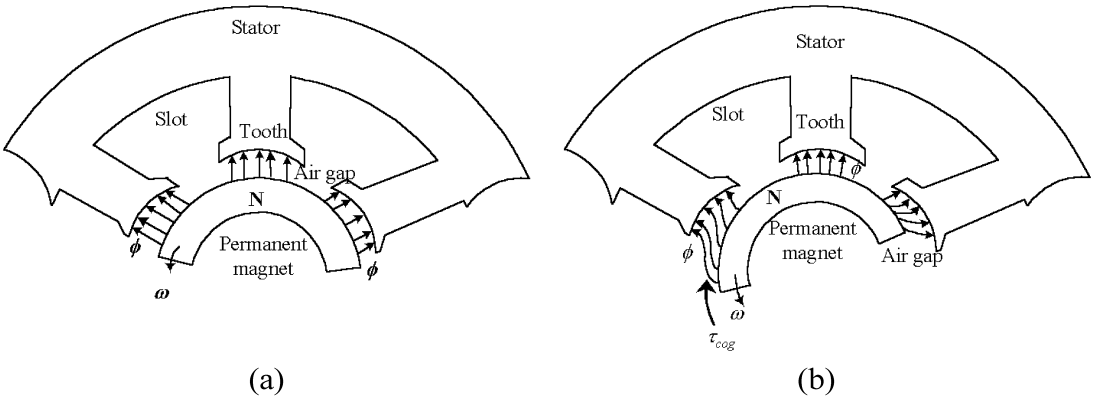

Figure 2.4: Cogging torque production. (a) Net $\tau_{cog} = 0$; (b) Net $\tau_{cog} \neq 0$.

Analytical modelling of cogging torque is challenging. By far, the most popular approach of numerically calculating the cogging torque is by finite element analysis [79]. In this section, a simple model of the cogging torque is presented. Cogging torque experienced by the k^{th} stator tooth of an unskewed PMSM can be written as the Fourier series [37]:

$$\tau_{cog,k} = \sum_{n=1}^{\infty} \tau_n \sin\left[nP(\theta_m - k\theta_s)\right], \quad k = 0, 1, \cdots, N_s - 1 \tag{2.46}$$

where n is the per-tooth harmonic index of the cogging torque, P is the number of magnet poles, N_s is the number of stator slots and θ_s is the angular slot pitch ($\theta_s = 2\pi/N_s$). Therefore, the net cogging torque is the algebraic sum over all teeth:

$$\tau_{cog} = \sum_{k=0}^{N_s-1} \tau_{cog,k}. \tag{2.47}$$

Because the net cogging torque is an algebraic sum, the per-tooth harmonic index n that appear in the net cogging torque satisfies the relationship:

$$cd(nP, N_s) = N_s, \tag{2.48}$$

where $cd(x, y)$ is the common divisor of x and y.

The experimental PMSM has 6 magnet poles and 18 stator slots. Thus, applying $P = 6$ and $N_s = 18$ into (2.48) yields $n \in \{3, 6, 9, \cdots\}$. From (2.46) and

(2.47),

$$\tau_{cog} = \sum_{n=3,6,9,\cdots}^{\infty} \tau_n \Theta_n \sin(n6\theta_m), \tag{2.49}$$

where

$$\Theta_n = \sum_{k=0}^{17} \cos(n6k\theta_s). \tag{2.50}$$

In most cases, only the first harmonic at $n = 3$ contributes significantly to cogging torque while the higher order harmonics ($n = 6, 9, \cdots$) can be neglected [37], [60]. Therefore, (2.49) can be simplified to:

$$\tau_{cog} = \tau_3 \Theta_3 \sin(18\theta_m). \tag{2.51}$$

From (2.16), $\theta_e = 3\theta_m$ hence,

$$\tau_{cog} = \tau_{cogpk} \sin(6\theta_e) = \tau_{cogpk} \sin(6\omega_e t), \tag{2.52}$$

where τ_{cogpk} is the cogging torque amplitude.

Therefore, in the experimental PMSM, cogging torque occurs at a frequency 6 times the synchronous frequency f_e. Cogging torque can be reduced via proper motor design and its effect is significant at only low speeds. In this work, it is assumed that cogging torque in the PMSM has been sufficiently reduced by proper motor design and construction.

2.4.2 Torque ripple due to back-emf harmonics

In the PMSM, harmonics of the back-emf is the most significant contributing factor to the production of torque ripples. As explained in the previous chapter, a non-perfectly sinusoidal distributed stator windings results in the stator-rotor mutual inductance that varies with respect to rotor angular position. This implies that $\frac{dM_{af}}{d\theta_e}$, $\frac{dM_{bf}}{d\theta_e}$ and $\frac{dM_{cf}}{d\theta_e}$ are non-zero values. Hence, the stator-rotor flux-linkage λ_m is no longer constant and consists of higher order harmonics. This results in phase back-emfs that are not perfectly sinusoidal. In stationary coordinates, the phase-a

back-emf generated by the rotating permanent magnet can be expressed as [32]:

$$\begin{aligned} E_a &= \frac{d\lambda_{af}}{d\theta_e} \\ &= M_1 \sin\theta_e + M_3 \sin(3\theta_e) + M_5 \sin(5\theta_e) + M_7 \sin(7\theta_e) \cdots , \end{aligned} \tag{2.53}$$

where λ_{af} is the flux linking stator phase-a and the permanent magnet as given in (2.12). E_b and E_c are similar to (2.53) but phase shifted by $-2\pi/3$ and $-4\pi/3$ respectively. Assuming purely sinusoidal stator phase currents expressed in (2.2) and neglecting τ_{cog}, τ_{self} and τ_{mut}, the motor torque comprises only τ_{emf}. Thus, it can be expressed from (2.24) as [22]:

$$\tau_m = \tau_{emf} = \tau_0 + \tau_6 \cos 6\theta_e + \tau_{12} \cos 12\theta_e + \cdots , \tag{2.54}$$

where

$$\tau_0 = \frac{3P_p}{2\omega_e} M_1 I_s \tag{2.55}$$

$$\tau_6 = \frac{3P_p}{2\omega_e} (M_7 - M_5) I_s \tag{2.56}$$

$$\tau_{12} = \frac{3P_p}{2\omega_e} (M_{13} - M_{11}) I_s. \tag{2.57}$$

Equations (2.54)-(2.57) describe the ripple torque due to back-emf harmonics in terms of quantities in the a-b-c frame. In the d-q frame, the ripple torque is described in the following.

In the presence of harmonics in the stator-rotor flux-linkage, from (2.38) and (2.41), the expression for the d-axis flux-linkage between the stator and rotor becomes [63]:

$$\psi_d = \Psi_{d0} + \Psi_{d6} \cos 6\theta_e + \Psi_{d12} \cos 12\theta_e + \cdots , \tag{2.58}$$

where $\Psi_{d0} = M_{df0} i_f$, $\Psi_{d6} = (6M_{qf6} + M_{df6}) i_f$ and $\Psi_{d12} = (12M_{qf6} + M_{df12}) i_f$.

Substituting (2.58) into (2.45) yields a similar torque expression as in (2.54):

$$\tau_m = \frac{3}{2} P_p i_{qs} \left(\Psi_{d0} + \Psi_{d6} \cos 6\theta_e + \Psi_{d12} \cos 12\theta_e + \cdots \right) \tag{2.59}$$

or

$$\tau_m = \frac{3}{2} P_p i_{qs} \left(\Psi_{d0} + \Psi_{d6} \cos 6\omega_e t + \Psi_{d12} \cos 12\omega_e t + \cdots \right). \tag{2.60}$$

Equations (2.54) and (2.60) show that the torque ripple due to back-emf harmonics is of 6, 12, $\cdots$ times of the synchronous frequency f_e.

Fig. 2.5 shows the back-emf of the PMSM used in experimental study when the motor is operated at a speed of 500 rpm. It can be found that odd harmonic components do exist, which are one of the major sources contributing to torque pulsations.

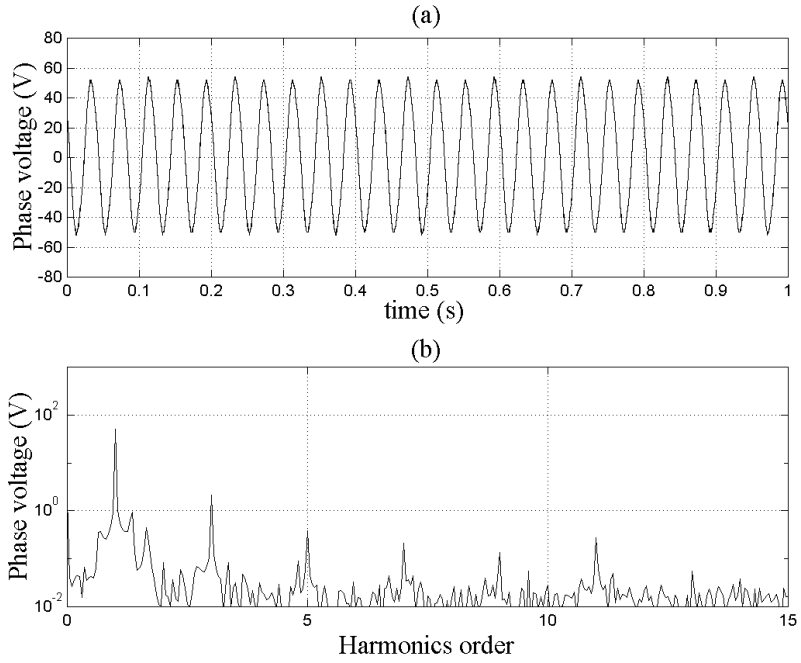

Figure 2.5: Frequency spectrum of steady-state speed response without compensation under the heavy load.

2.4.3 Torque ripple due to dc offset current error

Stator currents needed for control are measured with current sensors and transformed into digital form via low-pass filters and A/D converters. Since the positive and negative dc supply voltage of the current sensor may be unbalanced, and the

current measurement path contains many analog devices, dc offset is an inevitable problem [80], [81].

In the case of a Y-connected PMSM without any neutral point connection, it is sufficient to measure only 2-phase currents for vector control. Assuming phases a and b currents are measured, the measured phase currents can be expressed as:

$$\begin{aligned} i_{as-M} &= i_{as} + \Delta i_{as} \\ i_{bs-M} &= i_{bs} + \Delta i_{bs}, \end{aligned} \tag{2.61}$$

where Δi_{as} and Δi_{bs} are the dc offset error in phases a and b, respectively.

Similarly, denoting Δi_{ds} and Δi_{qs} as the dc offset terms in d-q frame, the corresponding measured currents in d-q frame are:

$$\begin{aligned} i_{ds-M} &= i_{ds} + \Delta i_{ds} \\ i_{qs-M} &= i_{qs} + \Delta i_{qs}, \end{aligned} \tag{2.62}$$

where Δi_{ds} and Δi_{qs} are obtained from the Park's transform of Δi_{as} and Δi_{bs} [80]:

$$\begin{aligned} \Delta i_{ds} &= \frac{2}{3}\left[\Delta i_{as}\sin\theta_e + \Delta i_{bs}\sin(\theta_e - 2\pi/3) + (-\Delta i_{as} - \Delta i_{bs})\sin(\theta_e + 2\pi/3)\right] \\ &= \frac{2}{\sqrt{3}}\sqrt{\Delta i_{as}^2 + \Delta i_{as}\Delta i_{bs} + \Delta i_{bs}^2}\cos(\theta_e + \varphi) \end{aligned} \tag{2.63}$$

$$\begin{aligned} \Delta i_{qs} &= \frac{2}{3}\left[\Delta i_{as}\cos\theta_e + \Delta i_{bs}\cos(\theta_e - 2\pi/3) + (-\Delta i_{as} - \Delta i_{bs})\cos(\theta_e + 2\pi/3)\right] \\ &= \frac{2}{\sqrt{3}}\sqrt{\Delta i_{as}^2 + \Delta i_{as}\Delta i_{bs} + \Delta i_{bs}^2}\sin(\theta_e + \varphi) \end{aligned} \tag{2.64}$$

$$\varphi = \arctan\left(\frac{\sqrt{3}\Delta i_{as}}{\Delta i_{as} + 2\Delta i_{bs}}\right). \tag{2.65}$$

Assuming perfect tracking of the currents, the measured currents exactly follow their reference values:

$$\begin{aligned} i_{ds-M} &= i_{ds}^* \\ i_{qs-M} &= i_{qs}^*, \end{aligned} \tag{2.66}$$

which implies, from (2.62), that:

$$\begin{aligned} i_{ds} &= i_{ds}^* - \Delta i_{ds} \\ i_{qs} &= i_{qs}^* - \Delta i_{qs}, \end{aligned} \tag{2.67}$$

where i_{ds}^*, i_{qs}^* are the reference d and q-axis currents, respectively.

The effects of Δi_{ds} on the d-axis stator flux-linkage, λ_{ds}, can be neglected since the synchronous inductance in the PMSM is small, hence from (2.32), the product of the small variation in i_{ds} with L_d is insignificant compared with the relatively larger stator-rotor flux-linkage, ψ_d (or $M_{df} i_f$). However, Δi_{qs} affects the output torque. From (2.45) and (2.67):

$$\tau_m = K_t(i_{qs}^* - \Delta i_{qs}) = \tau_m^* - \Delta\tau_m. \tag{2.68}$$

Substituting (2.64) into (2.68) yields:

$$\Delta\tau_m = K_t \frac{2}{\sqrt{3}} \sqrt{\Delta i_{as}^2 + \Delta i_{as}\Delta i_{bs} + \Delta i_{bs}^2}\, \sin(\theta_e + \varphi). \tag{2.69}$$

Denoting θ_e by $\omega_e t$, (2.69) shows that offset current error gives rise to a torque oscillation at the synchronous frequency f_e.

2.4.4 Torque ripple due to current scaling error

Another source of torque pulsations that arises from current measurement error is the current scaling error. The outputs of the current sensors have to be scaled to match the input voltage range of the A/D converter. This initial scaling is done via hardware electronic circuits. After the current signals have been converted into digital form, the controller re-scales the value of the A/D output to obtain the actual values of the phase currents. Implementation of a perfect scaling factor is virtually impossible, hence, scaling error of the currents is inevitable.

Again, assuming perfect current tracking as in (2.66), the measured phase

currents are:

$$\begin{aligned} i_{as-M} &= i_{as}^* = I_s \cos\theta_e \\ i_{bs-M} &= i_{bs}^* = I_s \cos(\theta_e - 2\pi/3) \end{aligned} \tag{2.70}$$

Denoting the scaling factors of the phases a and b currents as K_a and K_b, respectively, the phase currents as seen by the controller are:

$$\begin{aligned} i_{as} &= \frac{I_s \cos\theta_e}{K_a} \\ i_{bs} &= \frac{I_s \cos(\theta_e - 2\pi/3)}{K_b} \end{aligned} \tag{2.71}$$

From similar analysis as in the current offset error in (2.64), the corresponding error due to current scaling in the q-axis current is:

$$\begin{aligned} \Delta i_{qs} &= i_{qs-M} - i_{qs} \\ &= \frac{2}{3}\left[i_{as}^* \cos\theta_e + i_{bs}^* \cos(\theta_e - 2\pi/3) + (-i_{as}^* - i_{bs}^*)\cos(\theta_e + 2\pi/3)\right] \\ &\quad -\frac{2}{3}\left[\frac{i_{as}^*}{K_a}\cos\theta_e + \frac{i_{bs}^*}{K_b}\cos(\theta_e - 2\pi/3) + (-\frac{i_{as}^*}{K_a} - \frac{i_{bs}^*}{K_b})\cos(\theta_e + 2\pi/3)\right] \\ &= \frac{2}{\sqrt{3}}\left[i_{as}^*(1 - \frac{1}{K_a})\sin(\theta_e + \pi/3) + i_{bs}^*(1 - \frac{1}{K_b})\sin\theta_e\right] \\ &= I_s\left[\frac{K_a - K_b}{\sqrt{3}K_aK_b}\sin(2\theta_e + \pi/3) - \frac{K_a + K_b}{2K_aK_b} + 1\right] \end{aligned} \tag{2.72}$$

From (2.68) and (2.72), the torque error is:

$$\Delta\tau_m = K_t I_s\left[\frac{K_a - K_b}{\sqrt{3}K_aK_b}\sin(2\theta_e + \pi/3) - \frac{K_a + K_b}{2K_aK_b} + 1\right]. \tag{2.73}$$

Again denoting θ_e by $\omega_e t$, (2.73) shows that the scaling error causes the torque error to oscillate at twice the fundamental frequency $2f_e$.

2.5 Conclusion

In this chapter, a detailed modelling of the PMSM in two different reference frames has been presented. In addition, modelling of the pulsating torques in the PMSM

is also described. It has been shown that the cogging torque produces torque pulsations of frequency 6, 12, $\cdots$ times of the fundamental stator excitation frequency f_e. Similarly, torque ripple due to back-emf harmonics are also of the order 6, 12, $\cdots$ times of f_e. Errors in current measurement also give rise to torque ripple: the dc offset error generates a torque ripple of frequency that is equal to f_e while current scaling error produces a torque ripple at frequency twice that of f_e. Pulsating torques that are due to cogging and back-emf harmonics originate inherently within the PMSM, and are the main sources of torque pulsations in the PMSM. They are termed as primary phenomena. Conversely, the other torque pulsations such as current offset and scaling error originate from the drive system; hence, they are termed as secondary phenomena.

As described in Chapter 1, it is desirable to get a constant motor torque at the output. Therefore, it is necessary to compensate those torque pulsations by some means, which is the topic of research and is discussed in the following chapters.

Chapter 3

Application of LVSC and FILC for Pulsating Torque Minimization in PMSM

3.1 Introduction

In this chapter, the novel concepts of applying the learning variable structure control (LVSC) and the frequency-domain iterative learning control (FILC) to achieve pulsating torque minimization in the PMSM are presented. Both algorithms are modifications of the basic iterative learning control (ILC). To minimize torque pulsations in PMSM described in the previous chapter, current practice in many cases is by the way of meticulous design and construction of the motor, or off-line determination of the optimal stator current waveform. Here, learning control appears to be a judicious natural approach to achieve pulsating torque minimization, since it use the periodic nature of the torque pulsations as a function of rotor position in electrical angle. The control action in each cycle is based on the difference between the instantaneous motor torque (or speed) and the desired torque (or speed) in the previous cycle. Unlike in the other pulsating torque minimization schemes described in Chapter 1, this control scheme does not require exact detailed knowledge of the disturbance model and motor parameters. Therefore, this approach has significant practical advantages over the other proposed schemes, since ac-

curate system modelling and identification are likely to be inaccurate and very costly to obtain experimentally for industrial use. Furthermore, the LVSC and the FILC schemes can be implemented in the existing field-oriented control based drive scheme without any extra hardware modifications on the system. From the point of view of system requirement, both control schemes can be easily applied without any additional cost or any significant increase in computation time.

Section 3.2 gives a brief introduction of the basic ILC scheme, which is the fundamental concept for the LVSC and the FILC schemes proposed later. The algorithms and applications of the LVSC and the FILC schemes are described in Section 3.3 and Section 3.4, respectively. As the proposed method of pulsating torque minimization using the LVSC or the FILC requires feedback of the instantaneous torque signal, an on-line torque estimator is also proposed in Section 3.5. Finally, Section 3.6 concludes this chapter.

3.2 The Basic Iterative Learning Control

ILC is a relatively new approach to the problem of improving the tracking performance using previous experience in the face of design and modelling uncertainties or system non-linearities in response to periodic disturbances in the input. Originally developed by Arimoto *et al* [82], learning control is an iterative approach to generate the optimal system input so that the system output is as close as possible to the desired one. Much work has been done in recent years on the application of the ILC in servomechanism systems for industrial applications, especially in robotic manipulators [82], [83], [84], mechanical processes such as metal rolling [85] and chemical processes [86].

Before presenting the concepts of LVSC and FILC, it is necessary to introduce the basic theory of ILC, since both algorithms are developed based on this learning theory. The basic idea of the ILC is illustrated in Fig. 3.1. From the figure, each

time the system operates, input to the system, u_{i-1}, is stored in the memory, along with the resulting system output error, Δy_{i-1}. The learning controller evaluates the system error as compared to the desired signal y_d and then computes a new input, u_i, which is stored for use in the next cycle of operation. The new input u_i is chosen such that it guarantees the performance error will be reduced in the next iteration. Thus, given the previous input u_{i-1}, output y_{i-1} and desired output y_d, the task of the learning control is to specify the function $F(u_{i-1}, \Delta y_{i-1})$ for generating the next input u_i, such that convergence to the desired output is achieved.

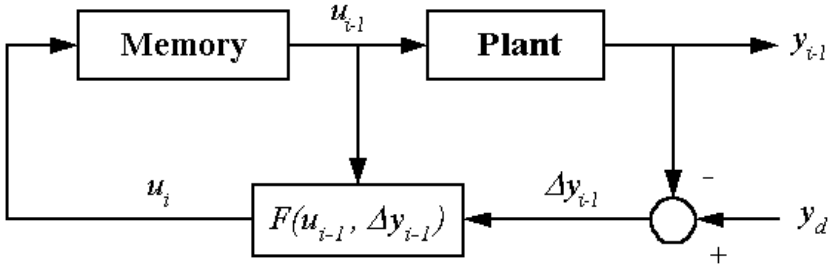

Figure 3.1: Iterative learning control configuration

The convergence property of the learning control algorithm would require a minimal (partial) knowledge of the system parameters and is independent on the desired output y_d. Therefore, simply by using input-output data obtained from actual plant operation, the ILC can derive the optimal control input for any desired response. Furthermore, as only partial knowledge of the system parameters is required, the ILC works well even in the presence of system parameter uncertainties. In the PMSM system, "partial" knowledge of system parameters: the motor flux linkage ψ_d and the range over which it may vary is required to compute the learning gain. An accurate value of the motor flux linkage ψ_d is not required. This is the primary difference between learning control and pre-programmed current excitation (optimal control method) described in Chapter 1. In the pre-programmed current excitation method, the optimal input is computed by using an accurate model of

the system. In optimal control techniques, inaccurate knowledge of motor parameters or presence of error in the modelling will lead to poor control performance. However, those shortcomings do not affect the ILC scheme and this is why the ILC has gained importance for industrial usage.

For a qualitative description of the ILC operation, the following non-linear, time-varying dynamic system is considered [87]:

$$\dot{x}(t) = a\left(x(t), t\right) + b(t)u(t) + \eta(t) \tag{3.1}$$

$$y(t) = c\left(x(t), t\right) + \xi(t) \tag{3.2}$$

where $x(t) \in R$, $u(t) \in R$, $y(t) \in R$ for all $t \in [0, T]$, T being the time period of the desired output. The functions $a \in R$, $b \in R$ are piecewise continuous in t and $c \in R$ is differentiable in x and t. $\eta(t) \in R$ refers to some unstructured uncertainties due to the state perturbations, un-modelled dynamics or repetitive disturbances, while $\xi(t) \in R$ denotes the random output measurement noises. The fundamental principles that underlie the concept of learning control are described by the following postulates:

A1: Each operation ends in a finite time duration $T > 0$.

A2: A desired output trajectory $y_d(t)$ is given a priori for $t \in [0, T]$.

A3: The system must start with the same initial condition throughout repeated iterations, where i is the iteration number and $i = 1, 2, 3, \cdots$.

A4: Invariance of the system dynamics is ensured throughout repeated iterations. This implies that, from (3.1) and (3.2), if $\eta(t) = 0$, given a realizable output trajectory $y_d(t)$ and an appropriate initial condition x_0, there exists a unique control input $u_d(t)$ that generates the desired torque for the PMSM.

A5: Each output trajectory $y_{i-1}(t)$ can be measured without noise, i.e. $\xi = 0$ and thereby the error signal $y_d(t) - y_{i-1}(t)$ can be used in the construction of the

next command input.

A6: The input command of the i^{th} cycle, $u_i(t)$, is composed of a simple and fixed recursive law, $u_i(t) = F\left(u_{i-1}(t), y_d(t) - y_{i-1}(t)\right)$, where F is a function of the $(i-1)^{th}$ input $u_{i-1}(t)$ and the $(i-1)^{th}$ cycle error $y_d(t) - y_{i-1}(t)$.

Postulates A3 - A5 are somewhat strict requirements that are practically unachievable under experimental conditions. However, with the introduction of the forgetting factor (which is discussed in greater detail later), those requirements can be relaxed to some extent.

Typically, the most basic form of the recursive learning law is expressed as:

$$u_i(t) = u_{i-1}(t) + \Gamma e_{i-1}(t) \tag{3.3}$$

where

$$e_{i-1}(t) = y_d(t) - y_{i-1}(t) \tag{3.4}$$

and $\Gamma \in R$ is the positive definite learning gain; $u_i(t)$ and $u_{i-1}(t)$ are the control inputs of the current and previous cycles respectively; $e_{i-1}(t)$ is the tracking error of the previous cycle.

For convergence of the output trajectory to the desired one, i.e. as $|e_{i-1}| \to 0$ as $i \to \infty$, the following criterion must hold [87]:

$$|1 - cb\Gamma| < 1 \tag{3.5}$$

As previously described, only a partial knowledge of cb (in (3.1) and (3.2)) is required such that the learning gain Γ can be chosen to meet condition (3.5).

However, the basic P-type learning algorithm as given in (3.3) is not robust to perturbation from the initial state or output errors. By introducing a forgetting factor α in the learning process, the robustness of the P-type ILC in the presence of initialization errors, fluctuations of the plant dynamics and measurement noise

is increased. This has been rigorously proven mathematically as well as via experimental studies by Arimoto *et al* [88]-[91]. Therefore, with the forgetting factor, the learning law in (3.3) is modified to:

$$u_i(t) = (1 - \alpha)u_{i-1}(t) + \Gamma e_{i-1}(t) \tag{3.6}$$

where $0 < \alpha < 1$. Correspondingly, postulates A3 - A5 are relaxed to some extent as in the following:

A3': Repeatability of the initial condition is satisfied within an allowable level of deviation, i.e., $x_i(0) - x_0(0) = \delta_i$, $|\delta_i| \leq \varepsilon_1$ for some small $\varepsilon_1 > 0$.

A4': An allowable level of fluctuations $\eta_i(t)$ in the system dynamics must satisfy the condition $|\eta_i|_\infty \leq \varepsilon_2$ for some small $\varepsilon_2 > 0$.

A5': Each output trajectory $y_{i-1}(t)$ can be measured within a small specified noise level $\xi_{i-1}(t)$, i.e., $e_{i-1}(t) = y_d(t) - [y_{i-1}(t) + \xi_{i-1}(t)]$ where $|\xi_{i-1}|_\infty \leq \varepsilon_3$ for some small $\varepsilon_3 > 0$.

Nevertheless, while introduction of the forgetting factor provides additional robustness to the ILC scheme as described above, it is worthwhile to note that convergence of the output trajectory is limited to an α neighborhood of the desired one. To avoid the saturation of convergence due to the forgetting factor, frequency-domain iterative learning control (FILC) method based-on Fourier series expansion has been proposed in the later section.

Another factor to be considered in the application of the ILC in the PMSM is that the ILC employing *previous cycle feedback* (PCF) algorithm is essentially an open-loop control, thus it may be sensitive to small random perturbations or initial state resetting error [92], [93]. To overcome this shortcoming, the present error signal (i.e. *current cycle feedback*, CCF) is included in the learning law, without affecting the convergence properties of the ILC. In this circumstance, convergence

is solely determined by the PCF part, while the CCF part merely increases the stability of the ILC against random error signals. Therefore, modifying (3.6) yields the P-type ILC employing combined PCF and CCF technique that can be written as:

$$u_i(t) = (1-\alpha)u_{i-1}(t) + \Gamma e_{i-1}(t) + \Phi e_i(t) \tag{3.7}$$

Figure 3.2 shows the schematic diagram of the learning control scheme expressed in (3.7).

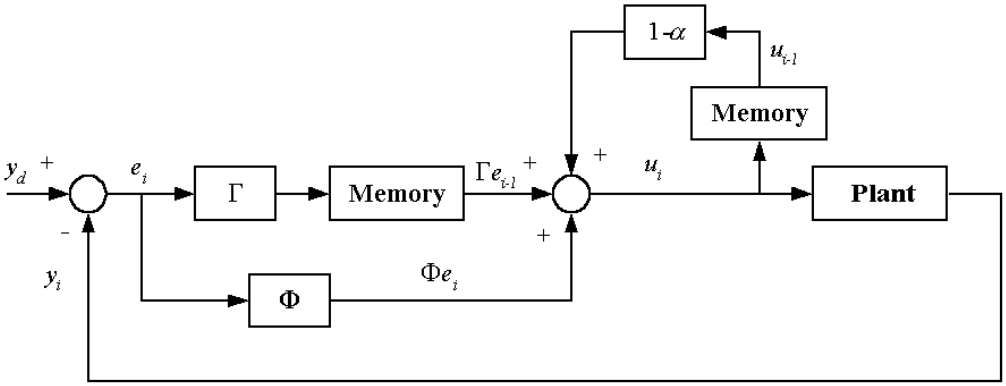

Figure 3.2: Iterative learning control configuration

The following section presents configurations and applications of the learning variable structure control (LVSC) and the frequency-domain iterative learning control (FILC) schemes, both of which are modified algorithms based on the basic concept of iterative learning control.

3.3 Configuration and Application of LVSC

Since both the LVSC and the FILC control strategies are modifications based on the basic ILC concept, similarly, they are designed for a repeatable control environment. A repeatable control system will repeat itself over a finite interval with respect to the given tracking target. In the learning variable structure control (LVSC) scheme, iterative learning control (ILC) is combined with variable structure

control (VSC) to improve robustness, while the frequency-domain iterative learning control (FILC) scheme is proposed to solve the problem caused by the introduction of forgetting factor α. In this section, the configuration and application of LVSC are explained in detail, and the FILC algorithm is described in the next section.

3.3.1 Problem formulation and LVSC configuration

The novel concept of learning variable structure control has been first systematically presented by Xu *et al* in [94]. Learning variable structure control is the synthesis of variable structure control (VSC) and iterative learning control. While VSC is used as usual to deal with system uncertainties, a learning mechanism is incorporated to learn the *equivalent control* required by the control task in a repetitive manner. In a sense, VSC provides feedback and the learning mechanism realizes feed-forward compensation. However, this type of feed-forward compensation is completely different from other feed-forward compensation approaches in that it only uses past control input and tracking error sequences to approximate the equivalent control. Owing to this important feature, the learning process is much less model-dependent, which is a strong desirable characteristic for any feed-forward compensation approach.

3.3.1.1 Problem formulation

Repeatable tracking control tasks

Consider an n^{th} order deterministic nonlinear uncertain dynamical system described by

$$\begin{cases} \dot{x}_j &= x_{j+1} \\ \dot{x}_n &= f(\boldsymbol{x},t) + b(\boldsymbol{x},t)u \end{cases} \tag{3.8}$$

where $\boldsymbol{x} = [x_1, \cdots, x_n]^T \in X \subseteq R^n$ is the physically measurable state vector; u is the control input; $f(\boldsymbol{x},t)$ and $b(\boldsymbol{x},t)$ are nonlinear uncertain functions.

Given a finite initial state $\boldsymbol{x}_i(0)$ and a finite time interval $[0,T]$ where i de-

notes the iteration sequence, the control objective is to design a VSC combined with iterative learning such that, as $i \to \infty$, the system state $\boldsymbol{x}_i$ of the nonlinear uncertain system (3.8) tracks the desired trajectory $\boldsymbol{x}_d = [x_{d,1}, \cdots, x_{d,n}]^T \in X_D \subseteq R^n$, where $\boldsymbol{x}_d \in C^1([0,T])$ and is generated by the following dynamics over $[0,T]$

$$\begin{cases} \dot{x}_{d,j} &= x_{d,j+1} \\ \dot{x}_{d,n} &= \beta(\boldsymbol{x}_d, t) + r(t) \end{cases} \tag{3.9}$$

where $\beta(\boldsymbol{x}_d, t) \in C(X_D \times [0,T])$ is a known function and $r(t) \in C([0,T])$ is a reference input. $\boldsymbol{x}_d \in C^1([0,T])$ ensures $\boldsymbol{x}_d \in C([0,T])$, $\dot{\boldsymbol{x}}_d \in C([0,T])$ and therefore $\boldsymbol{x}_d \in B([0,T])$ and $\dot{\boldsymbol{x}}_d \in B([0,T])$ as $[0,T]$ is a finite interval. As part of the repeatability condition, the initial states $\mathbf{x}_i(0) = \boldsymbol{x}_d(0)$ is available for all trials.

Switching surface

The switching surface of a basic VSC is defined as

$$\sigma_i = (x_{d,n} - x_{i,n}) + \sum_{j=1}^{n-1} \alpha_j (x_{d,j} - x_{i,j}) = \boldsymbol{\alpha}^T (\boldsymbol{x}_d - \boldsymbol{x}_i) \tag{3.10}$$

where $\boldsymbol{\alpha}^T = [\alpha_1, \cdots, \alpha_{n-1}, 1]$ and $\alpha_j (j = 1, \cdots, n-1)$ are chosen coefficients such that the polynomial $s^{n-1} + \alpha_{n-1} s^{n-2} + \alpha_{n-2} s^{n-3} + \cdots + \alpha_1$ is *Hurwitz* and s is a Laplace operator.

Assumptions

To derive an equivalent control, the following assumptions are proposed:

A1: $f(\boldsymbol{x}, t)$ is bounded by a known bounding function $f_{max}(\boldsymbol{x}, t)$, i.e., $|f(\boldsymbol{x}, t)| \leq f_{max}(\boldsymbol{x}, t)$ while $b(\boldsymbol{x}, t)$ is positive definite which is lower bounded by a known bounding function $b_{min}(\boldsymbol{x}, t)$ and is also upper bounded, i.e., $0 < \underline{b} \leq b_{min}(\boldsymbol{x}, t) \leq b(\boldsymbol{x}, t) \leq \overline{b}$ for some positive constants $\underline{b}$, $\overline{b}$ and $\forall (\boldsymbol{x}, t) \in X \times [0,T]$. It implies that $b^{-1}(\boldsymbol{x}, t) f(\boldsymbol{x}, t)$ is also bounded as $|b^{-1}(\boldsymbol{x}, t) f(\boldsymbol{x}, t)| \leq b_{min}^{-1}(\boldsymbol{x}, t) f_{max}(\boldsymbol{x}, t)$. The bounding functions $f_{max}(\boldsymbol{x}, t)$ and $b_{min}(\boldsymbol{x}, t)$ belong to $B(X \times [0,T]) \cap C(X \times [0,T])$.

A2: $\forall h \in f, b$, $h(\boldsymbol{x}, t) \in C(X \times [0,T])$ and $h(\boldsymbol{x}, t)$ satisfies the globally *Lipschitz*

condition, $\|h(\boldsymbol{x}_1,t)-h(\boldsymbol{x}_2,t)\| \leq l_h\|\boldsymbol{x}_1(t)-\boldsymbol{x}_2(t)\|$, $\forall t \in [0,T]$, $\forall \boldsymbol{x}_1, \boldsymbol{x}_2 \in X$ and for a positive constant $l_h < \infty$.

Equivalent control

Differentiating (3.10) with respect to time results

$$\dot{\sigma}_i = (\dot{x}_{d,n} - \dot{x}_{i,n}) + \sum_{j=1}^{n-1} \alpha_j (x_{d,j+1} - x_{i,j+1}) \tag{3.11}$$

Substituting (3.8) and (3.9) into (3.11) gives

$$\begin{aligned} \dot{\sigma}_i &= \sum_{j=1}^{n-1} \alpha_j (x_{d,j+1} - x_{i,j+1}) + \beta(\boldsymbol{x}_d,t) + r(t) - f_i - b_i u_i \\ &= g_i - f_i - b_i u_i \end{aligned} \tag{3.12}$$

where $f_i \doteq f(\boldsymbol{x}_i,t)$, $b_i \doteq b(\boldsymbol{x}_i,t)$, $g_i \doteq \sum_{j=1}^{n-1} \alpha_j (x_{d,j+1} - x_{i,j+1}) + g_d$, $g_d \doteq \beta(\boldsymbol{x}_d,t) + r(t)$. According to (3.12), making $\dot{\sigma}_i = 0$ obtains $x_i(t) = x_d(t)$, $\forall t \in [0,T]$ and gives the following expression for the *equivalent control*

$$u_{eq} = b_i^{-1}(g_i - f_i) = b_d^{-1}(g_d - f_d), \tag{3.13}$$

where $b_d \doteq b(\boldsymbol{x}_d,t)$, $f_d \doteq f(\boldsymbol{x}_d,t)$. Since $\boldsymbol{x}_d \in B([0,T])$, then $g_d \in B([0,T])$ as $\beta(\boldsymbol{x}_d,t) \in C(X_D \times [0,T])$, $r(t) \in C([0,T])$ and $[0,T]$ is a finite interval. According to A1, $b_d^{-1} \leq \underline{b}^{-1}$ and $\boldsymbol{x}_d \in B([0,T])$ ensures $f_d \in B([0,T])$, hence $u_{eq} \in B([0,T])$.

3.3.1.2 LVSC configuration

The proposed LVSC has a very simple structure consisting of two components in additive form: a standard switching control mechanism based on the known upper bounds using a continuous smoothing function, and a learning mechanism which simply adds up past VSC sequence. The LVSC is given below

$$u_i = u_{v,i} + u^* sat(u_{l,i-1}, u^*), \qquad u_{l,0} = 0 \tag{3.14}$$

$$u_{v,i} = \zeta\sigma_i + \rho sat(\sigma_i, \varepsilon) \tag{3.15}$$

$$u_{l,i} = u_{v,i} + u^* sat(u_{l,i-1}, u^*) \tag{3.16}$$

$$sat(m,n) \doteq \begin{cases} m/n & |m| \leq n \\ sgn(m) & |m| > n \end{cases} \tag{3.17}$$

where ζ, ρ, ε and u^* are positive-definite constants. u^* is a sufficiently large constant such that

$$u^* \geq |u_{eq}(t)| \tag{3.18}$$

for the whole interval $t \in [0,T]$ to ensure the learnability. Note that u^* can be either decided from the real limitation of the physical process, or simply chosen to be an arbitrarily large but finite virtual bound which does not affect the VSC part. Equation (3.15) is a VSC law which replaces the signum function $sgn(\sigma_i)$ with the saturation function $sat(\sigma_i, \varepsilon)$ to eliminate chattering. Since $u_{v,i}$ is continuous with respect to σ_i, g_i, $b_{min}(\boldsymbol{x}_i,t)$ and $f_{max}(\boldsymbol{x}_i,t)$, $b_{min}(\boldsymbol{x}_i,t) \in C(X \times [0,T])$, $f_{max}(\boldsymbol{x}_i,t) \in C(X \times [0,T])$ according to A1, $\sigma_i \in C(X \times [0,T])$, $g_i \in C(X \times [0,T])$ as $x_d \in C([0,T])$, hence $u_{v,i} \in C(X \times [0,T])$.

Since $b_d \neq 0$, it can be shown by (3.13) that, if $\beta(\boldsymbol{x}_d,t) + r(t) - f(\boldsymbol{x}_d,t) \neq 0$, then $u_{eq} \neq 0$. It is impossible to generate u_{eq} by using the VSC law (3.15), since when $\boldsymbol{x}_i \to \boldsymbol{x}_d$, $\sigma_i \to 0$, then $u_{v,i} \to 0 \neq u_{eq}$. To produce u_{eq} or to achieve perfect tracking using a smooth control input, (3.16) introduces the simple structure of the proposed learning control $u_{l,i}$. This learning control signal is the same as the final control output u_i, and it comprises the learning control signal of the previous iteration $u_{l,i-1}$ and the current iteration VSC output $u_{v,i}$. As $i \to \infty$, $u_{v,i} \to 0$ and $u_{l,i}(= u_i) \to u_{eq}$.

3.3.1.3 Fourier series based iterative learning

In this subsection, we further address important issues arising from practical considerations and implement learning control in frequency domain by means of Fourier series expansion. First, it should be noted that the repeatability of the control environment implies only countable integer frequencies being involved in the equivalent

control profile, this ensures the implementability of constructing componentwise learning in frequency domain. Secondly, nowadays all advanced control approaches have to be implemented using microprocessing technology. According to the sampling theory, LVSC needs only to learn a finite number of frequencies limited by one half of the sampling frequency $\omega_s = 2\pi/T_s$ where T_s is the sampling interval. Any attempt to learn and manipulate frequencies above that limit will be completely meaningless. Thirdly, most real systems can be characterized as low-pass filter because their bandwidth is much lower than the sampling frequency. It is sufficient for LVSC to take into account only a small portion of Fourier series in such cases.

The final control signal u_i is utilized as q-axis reference compensation current and is required to compensate the harmonic components of no more than the 12^{th} order of the synchronous frequency. In the experimental investigations, the highest synchronous frequency is 5 Hz when motor is operated at 100 rpm. This is because torque pulsations will automatically be filtered by the inertia, when motor is operated at speeds higher than 100 rpm. There is need to compensate these torque pulsations if they cannot be reflected in motor speed. Therefore, the spectrum of u_{eq}, σ_i, $u_{v,i}$, $u_{l,i}$ and $u^* sat(u_{l,i-1}, u^*)$ is located in relatively low frequency band ($\omega_b = 2\pi \times 5 \times 12 = 377$ rad/sec) comparing to sampling frequency ($\omega_s = 2\pi/T_s = 2\pi/(2.5 \times 10^{-4}) = 2.51 \times 10^4$ rad/sec). This means $\omega_b < \omega_s/2$, consequently, u_{eq}, σ_i, $u_{v,i}$, $u_{l,i}$ and $u^* sat(u_{l,i-1}, u^*)$ can be expressed in the following truncated Fourier Linear Combiners form

$$\begin{cases} u_{eq} = \boldsymbol{\Psi}^T \boldsymbol{\nu} \\ u_{l,i} = \boldsymbol{\Psi}^T \boldsymbol{\nu}_i \\ u_{v,i} = \boldsymbol{\Psi}^T \boldsymbol{\theta}_i \\ u^* sat(u_{l,i-1}, u^*) = \boldsymbol{\Psi}^T \hat{\boldsymbol{\nu}}_i \end{cases} \tag{3.19}$$

where

$$\boldsymbol{\theta}_i = \frac{2}{T}\int_0^T u_{v,i}\boldsymbol{\Psi}_1 dt \tag{3.20}$$

$$\hat{\boldsymbol{\nu}}_{i-1} = \frac{2}{T}\int_0^T u^* sat(u_{l,i-1}, u^*)\boldsymbol{\Psi}_1 dt \tag{3.21}$$

$$\begin{aligned}\boldsymbol{\Psi} &= [\,0.5 \;\; \cos\omega t \;\; \cos 2\omega t \;\; \cdots \;\; \cos N\omega t \\ &\qquad \sin\omega t \;\; \sin 2\omega t \;\; \cdots \;\; \sin N\omega t\,]^T \\ \boldsymbol{\Psi_1} &= [\,1 \;\; \cos\omega t \;\; \cos 2\omega t \;\; \cdots \;\; \cos N\omega t \\ &\qquad \sin\omega t \;\; \sin 2\omega t \;\; \cdots \;\; \sin N\omega t\,]^T \\ N &\geq \frac{\omega_b}{\omega} \qquad \omega = \frac{2\pi}{T}\end{aligned}$$

The frequency domain learning law can be obtained from (3.16) and (3.19) as

$$\boldsymbol{\nu}_i = \hat{\boldsymbol{\nu}}_{i-1} + \boldsymbol{\theta}_i \tag{3.22}$$

Since u_{eq} is invariant over every iteration, each element of $\boldsymbol{\nu}$ is constant. The frequency domain learning law (3.22) produces estimate $\boldsymbol{\nu}_i$ which converges to $\boldsymbol{\nu}$ as $i \to \infty$. Fig. 3.3 shows Fourier transformation of the learning control signal, in which $u_{l,i}$ is the original signal without process, and $\bar{u}_{l,i}$ is the final control signal after transformation.

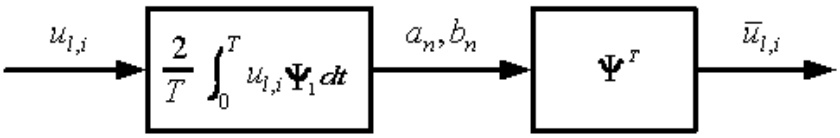

Figure 3.3: Block diagram of Fourier transformation of the learning control signal

The main advantage of Fourier series based learning is the enhancement of LVSC robustness and the improvement of tracking performance. Note that there always exist system noise or other small non-repeatable factors even in a repeatability dominant control environment. Accumulation of those tiny components contained

in control sequence $u_{v,i}$ and tracking error sequence σ_i may degrade the approximation precision of learning control sequence $u_{l,i}$. Fourier series based learning mechanism, on the other hand, updates coefficients $\boldsymbol{\nu}_i$, $\hat{\boldsymbol{\nu}}_{i-1}$ and $\boldsymbol{\theta}_i$ of the learnt frequency components $\boldsymbol{\Psi}$ and those coefficients are calculated according to (3.20) which takes integration of control sequence $u_{v,i}$ and tracking error sequence σ_i over the entire control interval $[0, T]$. In the sequel, the integration process (3.20) and (3.21) plays the role of an averaging operation on the two noisy sequences $u_{v,i}$ and σ_i and is able to remove the majority of those high frequency components.

3.3.2 Application of LVSC on the PMSM drive system

In this subsection, the LVSC schemes used for learning the desired stator current waveform for pulsating torque minimization are described. As the torque pulsations are of concern only in steady-state operation of the motor, the LVSC is applied only when the motor reaches steady state. Two different LVSC compensating schemes are presented: one for minimizing the pulsating torque and the other for minimizing the speed ripples.

3.3.2.1 Torque control with LVSC pulsating torque compensation scheme

In this torque control scheme as illustrated in Fig. 3.4, there is no outer closed-loop speed controller. The reference torque τ_m^* is taken as the input command. The drive scheme is basically a torque controller employing current-regulated PWM with sinusoidal current reference (CRPWM) with an additional LVSC controller that is responsible for shaping the optimal reference current profile to reduce the pulsating torque components. When the LVSC system is deactivated, only sinusoidal phase currents from power source are injected into the plant. When the LVSC system is activated, using the error signal between the desired and instantaneous motor torque, the LVSC torque controller learns and then generates the desired *equivalent*

control u_{eq}, i.e. compensating current profile i^*_{qs-2} of appropriate magnitude and phase corresponding to the pulsating torque components. This additional reference current is then added to the constant reference current i^*_{qs-1}. This process is performed iteration by iteration and consequently, the pulsating torque components reduce in magnitude as the number of iteration increases, resulting in a smoother motor torque that tracks the constant reference torque τ^*_m. The torque control scheme needs instantaneous torque information as the feedback signal, which can be obtained either from a high-bandwidth torque transducer output or from an on-line torque estimator implemented in software. A more detailed description of the on-line torque estimator is presented in Section 3.5.

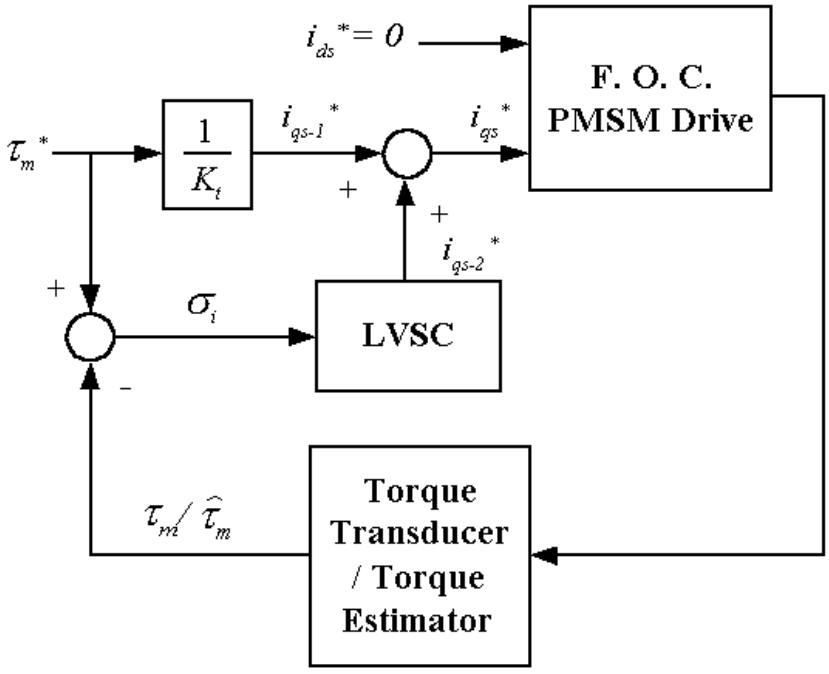

Figure 3.4: Configuration for LVSC torque control scheme

In this scheme, the design of the learning system is performed using electrical angle θ_e instead of time t as the iteration axis. This is more appropriate because torque pulsations occur at frequencies of integer multiples of the fundamental electrical frequency f_e (synchronous frequency) as presented in the previous chapter. Besides, without the outer speed control loop, the motor speed can not be strictly

kept constant, which makes it difficult to find a fixed time interval as the learning period, T. Therefore, the learning period for torque scheme is taken as the period of one electrical cycle or 2π electrical radians, while in the speed scheme time t is still used as the iteration axis.

To develop the controller, first, the total motor torque described in Chapter 2 is reproduced as:

$$\tau_m = \frac{3}{2} P_p \psi_d i_{qs} + \tau_{cog} + \tau_{\Delta i} \tag{3.23}$$

where τ_{cog} and $\tau_{\Delta i}$ are the torque ripples due to cogging and current measurement error, respectively. As these torque ripples are independent of i_{qs}, the linear current-torque relationship results in a switching surface of relative degree 0:

$$\sigma_i(\theta_e) = \tau_m^* - \tau_{m,i}(\theta_e) \tag{3.24}$$

In the analysis, perfect tracking of the inner loop current controller is assumed:

$$i_{qs,i}^*(\theta_e) = i_{qs,i}(\theta_e) \tag{3.25}$$

Therefore, the task for the LVSC controller is to modify the profile of $i_{qs,i}^*(\theta_e)$ such that $\tau_{m,i}(\theta_e) \to \tau_m^*$ when $i \to \infty$, and the LVSC controller becomes:

$$\begin{aligned} u_i &= u_{v,i} + u^* sat(u_{l,i-1}, u^*) \\ &= \zeta \sigma_i + \rho sat(\sigma_i, \varepsilon) + u^* sat(u_{i-1}, u^*) \\ &\Downarrow \\ i_{qs-2,i}^* &= \zeta_1 \sigma_i + \rho_1 sat(\sigma_i, \varepsilon_1) + u^* sat(i_{qs-2,i-1}^*, u^*) \end{aligned} \tag{3.26}$$

where ζ_1 and ρ_1 are positive coefficients which can be set to ensure robustness of the VSC. u^* can be defined equal to 10 or above, which is the upper bound value of the q-axis current to ensure the learnability.

3.3.2.2 Closed-loop PI speed control with LVSC speed ripple compensation

In the previously described scheme, LVSC is applied in the torque control loop to minimize the pulsating torque. The direct consequence of the torque pulsations is the presence of ripples in the speed. In this scheme, the LVSC is employed in the speed control loop with the objective of minimizing these speed ripples. Compared with the torque ripple minimization scheme previously described, this scheme has the advantage that it does not require the use of the torque estimator or torque transducer since no direct torque control is performed. Therefore, it is relatively simple and easily implementable.

The closed-loop speed control with LVSC speed ripple compensation scheme is shown in Fig. 3.5. This scheme is essentially a conventional closed-loop PI speed control scheme with an additional LVSC speed ripple compensator applied in parallel with the PI speed controller. The input to the speed controller is the speed error $\omega_m^* - \omega_m$. In order to maintain the speed at or around the speed set-point, the PI speed controller generates the desired torque signal, τ_m^* (which results in the reference current i_{qs}^* when divided by the motor torque constant $K_t = \frac{3}{2}P_p\psi_d$). To a certain extent, the PI speed controller compensates speed ripples. However, the PI speed controller has a limited bandwidth and it cannot fully reject the periodic speed ripples. Therefore, a significant amount of residual speed ripples still exist in the conventional closed-loop control system. With LVSC compensation, using the error signal between the desired and instantaneous motor speed, the LVSC speed controller learns and then generates the desired compensating current profile, i_{qs-2}^*, to neutralize the speed ripple components. This additional reference current, i_{qs-2}^*, is added to i_{qs-1}^*, resulting in the final q-axis reference current i_{qs}^*. This iterative correction is applied repeatedly cycle by cycle, with each cycle having a period of one electrical cycle or a period of fixed time interval (because speed is kept

constant in closed-loop speed control, a period of one electrical cycle has a fixed time interval). As a result, the speed ripple components reduce in magnitude as the number of iteration increases; resulting in a smoother motor speed that tracks the constant reference speed ω_m^*.

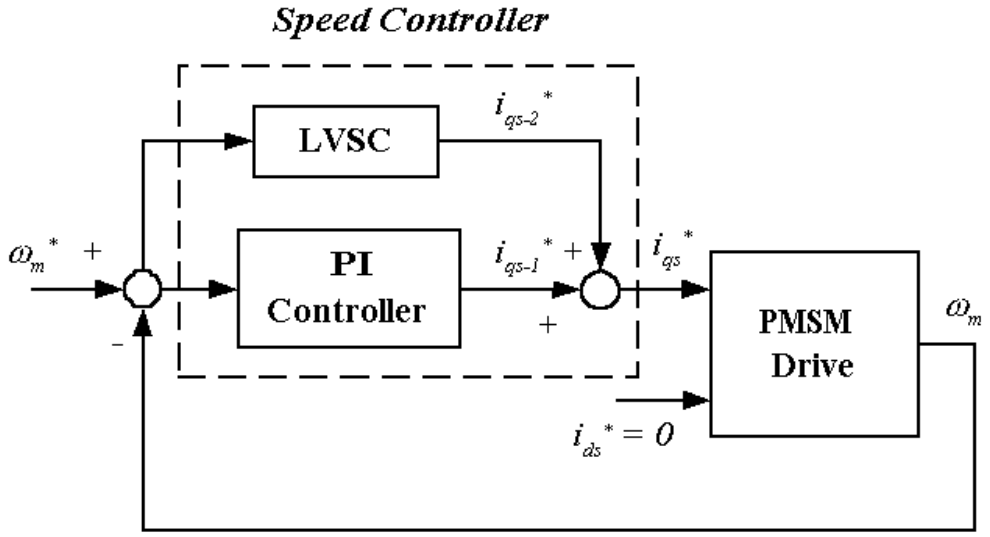

Figure 3.5: Configuration for closed-loop speed scheme with LVSC speed ripple compensation

To determine the controller, the equation of motion is re-written as:

$$\begin{aligned} \frac{d\omega_m(t)}{dt} &= -\frac{B}{J}\omega_m(t) + \frac{1}{J}\tau_m(t) - \frac{1}{J}\tau_L(t) \\ &= -\frac{B}{J}\omega_m(t) + \frac{K_t}{J}i_{qs}(t) - \frac{1}{J}\tau_L(t) \end{aligned} \tag{3.27}$$

Similarly, the first order system (current - angular velocity) results in a switching surface of relative degree 0:

$$\sigma_i(t) = \omega_m^* - \omega_{m,i}(t) \tag{3.28}$$

Hence, the task for the LVSC controller is to modify the profile of $i_{qs,i}^*(t)$ such that $\omega_{m,i}(t) \to \omega_m^*$ when $i \to \infty$, and the LVSC controller becomes:

$$i_{qs-2,i}^* = \zeta_2\sigma_i + \rho_2 sat(\sigma_i, \varepsilon_2) + u^* sat(i_{qs-2,i-1}^*, u^*) \tag{3.29}$$

where ζ_2 and ρ_2 are positive coefficients which can be set to ensure the robustness of VSC. u^* can be defined equal to 10 or above, which is the upper bound value of the q-axis current to ensure the learnability.

3.4 Configuration and Application of FILC

In this section, configuration and application of the FILC algorithm are presented in detail.

3.4.1 FILC algorithm

The introduction of the forgetting factor in the basic ILC scheme only ensures the tracking errors within a certain bound, and further improvement is limited with the consideration of robustness. Under such conditions, we further implemented the learning control in frequency domain by means of Fourier series expansion. Fourier series based learning enhances the robustness property of iterative learning while maintaining the possibility of reducing tracking errors to zero theoretically. Note that there always exists system noise or other small non-repeatable factors in the system. Accumulation of those components contained in u_i may degrade the approximation precision of the controller for each new trial. Fourier series-based learning mechanism, on the other hand, updates coefficients of the learned frequency components over the entire learning period, which takes an averaging operation on noise and is able to remove the majority of noise and non-repeatable factors. Consequently, there is no need to introduce the forgetting factor in this scheme. The repeatability of torque (or speed) ripples implies that only countable integer multiples of the frequency are involved. This ensures the feasibility of constructing componentwise learning in frequency domain. The schematic diagram of the frequency-domain iterative learning control is shown in Fig. 3.6, and the

corresponding control law is given by:

$$u_i(t) = FT(u_{i-1}(t)) + \Gamma e_{i-1}(t) + \Phi e_i(t), \tag{3.30}$$

where

$$FT(u_{i-1}(t)) = \mathbf{\Psi}^T \cdot \frac{2}{T} \int_0^T u_{i-1}(t) \mathbf{\Psi_1} dt \tag{3.31}$$

$$\begin{aligned} \mathbf{\Psi} &= [\, 0.5 \;\; \cos\omega t \;\; \cos 2\omega t \;\; \cdots \;\; \cos N\omega t \\ &\qquad \sin\omega t \;\; \sin 2\omega t \;\; \cdots \;\; \sin N\omega t \,]^T \\ \mathbf{\Psi_1} &= [\, 1 \;\; \cos\omega t \;\; \cos 2\omega t \;\; \cdots \;\; \cos N\omega t \\ &\qquad \sin\omega t \;\; \sin 2\omega t \;\; \cdots \;\; \sin N\omega t \,]^T \\ \omega &= \frac{2\pi}{T}, \qquad N = 12 \end{aligned}$$

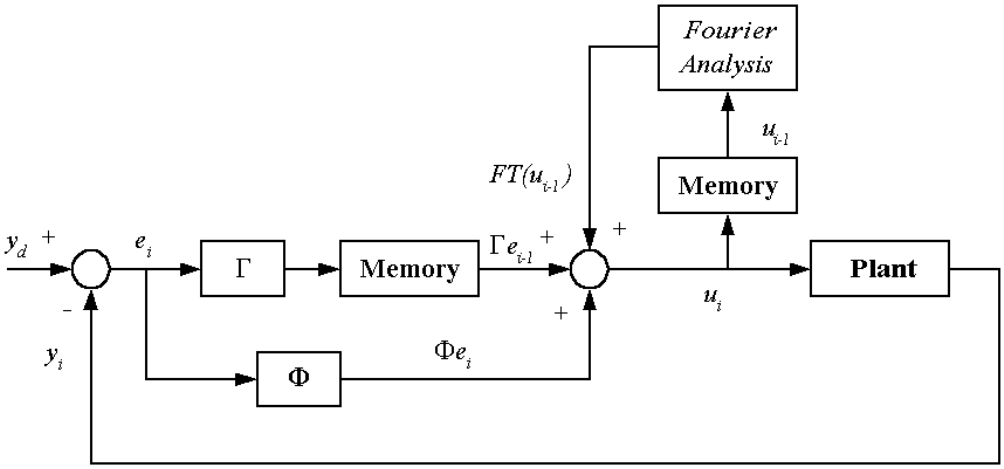

Figure 3.6: Frequency-domain iterative learning control configuration

3.4.2 Application of FILC on the PMSM Drive System

In this subsection, the FILC compensation scheme used for learning the desired stator current waveform for pulsating torque minimization are described. Similarly, two different compensating schemes are presented: one for minimizing the pulsating torque and the other for minimizing the speed ripples.

3.4.2.1 Torque control scheme with FILC pulsating torque compensation

The torque control scheme with FILC compensation as illustrated in Fig. 3.7 has the same structure as that presented in Subsection 3.3.2.1. The only difference between the two schemes is that the pulsating torque compensation controller is implemented based on FILC algorithm in this case, not LVSC. The same description holds good as that in Subsection 3.3.2.1, and therefore it is not repeated here. Again, we use electrical angle θ_e instead of time t as the iteration axis in this scheme.

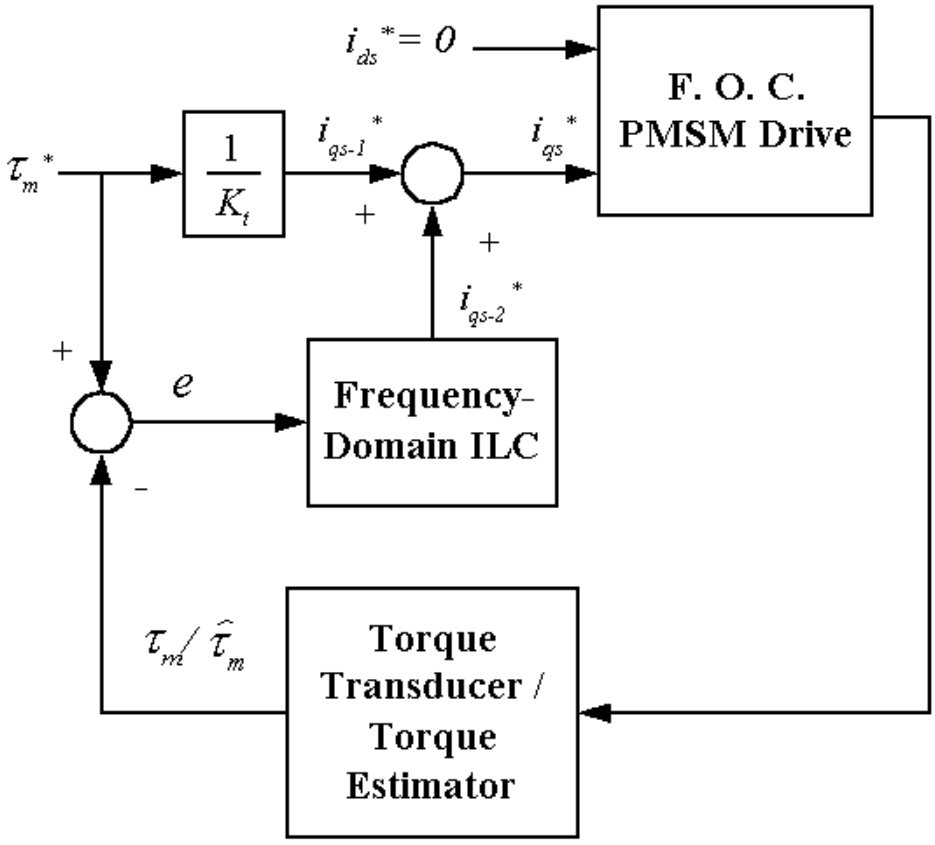

Figure 3.7: Configuration for FILC torque control scheme

To determine the learning gain Γ, first, the total motor torque described in Chapter 2 is reproduced as:

$$\tau_m = \frac{3}{2} P_p \psi_d i_{qs} + \tau_{cog} + \tau_{\Delta i} \tag{3.32}$$

The linear current - torque relationship can be re-written as:

$$\tau_{m,i}(\theta_e) = b(\theta_e) i_{qs,i}(\theta_e) + w(\theta_e) \qquad \forall \theta_e \in [0, 2\pi] \tag{3.33}$$

where

$$b(\theta_e) = \frac{3}{2} P_p \psi_d(\theta_e) \tag{3.34}$$

and $w(\theta_e)$ represents the sum of $\tau_{cog}(\theta_e) + \tau_{\Delta i}(\theta_e)$.

In the analysis, perfect tracking of the inner loop current controller is assumed:

$$i^*_{qs,i}(\theta_e) = i_{qs,i}(\theta_e) \tag{3.35}$$

Therefore, the task for the FILC controller is to modify the profile of $i^*_{qs,i}(\theta_e)$ such that $\tau_{m,i}(\theta_e) \rightarrow \tau^*_m$ when $i \rightarrow \infty$. Denoting the torque error term $e_i(\theta_e)$ by:

$$e_i(\theta_e) = \tau^*_m - \tau_{m,i}(\theta_e) \tag{3.36}$$

the learning law from (3.30) becomes:

$$i^*_{qs-2,i}(\theta_e) = FT\left(i^*_{qs-2,i-1}(\theta_e)\right) + \Gamma e_{i-1}(\theta_e) + \Phi e_i(\theta_e) \tag{3.37}$$

Applying the convergence condition from (3.5) yields the following:

$$|1 - b(\theta_e)\Gamma| < 1 \tag{3.38}$$

Denoting $0 < b(\theta_e) \leq b_{max}$, the inequality in (3.38) can be solved as:

$$0 < \Gamma < \frac{2}{b_{max}} \tag{3.39}$$

From the knowledge of the range of $\psi_d(\theta_e)$ and (3.34), b_{max} and hence, Γ can be determined. To achieve a faster rate of convergence, the value of Γ should approach $2b^{-1}_{max}$. However, a conservative choice of Γ that ensures stability and reasonably fast convergence would suffice. Theoretically the CCF gain, Φ, does not affect the convergence in the iteration axis of the learning controller. However, having Φ that is too large will cause over-amplification of error or noise signals

in the input updating and the corresponding control input will tend to be large, leading to the eventual divergence of the output. As before, a conservative choice of Φ such that $\Phi \leq \Gamma$ would suffice in producing good results. In the Fourier series expansion, parameter N can be chosen such that the process covers the N^{th} order harmonics of the fundamental frequency, and here it is set as 12.

During the first trial, i.e. at the 0^{th} iteration ($i = 0$), the initial value of i^*_{qs-2} is set to zero. As the iteration progresses, i^*_{qs-2} will approach the optimal value that cancels out the pulsating torque. However, it is not vital to set i^*_{qs-2} to zero at the first trial. Using sufficiently accurate pre-determined values of i^*_{qs-2} at the first trial would greatly increase the rate of convergence of the algorithm at which the torque pulsations are minimized. Nevertheless, as one of the primary advantages of the FILC is that it does not require any prior off-line computation, numerical pre-determination of the initial values of i^*_{qs-2} is not performed in this work so as to preserve the advantage of the FILC over the pre-programmed stator current excitation scheme.

3.4.2.2 Closed-loop PI speed control with FILC speed ripple compensation

In this scheme, the FILC is employed in the speed control loop with the objective of minimizing these speed ripples. The closed-loop speed control with FILC speed ripple compensation scheme is shown in Fig. 3.8. Again, it has the same structure as that described in Subsection 3.3.2.2 except the compensation controller being FILC, and hence it is not repeated here.

To determine the learning gain, the equation of motion is re-written as:

$$\frac{d\omega_m(t)}{dt} = -\frac{B}{J}\omega_m(t) + \frac{1}{J}\tau_m(t) - \frac{1}{J}\tau_L(t) \tag{3.40}$$

Assuming perfect tracking of the inner-loop current controller:

$$\tau_m(t) = \tau^*_m(t) = K_t i^*_{qs}(t) \tag{3.41}$$

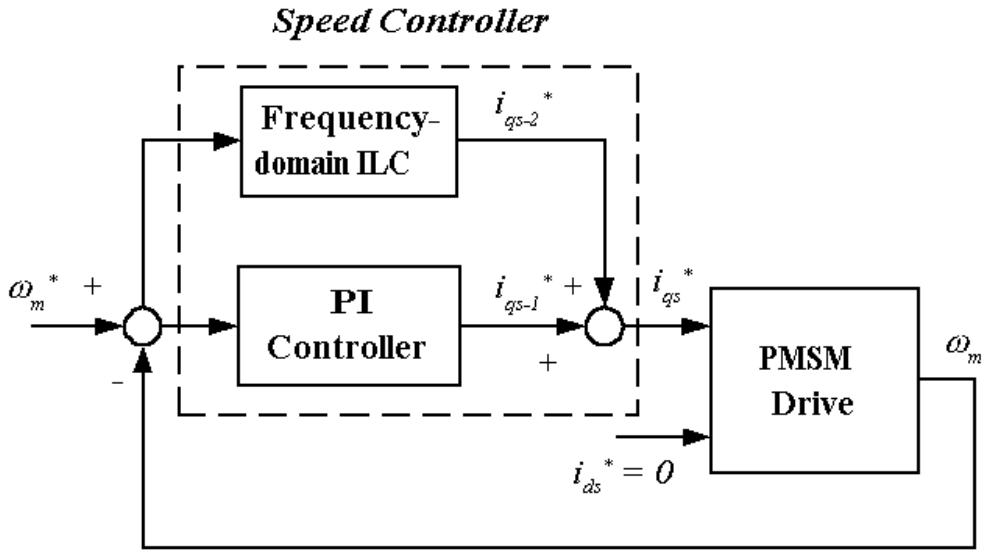

Figure 3.8: Configuration for closed-loop speed scheme with FILC speed ripple compensation

and substituting (3.41) into (3.40) yields:

$$\dot{\omega}_m(t) = a_1\omega_m(t) + b_1(t)i_{qs}^*(t) + w_1(t) \tag{3.42}$$

where the subscripts '1' in a_1, b_1 and w_1 are for the sake of distinguishing between the notations a, b and w used in both (3.33) and (3.42). Here, $a_1 = -\frac{B}{J}$, $b_1(t) = \frac{K_t(t)}{J}$ and $w_1(t) = -\frac{1}{J}\tau_L(t)$.

The task for the learning controller is to modify the profile of $i_{qs,i}^*(t)$ by generating $i_{qs-2,i}^*(t)$ such that $\omega_{m,i}(t) \to \omega_m^*$ when $i \to \infty$. Denoting

$$e_{i-1}(t) = \omega_m^* - \omega_{m,i-1}(t) \tag{3.43}$$

and applying the P-type FILC employing combined PCF and CCF algorithm from (3.30) yields the learning law as expressed in (3.37), reproduced in the following:

$$i_{qs-2,i}^*(t) = FT\left(i_{qs-2,i-1}^*(t)\right) + \Gamma e_{i-1}(t) + \Phi e_i(t) \tag{3.44}$$

Applying the convergence condition in (3.5) produces the following inequality:

$$|1 - b_1(t)\Gamma| < 1 \tag{3.45}$$

As in (3.38) and (3.39), the range of the learning gain Γ can be determined by (3.45). The analyses of the CCF gain Φ are similar to those described in the closed-loop iterative learning torque control scheme in Subsection 3.4.2.1. Thus, Φ can be chosen such that $\Phi \leq \Gamma$.

3.5 A High Gain Torque Estimator

A pre-requisite for the proper functioning of the proposed LVSC and FILC torque control schemes is the assumption of the existence of the instantaneous torque feedback information. For high-performance instantaneous torque control, the torque feedback must accurately reflect any instantaneous variation in the developed motor torque. To obtain the torque feedback signal, one way is to directly measure the motor torque by using a torque transducer (either the shaft torque transducer or a stator reaction torque transducer, the former measuring load torque while the latter measuring motor torque, differing by the inertial torque $J\frac{d\omega}{dt}$ term). However, this direct measurement method is not preferred for servo control applications, as torque transducers are disadvantaged due to their high costs. Therefore, alternative means of obtaining the torque feedback information is essential. In this section, the design of an on-line torque estimator that employs the high gain observer principle to estimate the flux is presented.

The dynamic electrical subsystem of the PMSM in (2.43) and (2.44) can be re-written in the state-space form as:

$$\dot{\boldsymbol{x}} = \boldsymbol{A}\boldsymbol{x} + \boldsymbol{B}\boldsymbol{u} + \boldsymbol{D}\boldsymbol{\psi} \tag{3.46}$$

where

$$\boldsymbol{x} = \begin{bmatrix} i_{ds} \\ i_{qs} \end{bmatrix} \quad \boldsymbol{u} = \begin{bmatrix} v_{ds} \\ v_{qs} \end{bmatrix} \quad \boldsymbol{\psi} = \begin{bmatrix} \psi_d \\ \psi_q \end{bmatrix}$$
$$\boldsymbol{A} = \begin{bmatrix} -\frac{r_s}{L_s} & \omega_e \\ -\omega_e & -\frac{r_s}{L_s} \end{bmatrix} \quad \boldsymbol{B} = \begin{bmatrix} \frac{1}{L_s} & 0 \\ 0 & \frac{1}{L_s} \end{bmatrix} \quad \boldsymbol{D} = \begin{bmatrix} 0 & \omega_e \\ -\omega_e & 0 \end{bmatrix}. \tag{3.47}$$

The quantities to be estimated are the d, q-axes flux linkage terms, ψ_d and ψ_q. Note that although ψ_q should equal zero theoretically, it still has small ripples around zero like current term i_{ds}. Therefore, we include this part into torque estimation. Consider (3.46), where currents, speed can be measured and motor parameters are known. Thus, application problems reduce to the estimation of unknown inputs, i.e. flux linkage, from the state measurements where the input and the state are related by a first order differential equation [76].

Suppose $\boldsymbol{z}$ represent d, q-axes currents, $\boldsymbol{y}$ comprise all known state variable components including d, q-axes currents and voltages and $\boldsymbol{x}$ are d, q-axes flux linkage to be estimated. They are related by a relationship

$$\dot{\boldsymbol{z}} = \boldsymbol{y} + \boldsymbol{x}. \tag{3.48}$$

Re-writing (3.48), we obtain

$$\boldsymbol{x} = \dot{\boldsymbol{z}} - \boldsymbol{y} \tag{3.49}$$

and by filtering both sides of (3.49) with a low pass filter we get

$$\frac{1}{\tau s + 1}\boldsymbol{x} = \frac{1}{\tau s + 1}(s\boldsymbol{z} - \boldsymbol{y}) \tag{3.50}$$

where $\tau > 0$ is the filter time constant and $s = j\omega$ is the Laplace operator. Then the following holds:

$$\frac{1}{\tau s + 1}\boldsymbol{x} = \frac{\boldsymbol{z}}{\tau} - \frac{1}{\tau s + 1}(\frac{\boldsymbol{z}}{\tau} + \boldsymbol{y}) \tag{3.51}$$

Denoting

$$\boldsymbol{\varepsilon} = \frac{1}{\tau s + 1}(\frac{\boldsymbol{z}}{\tau} + \boldsymbol{y}) \tag{3.52}$$

we see that the estimation of $\boldsymbol{x}$ can be found as

$$\hat{\boldsymbol{x}} = \frac{\boldsymbol{z}}{\tau} - \boldsymbol{\varepsilon}. \tag{3.53}$$

Hence, with the parameter τ chosen carefully, flux linkage can be determined from

$$\begin{bmatrix} \hat{\psi}_d \\ \hat{\psi}_q \end{bmatrix} = \begin{bmatrix} 0 & \frac{\omega_e}{L_s} \\ -\frac{\omega_e}{L_s} & 0 \end{bmatrix}^{-1} \begin{bmatrix} \frac{i_{ds}}{\tau} - \varepsilon_d \\ \frac{i_{qs}}{\tau} - \varepsilon_q \end{bmatrix} \tag{3.54}$$

where

$$\begin{bmatrix} \varepsilon_d \\ \varepsilon_q \end{bmatrix} = \frac{1}{\tau s+1} \begin{bmatrix} \frac{1}{\tau} - \frac{r_s}{L_s} & \omega_e \\ -\omega_e & \frac{1}{\tau} - \frac{r_s}{L_s} \end{bmatrix} \begin{bmatrix} i_{ds} \\ i_{qs} \end{bmatrix} + \begin{bmatrix} \frac{1}{L_s} & 0 \\ 0 & \frac{1}{L_s} \end{bmatrix} \begin{bmatrix} v_{ds} \\ v_{qs} \end{bmatrix} \tag{3.55}$$

Consequently, motor torque can be estimated by

$$\hat{\tau}_m = \frac{3}{2} P_p (\hat{\psi}_d i_{qs} - \hat{\psi}_q i_{ds}) \tag{3.56}$$

During the actual operation of the PMSM, it was observed that the motor speed consists of not only the sixth and twelfth harmonic ripples, but also the first and second harmonic ripples as well. From the analysis of torque pulsations in Chapter 2, the source of these low-order harmonic speed ripples is very likely due to current measurement error that produces the first and second order harmonic torque pulsations. However, those torque pulsations are not reflected in the estimated torque signal using the high gain observer technique. This is because the current measurement error is not in the dynamic model of the motor that is used in the flux observer. To compensate for these low-order harmonic torque pulsations, an additional torque ripple estimator is employed. This torque ripple estimator scheme has been applied to a reluctance synchronous machine in [74], and it essentially uses the speed ripple information to determine the magnitude of the torque ripple. The same scheme has been extended to measure torque ripples in PMSM due to current offset and current scaling errors.

From the equation of motion in (2.25), the following can be expressed:

$$\tau_0 + \Delta\tau = J \frac{d(\omega_0 + \Delta\omega)}{dt} + B(\omega_0 + \Delta\omega) + \tau_L \tag{3.57}$$

where τ_0 is the average motor torque, $\Delta\tau$ is the low-order harmonic torque ripple, ω_0 is the average motor speed and $\Delta\omega$ is the low-order harmonic speed ripple. At steady-state operation, the average motor torque equals to the sum of the load torque and the frictional torque (as ω_0 is constant, hence, $J\frac{d\omega_0}{dt} = 0$):

$$\tau_0 = B\omega_0 + \tau_L \tag{3.58}$$

Therefore, substituting (3.58) into (3.57) yields the following equation:

$$\Delta\tau = J\frac{d\Delta\omega}{dt} + B\Delta\omega \approx J\frac{d\Delta\omega}{dt} \tag{3.59}$$

where it has been assumed that $B\Delta\omega \approx 0$.

Assuming that the effect of the sixth and twelfth torque harmonics are absent in the motor speed, as the higher frequency ripples are naturally filtered off by the system inertia, the estimated torque ripple resulting from current measurement error can be evaluated from equation (3.59). However, in practice a low-pass filter with cutoff frequency set at slightly above the second order harmonic frequency is used to attenuate any sixth and twelfth order harmonic ripples that are present in the estimated torque ripple signal in equation (3.59). Writing

$$\hat{\tau}_{m2} = J\frac{d\Delta\omega}{dt} \tag{3.60}$$

as the estimated low-order harmonic torque ripple that is due to current measurement error, and denoting the estimated torque using the high gain observer as $\hat{\tau}_{m1}$, the total estimated torque is given by:

$$\hat{\tau}_m = \hat{\tau}_{m1} + \hat{\tau}_{m2} \tag{3.61}$$

Therefore, the total estimated torque consists of the dc torque, the first, second, sixth and twelfth harmonic torque ripples that are due to the combined effect of current measurement error and non-ideal back-emf waveform.

3.6 Conclusion

In this chapter, the applications of LVSC and FILC on the PMSM for pulsating torque minimization are presented. Applications of both schemes in this area are proper because the torque pulsations are inherently periodic in nature; hence, these pulsations can be readily compensated by the periodic learning method. In

addition, both controllers are simple to implement, utilize only a small amount of computational overhead and do not need any modification to the existing drive scheme.

Two different control schemes are proposed for the PMSM, one of which is designed to compensate pulsating torque directly by using either LVSC or FILC algorithm, while the other employs the speed controller for speed ripple compensation by using either LVSC or FILC method.

The first scheme employs a torque control without an outer loop speed control. Input to the system is the reference torque command τ_m^* while the instantaneous motor torque signal is either estimated using the torque estimator $\hat{\tau}_m$ or measured from a high-bandwidth output torque transducer τ_m. The proposed controller, i.e. LVSC or FILC torque controller compares the error between τ_m^* and $\hat{\tau}_m/\tau_m$, and computes the reference compensation current i_{qs-2}^* such that convergence of $\hat{\tau}_m/\tau_m$ to τ_m^* to a certain extent is guaranteed as learning progresses.

In the second scheme, the LVSC or FILC performs speed control with the objective of minimizing speed ripples that originate from the torque pulsations. In this scheme, the proposed speed controller is applied in addition to the PI speed controller. The conventional PI speed controller is incapable of fully suppressing the speed ripples. Therefore, the presented speed controller is employed to fully minimize those speed ripples by generating the additional current reference i_{qs-2}^*. Unlike the previous scheme, this scheme does not control the torque—the controller attempts to minimize the speed ripples by controlling the speed. Therefore, the on-line torque estimator is not required since instantaneous torque control is not performed in this scheme.

The next chapter proceeds to verify the effectiveness of the proposed LVSC and FILC schemes through computer simulation studies.

Chapter 4

Simulation Results

4.1 Introduction

To investigate the performances of the proposed LVSC and FILC pulsating torque minimization schemes as well as the high gain torque estimator as described in Chapter 3, simulation studies were carried out using MATLAB software package. The field-oriented controller for the PMSM drive and plant model of a 3-phase, surface-mounted PMSM were programmed using MATLAB programming codes. Torque ripples due to current offset and scaling errors, and harmonics in the flux linkage were also included in the simulation model of the PMSM drive. The model of the PWM inverter operation was omitted in the simulation studies. This omission is justifiable because the actual PWM carrier frequency in the PMSM drive system is higher than 5 kHz, and the simulation results that are obtained by using linear drive voltages are almost identical to those obtained by using the PWM drive voltages [95].

Simulation studies for the drive systems employing the two proposed LVSC schemes as well as two FILC schemes, and the high gain torque estimator were performed, and their steady-state torque (or speed) responses are compared to those with conventional PMSM drive control schemes. Specifically:

1. The performance of the torque controller with the proposed LVSC pulsating torque compensation scheme is compared with that of the conventional feed-

forward scheme (with sinusoidal currents).

2. The performance of the closed-loop PI speed controller with the proposed LVSC speed ripple compensation scheme is compared with that of the conventional closed-loop PI speed control scheme.

3. The performance of the torque controller with the proposed FILC pulsating torque compensation scheme is compared with that of the basic ILC torque ripple compensation scheme.

4. The performance of the closed-loop PI speed controller with the proposed FILC speed ripple compensation scheme is compared with that of the basic ILC speed ripple compensation scheme.

5. The performance of the high gain torque estimator is evaluated by comparing it with the actual instantaneous torque signals obtained from the PMSM dynamic model.

The performance criterion to evaluate the effectiveness of the proposed schemes for torque and speed ripple minimization are the torque ripple factor (TRF) and speed ripple factor (SRF), respectively. TRF is defined as the ratio of the peak-to-peak torque ripple to the rated torque, while SRF is defined as the ratio of the peak-to-peak speed ripple to the rated speed:

$$TRF = \frac{\tau_{pk-pk}}{\tau_{rated}} \times 100\% \tag{4.1}$$

$$SRF = \frac{\omega_{pk-pk}}{\omega_{rated}} \times 100\% \tag{4.2}$$

where τ_{pk-pk} and $\tau_{rated} = 7.8$ Nm are the peak-to-peak torque ripple and rated torque, respectively, while ω_{pk-pk} and $\omega_{rated} = 2000$ rpm are the peak-to-peak speed ripple and rated speed, respectively.

As the torque (or speed) ripples in PMSM affect the drive performance only in steady-state operation, the issue of torque (or speed) ripple minimization is cor-

respondingly addressed only for steady-state operations. Therefore, the TRF and SRF are determined only when the PMSM drive is operating in steady-state. Here 'steady-state' is defined as a condition, under which some specified characteristic, such as a value, rate, periodicity, or amplitude, exhibits only negligible change over an arbitrarily long period.

Section 4.2 presents the simulation results of two LVSC schemes, two FILC schemes, and the high gain torque estimator. Finally, Section 4.3 concludes this chapter.

4.2 Simulation Results

4.2.1 LVSC pulsating torque compensation scheme

The complete PMSM drive scheme with the proposed LVSC torque controller described in Subsection 3.3.2.1 is shown in Fig. 4.1. Note that the high gain torque estimator is not used in this evaluation and the instantaneous torque signal is obtained from the PMSM dynamic model directly, since the performance of the torque estimator is evaluated in a separate subsection. When the LVSC torque controller is not functional, the control scheme is essentially a feed-forward scheme with sinusoidal current excitation. However, when the LVSC torque controller is activated, it provides the additional compensation current i^*_{qs-2} for torque ripple minimization. In the simulation studies, the PMSM drive employing the two schemes (current-regulated PWM with sinusoidal current reference (CRPWM) and the proposed LVSC scheme) are operated under different conditions: at a speed of 0.025 p.u.(50 rpm) with load torques ranging from 0.2 p.u.(1.56 Nm) to 0.8 p.u.(6.24 Nm). The TRF of the two schemes are then compared to study the effectiveness of the proposed LVSC scheme in accomplishing pulsating torque minimization.

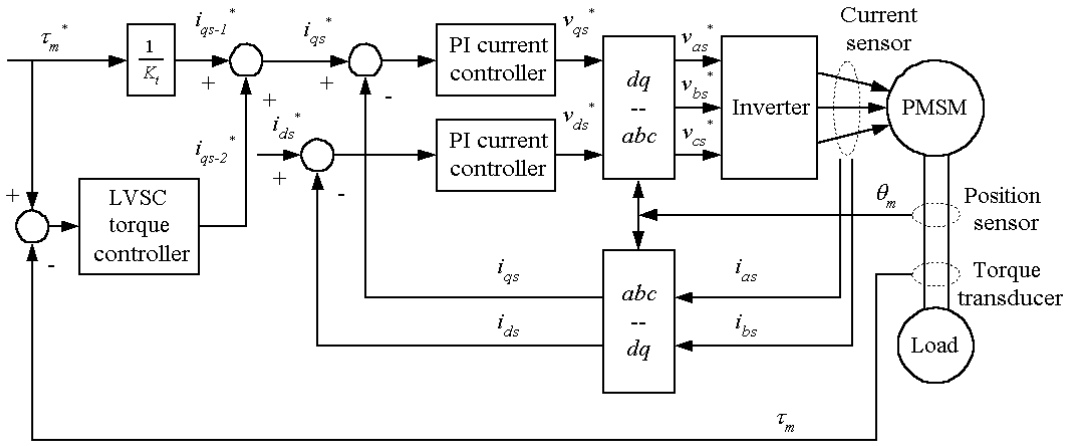

Figure 4.1: PMSM drive scheme employing the proposed LVSC torque control.

In the simulation studies, the PMSM is allowed to accelerate by applying the reference torque signal, τ_m^*, which is greater than the load torque, τ_L, until the motor reaches the desired speed, then τ_m^* is reduced to τ_L so that the motor operates at a constant speed in steady state.

Fig. 4.2 (a) shows the steady-state torque response of the conventional CRPWM drive scheme when the operating conditions are: speed 0.025 p.u.(50 rpm) and load torque 0.2 p.u.(1.56 Nm). The corresponding TRF is 7.60%. The frequency spectrum in Fig. 4.2 (b) shows the presence of the 1^{st}, 2^{nd}, 6^{th} and 12^{th} harmonics in the torque response. Fig. 4.3 (a) shows the steady-state torque response of the proposed LVSC torque control scheme under the same operating conditions as in Fig. 4.2. With the LVSC torque ripple compensation scheme being active, the corresponding TRF is improved from 7.60% to 0.19%, in other words, the torque ripples are almost removed completely as can be seen from Fig. 4.3.

To verify the effectiveness of the proposed LVSC scheme under heavy loads, the PMSM is operated under a load of 0.8 p.u.(6.24 Nm) with the operating speed around 0.025 p.u.(50 rpm). Fig. 4.4 shows the steady-state torque response of the CRPWM scheme. The corresponding TRF is 9.33%. Similarly, Fig. 4.5 shows the steady-state torque response of the proposed LVSC torque control scheme. With

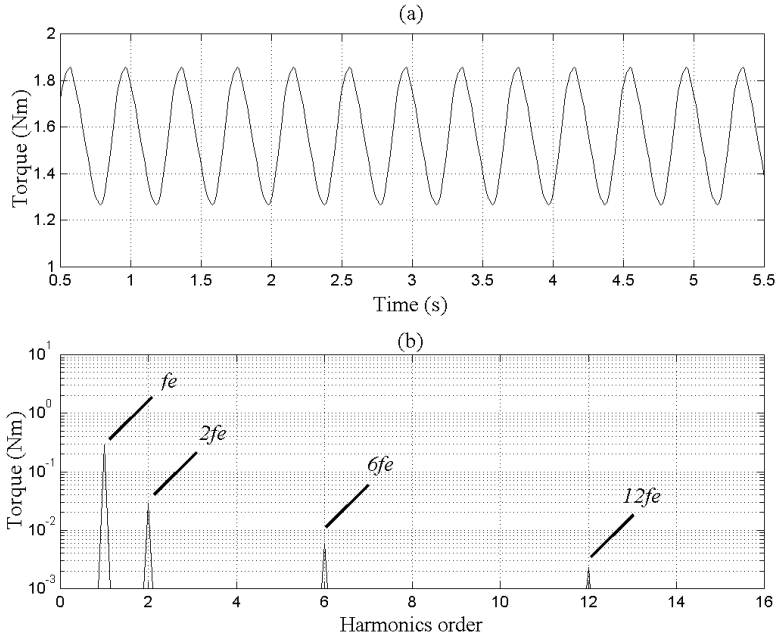

Figure 4.2: Sinusoidal current control scheme: (a) steady-state torque response (TRF=7.60%), and (b) the corresponding frequency spectrum.

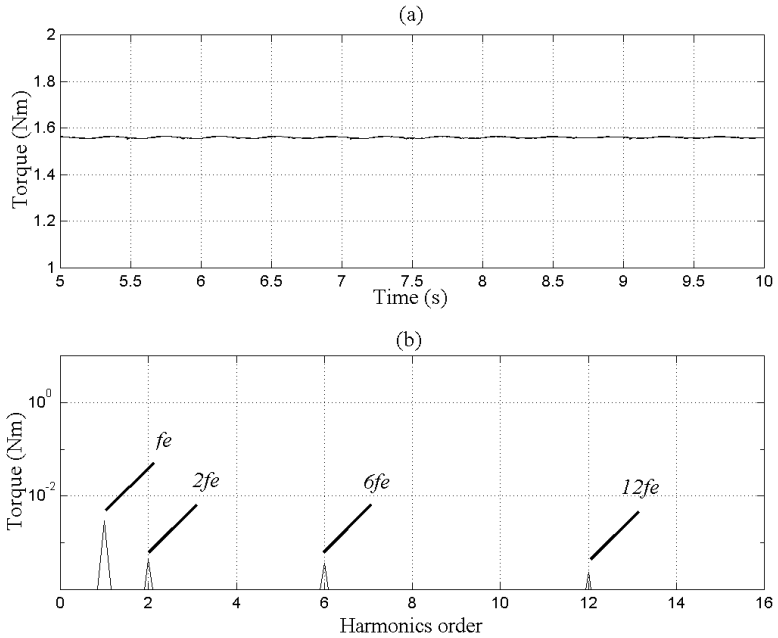

Figure 4.3: Proposed LVSC torque control scheme: (a) steady-state torque response (TRF=0.19%), and (b) the corresponding frequency spectrum.

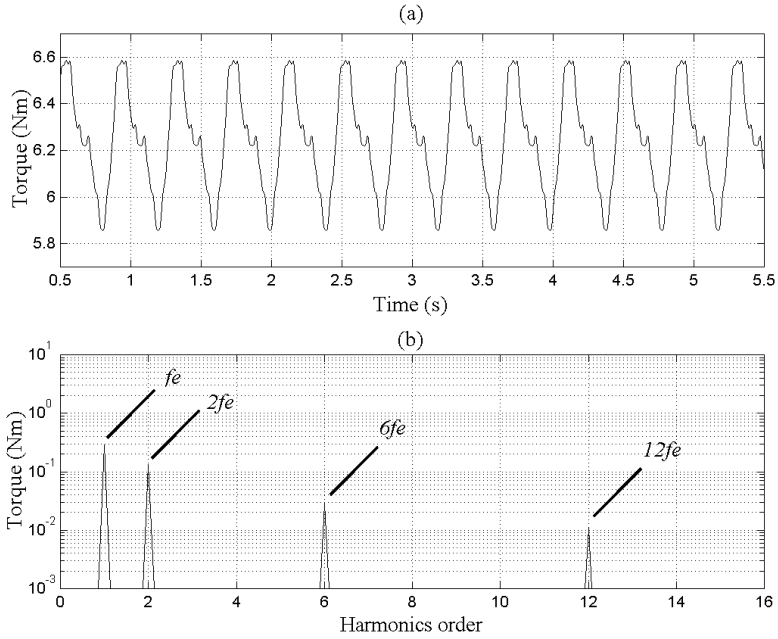

Figure 4.4: Sinusoidal current control scheme: (a) steady-state torque response (TRF=9.33%), and (b) the corresponding frequency spectrum.

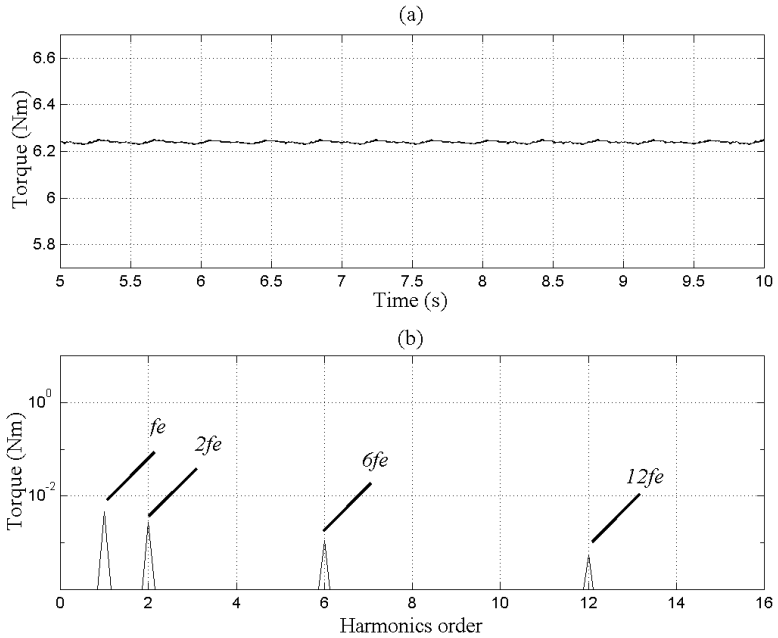

Figure 4.5: Proposed LVSC torque control scheme: (a) steady-state torque response (TRF=0.29%), and (b) the corresponding frequency spectrum.

the torque ripple compensation provided by the LVSC scheme, the corresponding TRF is significantly improved to 0.29%. Table 4.1 shows the numerical results of specific harmonic torque components with and without the LVSC torque ripple compensation scheme. From these data, it can be found that all those harmonics present in pulsating torque have been suppressed by a factor of more than 9.

Table 4.1: Torque harmonics with or without LVSC torque control.

Loading conditions	Harmonics order	1^{st}	2^{nd}	6^{th}	12^{th}
Light load	without LVSC (Nm)	2.8e-1	2.7e-2	6.0e-3	2.2e-3
(0.2 p.u.)	with LVSC (Nm)	2.9e-3	4.4e-4	3.7e-4	2.4e-4
Heavy load	without LVSC (Nm)	2.8e-1	1.2e-1	3.0e-2	1.0e-2
(0.8 p.u.)	with LVSC (Nm)	4.4e-3	2.6e-3	1.1e-3	5.2e-4

From the motor torque equation in (2.45), it is known that the motor torque is directly proportional to the amplitude of the stator current. However, as expressed in (2.56) and (2.57), the magnitude of the 6^{th} and 12^{th} harmonic ripples in the torque (those are due to the harmonics in the flux linkage) are directly proportional to the amplitude of the stator current. Therefore, with higher loading it is expected that these torque ripples (6^{th} and 12^{th} harmonic components) increase significantly while the magnitude of the 1^{st} torque ripple component remains constant. Comparing the torque responses of the CRPWM scheme shown in Fig. 4.2 with Fig. 4.4, it can be seen that the 6^{th} and 12^{th} harmonic torque ripples become more dominant as the load torque is increased (from 0.2 p.u. to 0.8 p.u.), thus complying with theory.

The steady-state phase currents of the CRPWM and proposed LVSC schemes are shown in Figs. 4.6 and 4.7, respectively. Comparing Fig. 4.6(a) and 4.7(a), it can be seen that the LVSC torque controller compensates the torque ripples by injecting additional harmonics to the purely sinusoidal phase currents. The frequency spectra of these phase currents in Fig. 4.6(b) and 4.7(b) confirm that

the LVSC modifies the sinusoidal phase currents by injecting the 5^{th}, 7^{th}, 11^{th} and 13^{th} harmonic components in the phase currents. However, after these harmonic components has been injected, the rms value of phase current has been reduced from 0.652 A to 0.646 A. Although the decrease is slight, it still degrades the operating performance of the PMSM.

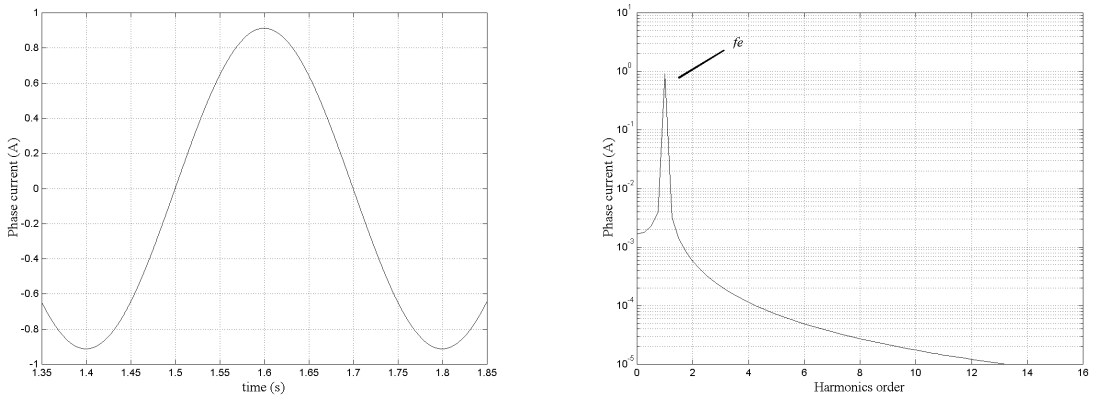

(a) Steady-state phase current for one electrical period

(b) The corresponding frequency spectrum (f_e=2.5 Hz)

Figure 4.6: Sinusoidal current control scheme

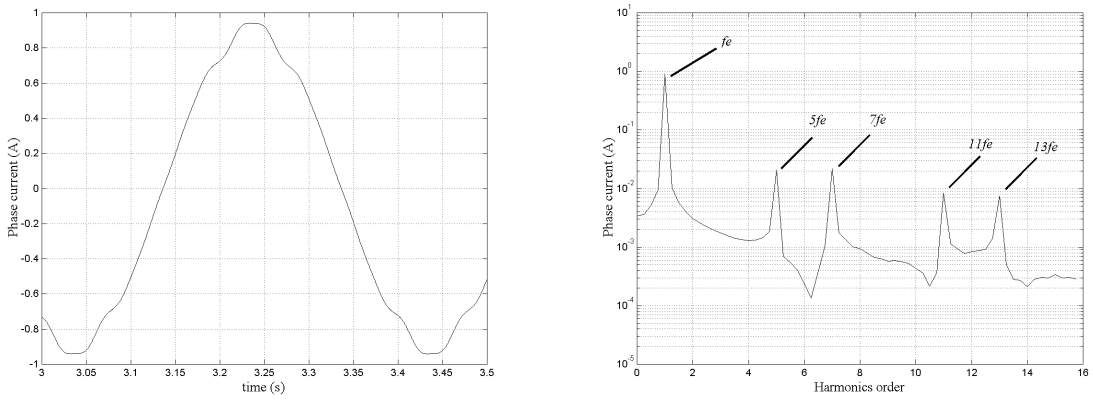

(a) Steady-state phase current for one electrical period

(b) The corresponding frequency spectrum (f_e=2.5 Hz)

Figure 4.7: Proposed LVSC torque control scheme

The following subsection presents the simulation results of the proposed LVSC

speed ripple compensation scheme, whose performance is compared with that of the closed-loop PI speed controller.

4.2.2 LVSC speed ripple compensation scheme

The closed-loop PI speed control with LVSC speed ripple compensation scheme described in Subsection 3.3.2.2 is shown in Fig. 4.8. In this scheme, the LVSC speed controller is applied in parallel with a PI speed controller. Without the LVSC speed controller, the control scheme is essentially a conventional PI speed controller. However, when the LVSC speed controller is activated, it provides an additional q-axis reference compensation current i^*_{qs-2} for speed ripple minimization. To a limited extent, the PI speed controller compensates the speed ripples. However, using the PI speed controller alone is not adequate to completely suppress the speed ripples. This is because the PI controller cannot fully reject the non-linear torque disturbances. Furthermore, the PI speed controller has a limited bandwidth that makes it incapable of compensating for higher order harmonic speed ripples. Therefore, the additional LVSC speed controller is required to further minimize these speed ripples.

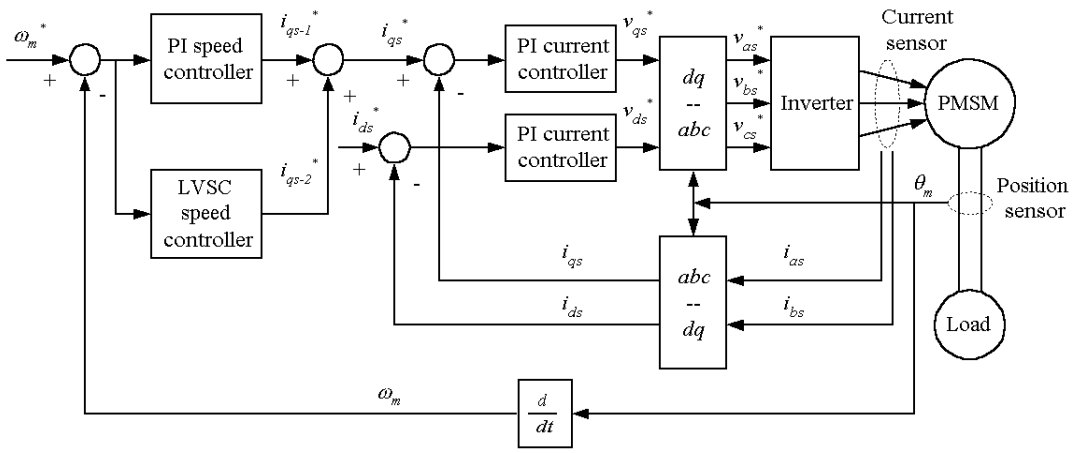

Figure 4.8: PMSM drive scheme employing the proposed LVSC speed control.

In this simulation study, the PMSM drive employing the two schemes (PI

speed control with and without the proposed LVSC speed control scheme) are operated at a speed of 0.025 p.u.(50 rpm) under different load torques ranging from 0.2 p.u.(1.56 Nm) to 0.8 p.u.(6.24 Nm). At low operating speeds, the effect of the torque pulsations on the motor speed becomes significant. This is because at low motor speeds, the torque pulsations are correspondingly at low frequencies, and are not filtered off by the system inertia; hence, they are reflected back in the motor speed as speed ripples. The SRF of the two schemes are evaluated by using the definition of the SRF in (4.2). They are then compared to study the effectiveness of the proposed LVSC scheme on speed ripple minimization.

With the PI speed controller in the outer loop, the desired operating speed of the PMSM is determined by the reference speed signal input by the user, ω_m^*, to the PI speed controller. This is unlike the open-loop case in torque controller where, in the absence of any speed controller, the motor is allowed to accelerate by manually setting the reference torque signal, τ_m^*, to be greater than the load torque, τ_L, until the motor reaches the desired speed.

Fig. 4.9 (a) shows the steady-state speed response of the conventional closed-loop PI speed control scheme without the proposed LVSC speed controller (ω_m^*=50 rpm, τ_m^*=1.56 Nm). The corresponding SRF is 0.20%. The frequency spectrum in Fig. 4.9 (b) indicates the presence of significant fundamental harmonic component in the speed ripples. Fig. 4.10 (a) shows the steady-state speed response of the PMSM drive with the proposed LVSC speed control scheme under the same working conditions as in Fig. 4.9. With LVSC speed ripple compensation being activated, the SRF is greatly improved to 0.01%. From the frequency spectra shown in Figs. 4.9 (b) and 4.10 (b), it is evident that the proposed LVSC scheme reduces the all harmonic speed ripples by at least one order of magnitude. This demonstrates the effectiveness of the LVSC scheme in providing additional compensation to further minimize the speed ripples.

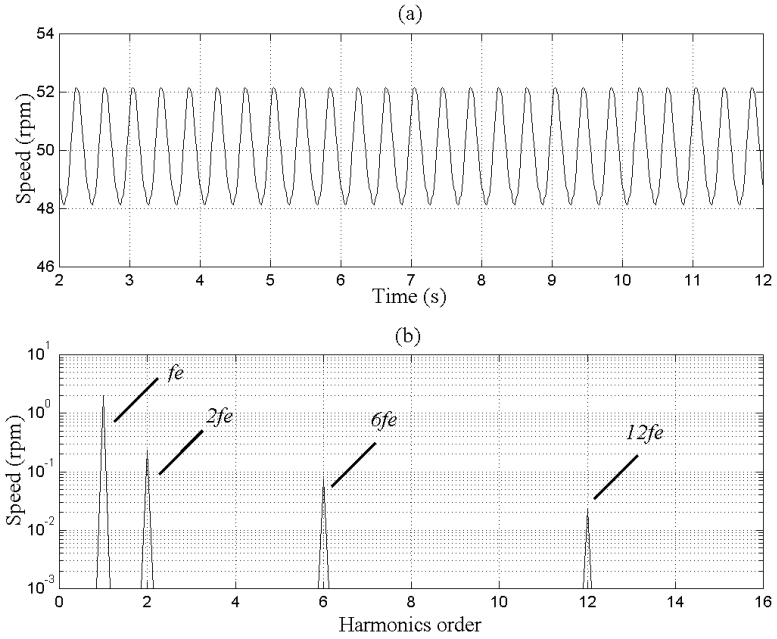

Figure 4.9: Conventional PI speed control scheme: (a) steady-state speed response (SRF=0.2%), and (b) the corresponding frequency spectrum.

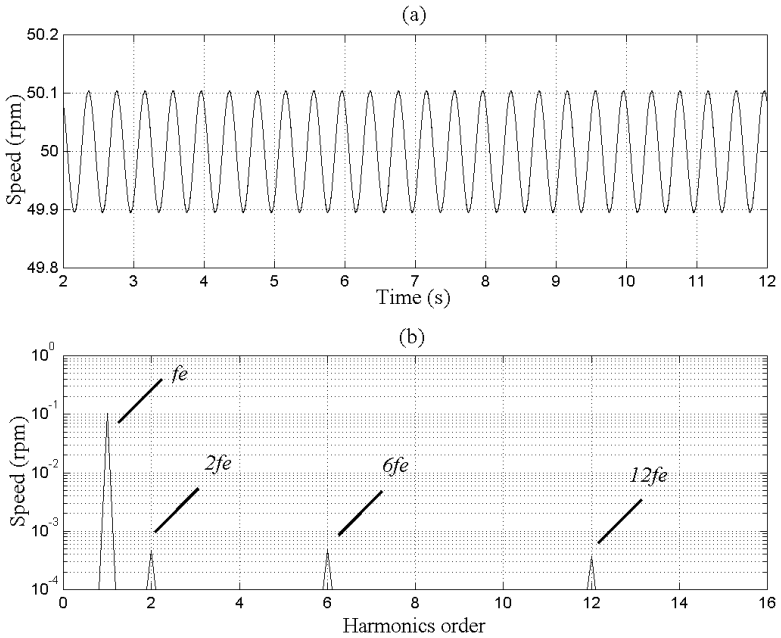

Figure 4.10: Conventional PI speed control scheme with LVSC speed control: (a) steady-state speed response (SRF=0.01%), and (b) the corresponding frequency spectrum.

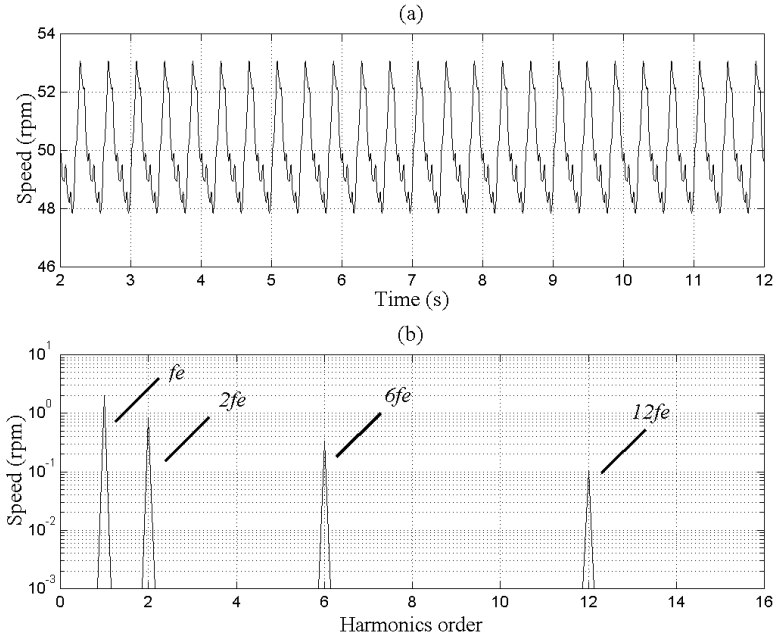

Figure 4.11: Conventional PI speed control scheme: (a) steady-state speed response (SRF=0.26%), and (b) the corresponding frequency spectrum.

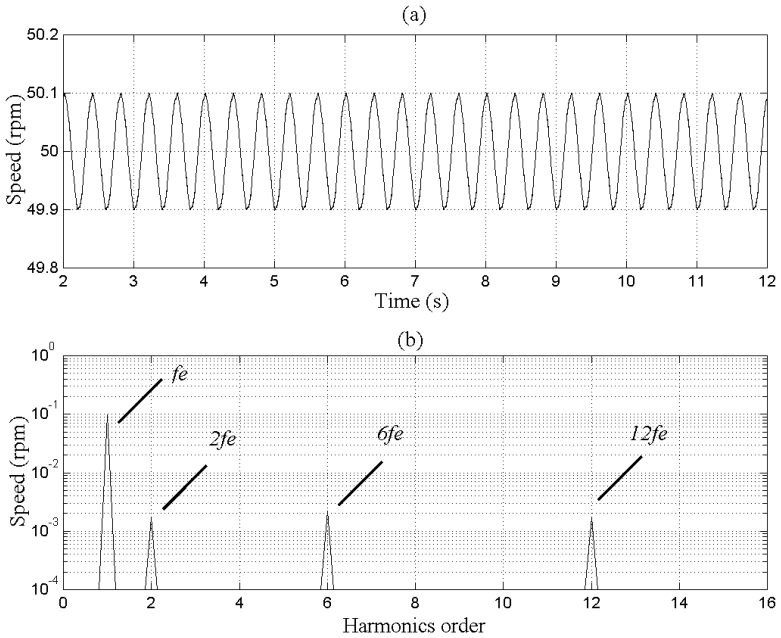

Figure 4.12: Conventional PI speed control scheme with LVSC speed control: (a) steady-state speed response (SRF=0.01%), and (b) the corresponding frequency spectrum.

As described in Subsection 4.2.1, an undesirable consequence of increasing the load torque is the increase in the 6^{th} and 12^{th} harmonic torque ripples. Therefore, with increased loading to the PMSM, the corresponding speed ripples (that are due to the 6^{th} and 12^{th} harmonic torque ripples) are expected to increase. In this case, the influence of increasing the load torque on the effectiveness of the proposed LVSC scheme is studied. Operate the PMSM at a speed of 0.025 p.u.(50 rpm) and a load torque of 0.8 p.u.(6.24 Nm) applied to the motor. Fig. 4.11 shows the steady-state speed response of the PI speed control scheme without LVSC speed ripple compensation. The corresponding SRF is 0.26%. From the figure, the 6^{th} and 12^{th} harmonic speed ripples are dominant unlike in Fig. 4.9, where a lower load torque is applied to the PMSM. With LVSC speed ripple compensation being activated, the SRF is significantly reduced to 0.01%. The steady-state speed response of the drive scheme with LVSC compensation is shown in Fig. 4.12 and Table 4.2 shows the numerical results of specific harmonic speed components with and without the LVSC compensation scheme.

Table 4.2: Speed harmonics with or without LVSC speed control.

Loading conditions	Harmonics order	1^{st}	2^{nd}	6^{th}	12^{th}
Light load (0.2 p.u.)	without LVSC (rpm)	2.0	2.3e-1	7.4e-2	2.3e-2
	with LVSC (rpm)	1.0e-1	4.7e-4	4.9e-4	3.7e-4
Heavy load (0.8 p.u.)	without LVSC (rpm)	2.0	8.4e-1	3.4e-1	1.1e-1
	with LVSC (rpm)	9.8e-2	1.8e-3	2.2e-3	1.7e-3

The following subsections present the simulation results of the proposed FILC compensation schemes.

4.2.3 FILC pulsating torque compensation scheme

The complete PMSM drive scheme with the proposed FILC torque controller has the same structure as that of the LVSC scheme as described in Subsection 4.2.1,

and hence readers are suggested to see Fig. 4.1 for reference. When the FILC torque controller is not functional, the control scheme is essentially a feed-forward scheme with sinusoidal current excitation. When the FILC torque controller is activated, it provides the additional compensation current i^*_{qs-2} for torque ripple minimization. In the simulation studies, the PMSM drive employing the two schemes (the basic ILC and the proposed FILC schemes) are operated under different conditions: at a speed of 0.025 p.u.(50 rpm) with load torques ranging from 0.2 p.u.(1.56 Nm) to 0.8 p.u.(6.24 Nm). The TRF of the two schemes are then compared to study the effectiveness of the proposed FILC scheme on accomplishing pulsating torque minimization.

Fig. 4.13 (a) shows the steady-state torque response of the basic ILC torque control scheme when the operating conditions are: speed equal to 0.025 p.u.(50 rpm) and load torque equal to 0.2 p.u.(1.56 Nm). The corresponding TRF is 0.49%. The frequency spectrum in Fig. 4.13 (b) shows the presence of the 1^{st}, 2^{nd}, 6^{th} and 12^{th} harmonics in the torque response. Fig. 4.14 (a) shows the steady-state torque response of the proposed FILC torque control scheme under the same operating conditions. With the frequency-domain learning compensation, the corresponding TRF is improved from 0.49% to 0.22%, in other words, the torque ripples are further reduced by a factor of 2.

To verify the effectiveness of the proposed FILC scheme under a heavy load, the PMSM is operated under a load of 0.8 p.u.(6.24 Nm) at an operating speed of 0.025 p.u.(50 rpm). Fig. 4.15 shows the steady-state torque response of the basic ILC scheme. The corresponding TRF is 1.30%. Similarly, Fig. 4.16 shows the steady-state torque response of the proposed FILC torque control scheme. With the compensation currents provided by the FILC scheme, the corresponding TRF is further improved to 0.90%. Table 4.3 shows the numerical results of specific torque harmonics. From these data, it can be found that frequency-domain learning

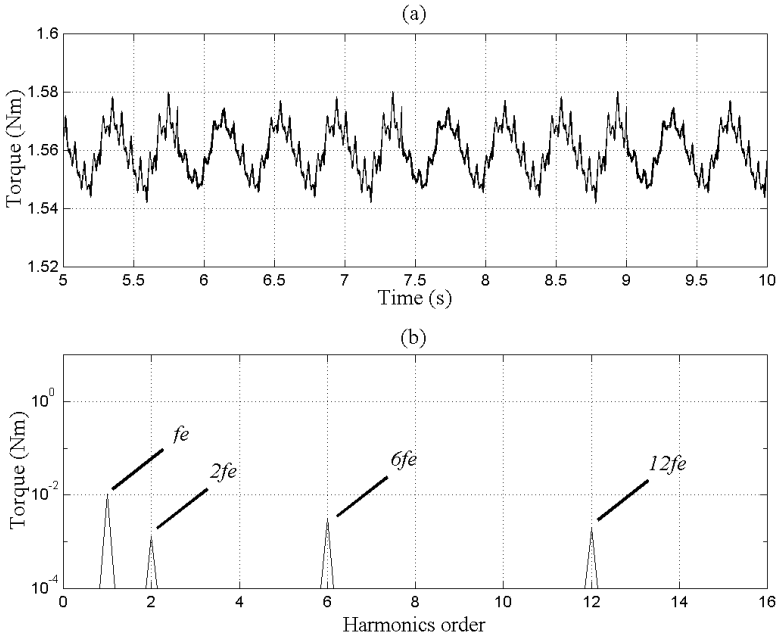

Figure 4.13: The basic ILC torque control scheme: (a) steady-state torque response (TRF=0.49%), and (b) the corresponding frequency spectrum.

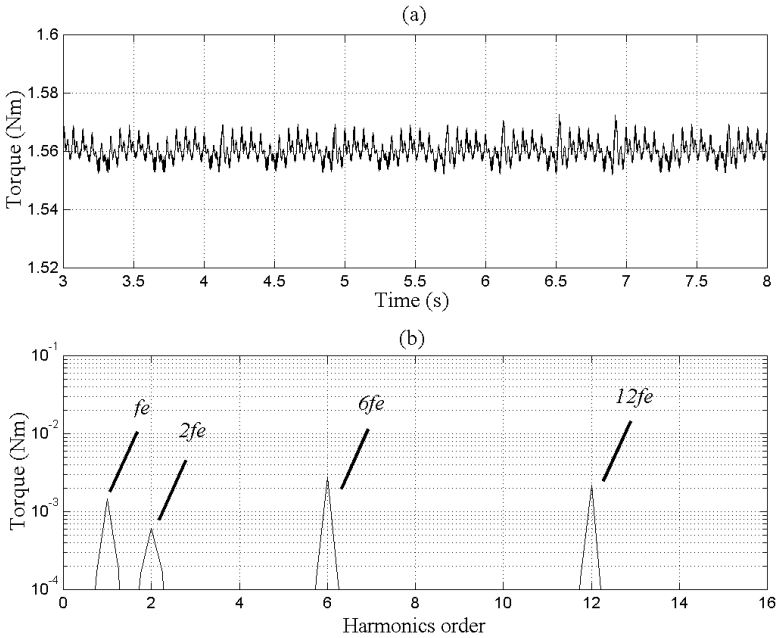

Figure 4.14: The proposed FILC torque control scheme: (a) steady-state torque response (TRF=0.22%), and (b) the corresponding frequency spectrum.

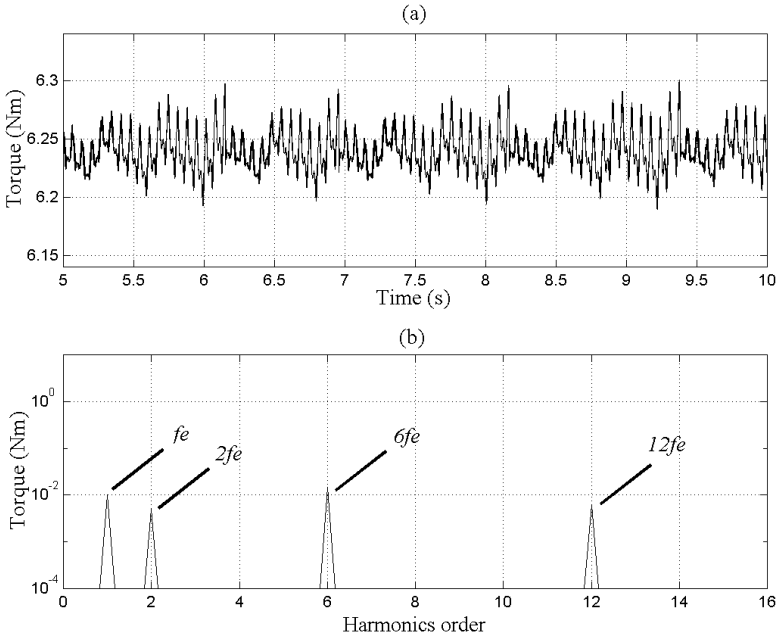

Figure 4.15: The basic ILC torque control scheme: (a) steady-state torque response (TRF=1.30%), and (b) the corresponding frequency spectrum.

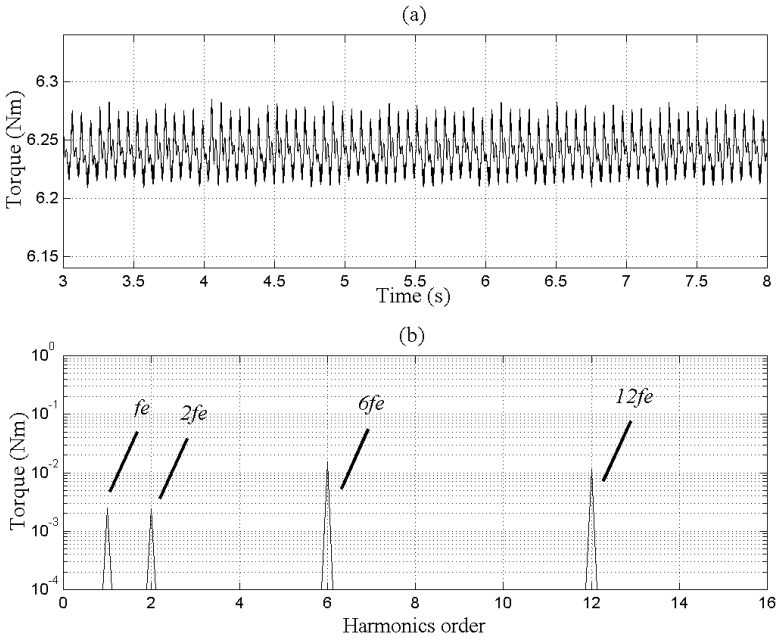

Figure 4.16: The proposed FILC torque control scheme: (a) steady-state torque response (TRF=0.90%), and (b) the corresponding frequency spectrum.

method can further suppress the 1^{st} and 2^{nd} harmonic components, but do not have much effect on the 6^{th} and 12^{th} harmonics. This is because the 6^{th} and 12^{th} harmonic components are already reduced to small values by applying the basic ILC compensation scheme, and further reduction is difficult to achieve.

Table 4.3: Torque Harmonics with or without ILC/FILC torque control.

Loading conditions	Harmonics order	1^{st}	2^{nd}	6^{th}	12^{th}
Light load	with ILC (Nm)	1.1e-2	1.3e-3	3.2e-3	1.9e-3
(0.2 p.u.)	with FILC (Nm)	1.5e-3	6.1e-4	2.8e-3	2.2e-3
Heavy load	with ILC (Nm)	1.0e-2	5.0e-3	1.5e-2	6.3e-3
(0.8 p.u.)	with FILC (Nm)	2.5e-3	2.4e-3	1.5e-2	1.1e-2

4.2.4 FILC speed ripple compensation scheme

Similarly, the closed-loop PI speed control with the FILC speed ripple compensation scheme has the same structure as that of LVSC scheme, and readers are suggested to refer to Fig. 4.8 for details. In this scheme, the FILC speed controller is applied in parallel with a PI speed controller. When the FILC speed controller is activated, it provides additional compensation current i^*_{qs-2} for speed ripple minimization. Although the basic ILC speed controller can reduce speed ripples to a great extent, however, the presence of forgetting factor limits this reduction. Therefore, the FILC speed controller implemented by means of Fourier series expansion is proposed to eliminate the forgetting factor, and hence can further minimize the speed ripples. In this simulation study, the PMSM drive employing the two schemes (PI speed control with either the basic ILC or the proposed FILC speed control scheme) are operated at a speed of 0.025 p.u.(50 rpm) under different load torques ranging from 0.2 p.u.(1.56 Nm) to 0.8 p.u.(6.24 Nm). The SRF of the two schemes are then compared to study the effectiveness of the proposed FILC scheme on speed

ripple minimization.

Fig. 4.17 (a) shows the steady-state speed response of the conventional closed-loop PI speed control scheme with the basic ILC speed controller (ω_m^*=50 rpm, τ_m^*=1.56 Nm). The corresponding SRF is 0.0096%. The frequency spectrum in Fig. 4.17 (b) indicates the reduction of those harmonic components in the speed ripples, compared with Fig. 4.9 (b). Fig. 4.18 (a) shows the steady-state speed response of the PMSM drive with the proposed FILC speed control scheme under the same working conditions as in Fig. 4.17. With FILC speed ripple compensation, the SRF is further improved to 0.002%. From the frequency spectrum in Figs. 4.17 (b) and 4.18 (b), it is evident that the proposed FILC scheme reduces the 1^{st} harmonics by a factor of 5, compared with the result of ILC speed control scheme. This demonstrates the effectiveness of the FILC scheme in providing additional compensation to further minimize the speed ripples.

In this case, the influence of increasing the load torque on the effectiveness of the proposed FILC scheme is studied. Operating the PMSM at a speed of 0.025 p.u.(50 rpm), a load torque of 0.8 p.u.(6.24 Nm) is applied to the motor. Fig. 4.19 shows the steady-state speed response of the PI speed control scheme with ILC speed ripple compensation. The corresponding SRF is improved to 0.012%. In the figure, the 6^{th} and 12^{th} harmonic speed ripples are increased by a factor of 4, compared with those in Fig. 4.17, where a lower load torque is applied to the PMSM. With FILC speed ripple compensation, the SRF is further reduced to 0.004%. The speed response of the drive scheme with FILC compensation is shown in Fig. 4.20. Table 4.4 shows the numerical results of specific speed harmonics of both compensation schemes.

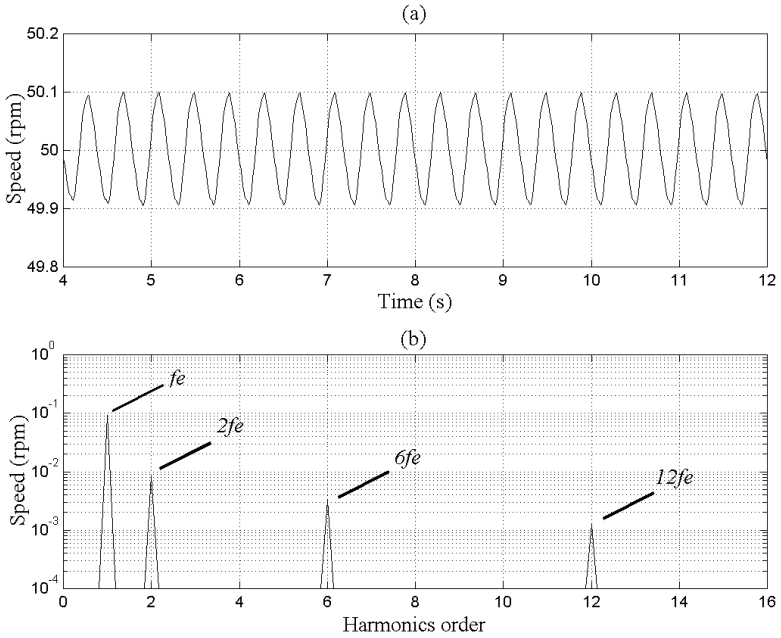

Figure 4.17: Conventional PI speed control scheme with ILC speed control: (a) steady-state speed response (SRF=0.0096%), and (b) the corresponding frequency spectrum.

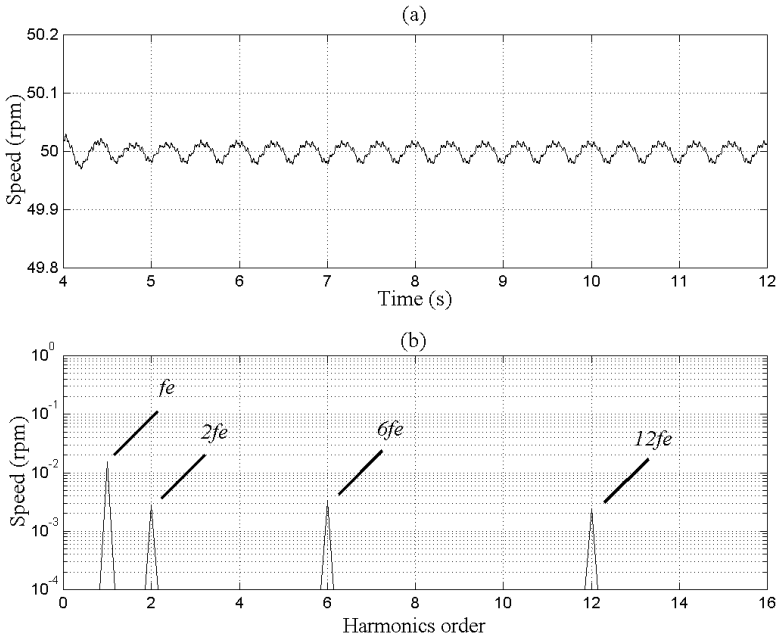

Figure 4.18: Conventional PI speed control scheme with FILC speed control: (a) steady-state speed response (SRF=0.002%), and (b) the corresponding frequency spectrum.

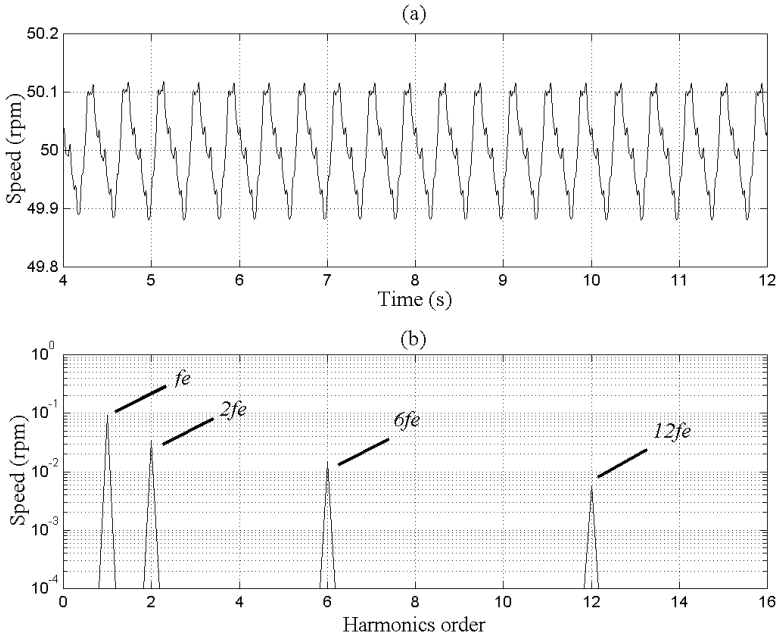

Figure 4.19: Conventional PI speed control scheme with ILC speed control: (a) steady-state speed response (SRF=0.012%), and (b) the corresponding frequency spectrum.

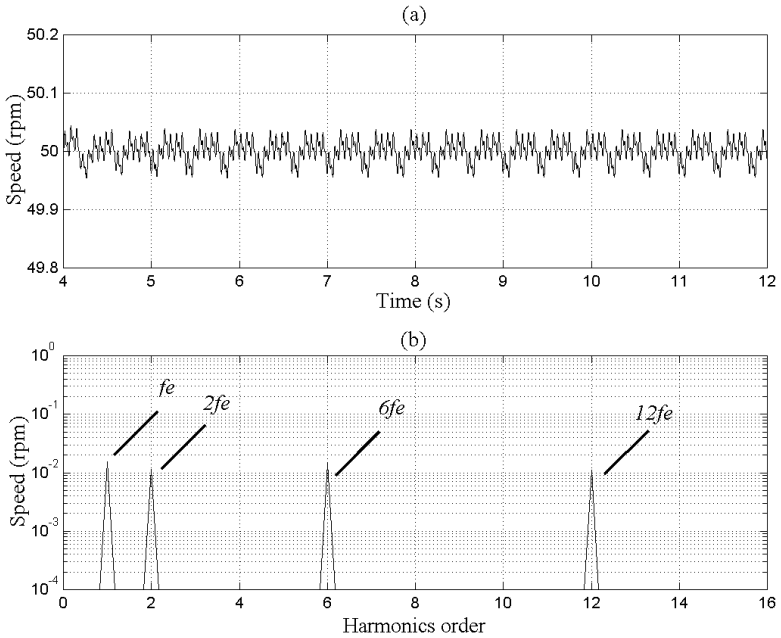

Figure 4.20: Conventional PI speed control scheme with FILC speed control: (a) steady-state speed response (SRF=0.004%), and (b) the corresponding frequency spectrum.

Table 4.4: Speed harmonics with or without ILC/FILC speed control.

Loading conditions	Harmonics order	1^{st}	2^{nd}	6^{th}	12^{th}
Light load	with ILC (rpm)	9.2e-2	8.5e-3	3.2e-3	1.3e-3
(0.2 p.u.)	with FILC (rpm)	1.6e-2	2.8e-3	3.2e-3	2.4e-3
Heavy load	with ILC (rpm)	9.2e-2	3.4e-2	1.5e-2	5.8e-3
(0.8 p.u.)	with FILC (rpm)	4.1e-1	6.2e-4	8.4e-4	4.6e-4

4.2.5 High gain torque estimator

In order to verify the effectiveness of the proposed high gain torque estimator as described in Section 3.5, the simulation investigation were carried out. However, the performance of the proposed high gain torque estimator is not fixed. Instead, it is affected by different values of parameter τ, i.e. the time constant of the low pass filter in the observer. To find out the most ideal value of parameter τ, various values of the parameter were tested and corresponding estimated torque waveforms are compared with the actual torque signals.

The basic function of the low pass filter used in the torque estimator is eliminating high frequency noise meanwhile leaving the complete information of pulsating torque harmonics, which can be used as the feedback signal to the controller. Thus the upper bound of parameter τ can be determined according to the consideration of allowing the complete information of pulsating torque harmonics to pass. In the simulation study, the motor is assumed to operate around 50 rpm, which means the synchronous frequency is 2.5 Hz ($f_e = P_p\omega_m/(2\pi) = 3\times 50/60 = 2.5$Hz). To consider the 12^{th} harmonics, the maximum value of parameter τ can be determined as:

$$\tau \leq \frac{1}{2\pi \times 12 \times f_e} = 5.31e-3 \tag{4.3}$$

Fig. 4.21 (a) shows the actual and estimated torque waveforms when parameter τ is equal to $5.31e-3$ (ω_m=50 rpm, τ_L=1.56 Nm). Fig. 4.21 (b) illustrates

the torque error between the actual and estimated values. The magnitude of the estimated torque error is within 0.06 Nm. Theoretically, further decreasing of parameter τ can bring more accurate estimation. Thus $\tau = 5.31e-4$ has been tried and the corresponding result is shown in Fig. 4.22. In this case, the error value is greatly reduced and hence the effectiveness of the proposed high gain torque estimator is verified. To investigate how a large value of time constant influences the estimation performance, $\tau = 5.31e-2$ was also tested in Fig. 4.23. It can be found that a comparatively smooth torque waveform is estimated and high frequency harmonics information is lost due to the large time constant of the low pass filter. Hence, a small value of τ is more appropriate than a large one. However, too small time constant also can induce problems, since some low-frequency noise cannot be filtered properly due to the high-bandwidth of the low pass filter in practical application. Thus, a value between 5.0e-4 and 1.0e-3 is fine with our simulation and experimental tasks.

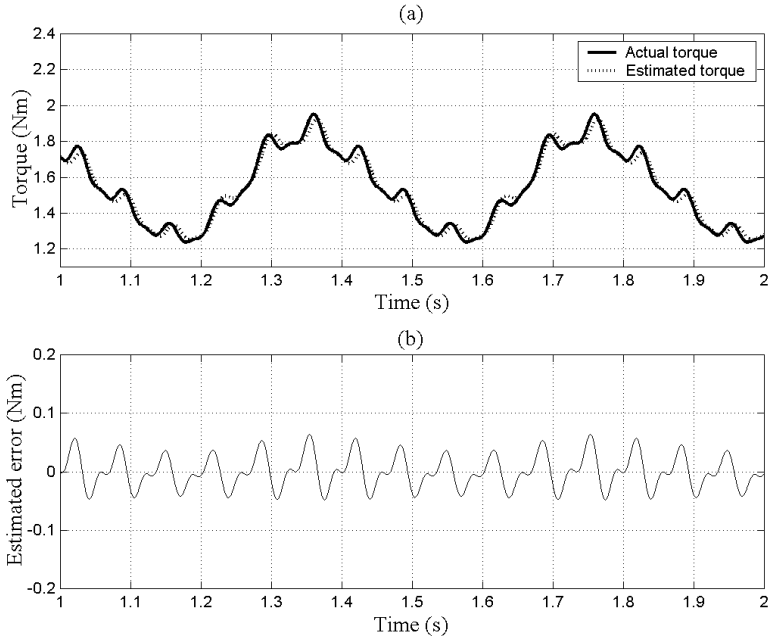

Figure 4.21: (a) Actual and estimated torque waveforms (τ=5.31e-3). (b) Estimated torque error.

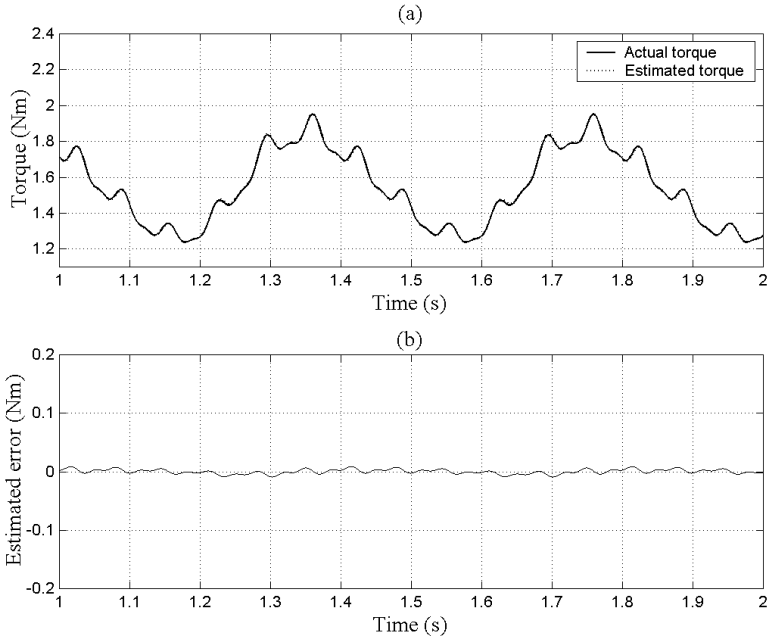

Figure 4.22: (a) Actual and estimated torque waveforms (τ=5.31e-4). (b) Estimated torque error.

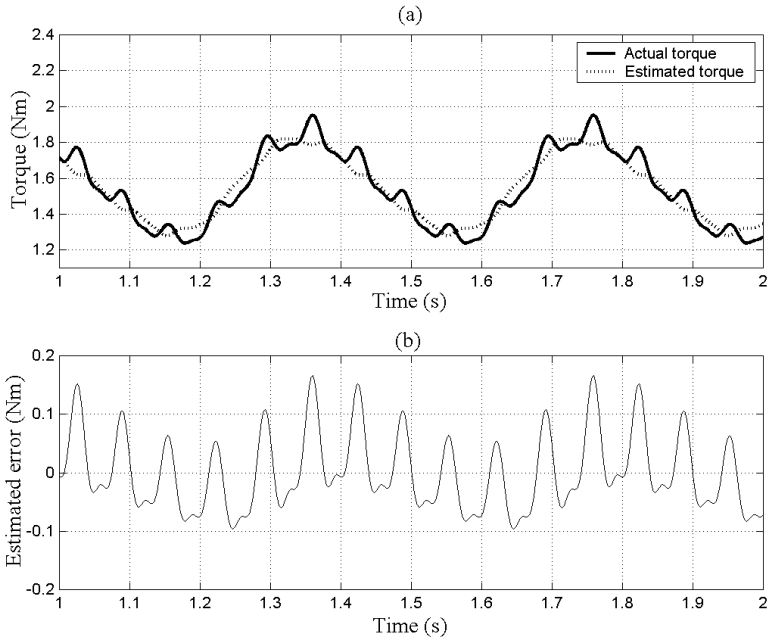

Figure 4.23: (a) Actual and estimated torque waveforms (τ=5.31e-2). (b) Estimated torque error.

4.3 Conclusion

This chapter presents the simulation results showing the effectiveness of the two LVSC and two FILC schemes in achieving torque (or speed) ripple minimization. The simulation studies are carried out for the PMSM drive over a wide range of load torques (0.2 p.u. - 0.8 p.u.) at a low operating speed of 50 rpm (0.025 p.u.). The performances of the conventional PMSM drive schemes, namely, the feed-forward CRPWM scheme, the closed-loop PI speed control scheme, and the basic ILC speed and torque ripple compensation schemes are used to compare with those of the proposed schemes. In the simulation studies, the proposed high gain torque estimator is tested separately in Subsection 4.2.5 to estimate the instantaneous torque feedback signal that is required for the LVSC and FILC torque controllers. The TRF (or SRF) is determined as performance criterion to evaluate the effectiveness of the proposed schemes.

It is shown from the simulation results that the proposed LVSC and the FILC torque controllers, and the LVSC and the FILC speed controllers are effective in minimizing periodic torque and speed ripples, respectively. The learning control iteratively "learns" the optimal current wave-shape that is required to minimize these torque (or speed) ripples cycle-by-cycle using previous "experience" of the error signal between the desired torque (or speed) and the actual motor torque (or speed) feedback signals. The simulation results demonstrate that, under the simulated operating conditions, the proposed LVSC and FILC schemes are able to minimize the torque (or speed) ripples at least by a factor of 10. In addition, the FILC schemes implemented by means of Fourier Series expansion can further reduce torque (or speed) ripples compared with the basic ILC scheme implemented with a forgetting factor. According to the simulation results, the high gain torque estimator is verified effective in estimating the instantaneous torque signals with the parameter chosen properly. Since the satisfactory simulation test results have

been obtained, the next step proceeds to verify the effectiveness of the proposed scheme via experimental studies. The following chapter briefly describes the experimental setup and implementation schemes of the PMSM drive that is used in the experimental studies.

Chapter 5

Hardware and Software Implementation of the DSP-based PMSM Drive System

5.1 Introduction

The pulsating torque minimization schemes employing the proposed control algorithms that were described in previous chapters were implemented on a 1.64 kW surface-mounted PMSM using a 2.2 kW IGBT PWM voltage-source inverter, a digital signal processor (DSP) and an integrated interface platform providing interface between the digital and analog systems. The DSP executes instructions at 60 MHz clock frequency and the drive system can operate at a sampling period of 250 μs for the inner current control loop. The program codes, in which the control algorithm and drive functions are contained, are written in C language.

Section 5.2 presents an overview of the drive implementation. Section 5.3 briefly describes the PMSM drive hardware used in this research work. Section 5.4 provides description of the DSP software environment. In Section 5.5, the control algorithms for the pulsating torque minimization schemes which are implemented using C programming are presented using flow charts. Section 5.6 concludes this chapter.

5.2 Overview of the Drive Implementation

Using the *dSPACE* DSP-DS1102 processor, an experimental setup for implementing speed or torque control of PMSM drives has been built. Fig. 5.1 shows the photograph of the experimental machines, which consist of a PMSM, a torque transducer and a DC generator. Fig. 5.2 shows the configuration for the experimental setup.

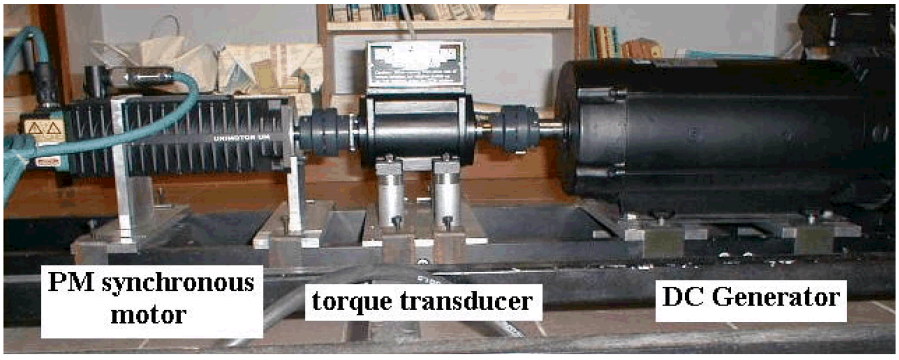

Figure 5.1: Photograph of the PMSM and loading mechanism used in experiments

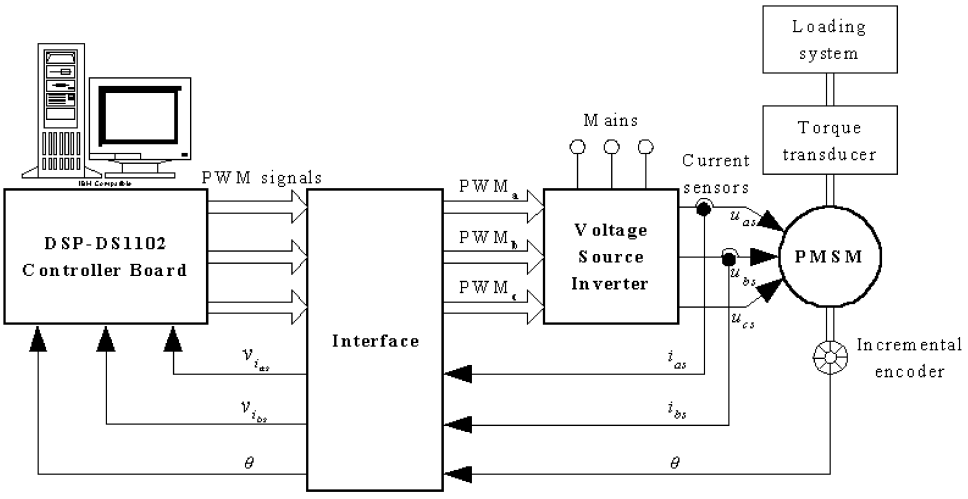

Figure 5.2: Configuration for the PMSM drive experimental setup

As shown in Fig. 5.2, the experimental setup comprises the following:

1. A PC/AT for software programming, debugging and real-time control.

2. A DSP-DS1102 controller board for executing control programs, generating

control signals, performing A/D and D/A conversions, and communicating with the PC/AT.

3. A PWM voltage-source inverter for driving the PMSM.

4. An integrated interface platform for performing logic operations, inverter control, buffering, isolation, protection, etc.

5. A surface-mounted PMSM with built-in incremental encoder for position sensing.

6. Two current sensors for measuring the phase currents in two motor phases.

7. A loading system for providing load torque to the PMSM.

8. A torque transducer for measuring the actual motor torque.

5.3 System Hardware

The system hardware essentially comprises the DS1102 controller board, PMW inverter, PMSM, integrated interface platform, current sensors, loading system and torque transducer. The individual components of the system hardware are described in the following subsections [96].

5.3.1 DS1102 controller board

The *dSPACE* DS1102 controller board is specifically designed for the development of high-speed multi-variable digital controllers and real-time implementations in various fields such as motor drives. The board consists of a floating-point DSP TMS320C31, a micro-controller TMS320P14 acting as slave-DSP for the digital I/O subsystem, A/D and D/A converters, and encoder interfaces [97]. The main DSP processes numerically intensive algorithms at a frequency of 60 MHz. The

slave-DSP performs digital I/O and PWM generation. The A/D converters convert the analog feedback signals of ±10 V into digital format so that the DSP can read in the measured quantity. Such conversions are used for the measured stator currents and the motor torque feedback signal. Conversely, the D/A converters convert the digital signals in the DSP into analog signals of ±10 V so that they can be displayed on the oscilloscope. The encoder interface provides the interfacing of the DSP with the incremental encoder so that the output of the incremental encoder, which is in discrete pulses, can be quantized into digital form; hence, the data on the rotor-position is obtained. The DS1102 controller board is designed like a PC expansion card so that it can be inserted into the PCI slot of the PC, together with the PC video card or sound card. Using the appropriate software for communication between the PC and the DSP, users can debug the user-program that is loaded in the DSP (via C programming and the Texas Instruments C Compiler), tune the experimental parameters on-line (via COCKPIT®) or display the experimental variables in real-time (via TRACE®). The details of the DSP-DS1102 controller board architecture are provided in Appendix B.

5.3.2 PWM inverter

A 3-phase, 2.2 kW PWM inverter is used as the power circuit for driving the PMSM. The inverter consists of a IGBT module (MUBW 10-12A7), DC-link capacitors, transformer board and driver board. The IGBT module used in the PWM inverter is IXYS model (MUBW 10-12A7). Details of the inverter are given in Appendix C.

5.3.3 Integrated interface platform

In the implementation of the experimental PMSM drive setup, it is necessary to provide a hardware interface between the motor drive and DSP-DS1102. The

hardware interface performs the following functions:

1. Generating mid-symmetrical PWM signals using EX-OR gates.
2. Generating six PWM signals that control the six switches of the PWM inverter.
3. Incorporating dead-time in the PWM signals.
4. Setting the over-current/over-voltage protections and RESET/STOP functions of the inverter.
5. Buffering the pulse signals generated from the incremental encoder.
6. Provide filtering of the measured current and torque signals.

In the laboratory, an integrated interface platform that incorporates the functions (1) - (6) into modular units has been constructed by research engineers. The platform comprises five cards (or modules), namely the Inverter Control Card, Encoder Interface Card, Digital I/O Card, Current Feedback Card and Torque/Analog Feedback Card. Fig. 5.3 shows a simplified block diagram of the integrated interface platform.

The details of the integrated interface platform are given in Appendix D. Functions of the individual cards are summarized below.

5.3.3.1 Inverter Control Card

The Inverter Control Card is responsible for generating the mid-symmetrical PWM signals. As described in [98], the PWM signals generated by the TMS320P14 slave DSP are always set to ON at the beginning of the PWM period. Thus arises the problem of PWM signal "jitters" relative to the clock and equidistant PWM signals. The mid-symmetrical PWM overcomes this problem. As shown in Fig. 5.3, from the three mid-symmetrical PWM signals, another three signals are obtained

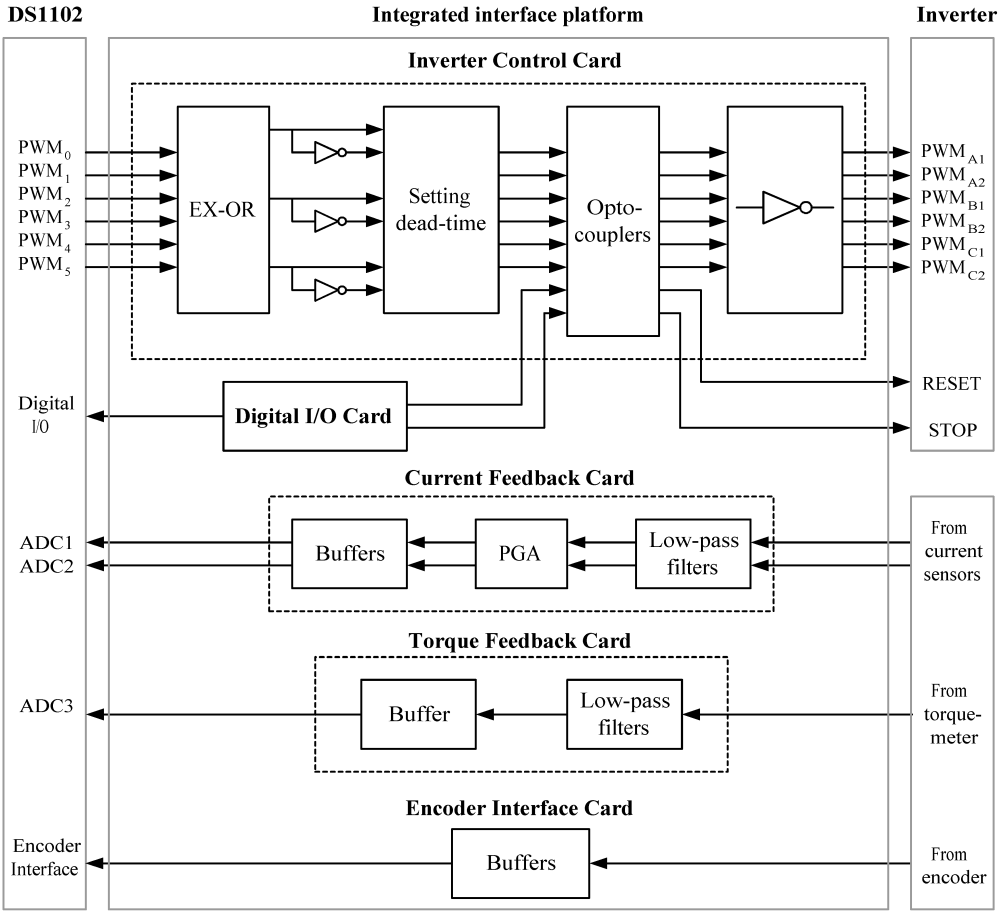

Figure 5.3: Simplified block diagram of the integrated interface platform

from the complement of those three signals. Thus, a total of six PWM signals are generated. Dead-time is also introduced to those six PWM signals to avoid mutual ON states on both the upper and lower switches in the same phase of the inverter. The opto-couplers provide isolation between the low-power control side and the high-power side of the circuit. As the inputs to the inverter are active-low, the PWM signals are inverted before being sent to the inverter inputs. The RESET and STOP signals are from the DSP digital I/O and can be controlled by the user via software.

5.3.3.2 Encoder Interface Card

The incremental encoder has a resolution of 2048 lines per revolution. Its output is in pulse-form and it does not provide information on the absolute rotor position.

Signals from the incremental encoder output are sent through buffers to shape the waveforms and to drive the encoder interface circuit of the DS1102.

5.3.3.3 Digital I/O and Absolute Encoder Card

The DS1102 controller board has 16 ports for digital I/O. These digital I/O lines are controlled by two octal latches. Also, the bus lines for the DS1102 digital I/O are shared with the inputs from the absolute encoder. Therefore, the digital I/O and absolute encoder lines are time multiplexed. However, in the PMSM experimental setup, the absolute encoder is not used. Therefore, this card is only for use of digital I/O.

5.3.3.4 Current Feedback Card

The Current Feedback Card performs signal conditioning of the measured current signals (in voltage form). The measured current signals are filtered to remove the inverter switching noise using simple resistive-capacitive op-amp low-pass filters. The measured current signals are also passed through a voltage buffer. In addition, there is one Programmable Gain Amplifier (PGA) for each channel of the measured current. The PGAs are software programmable via the DS1102 digital I/Os dedicated to them. They can provide amplification of $1\times$, $2\times$, $4\times$ or $8\times$ of the measured current signals to fully utilize the ± 10 V full-scale of the A/D converters for a more accurate computation of the measured current. Fig. 5.3 shows the block diagram of the Current Feedback Card.

5.3.3.5 Torque/Analog Feedback Card

The Torque/Analog Feedback Card performs low-pass filtering of the measured torque signal using a simple resistive-capacitive op-amp low-pass filter. In addition, the filtered torque signal is passed through a voltage buffer before being fed into the A/D converter of the DS1102.

5.3.4 Current sensors

Sufficiently accurate measurements of the motor phase currents are essential to ensure high-performance in the PMSM drive system. In the experimental setup, two current sensors are utilized to measure the phase-a and -b currents. The measured currents are converted into voltage signals scaled to the range ± 10 V by using resistors of appropriate resistances. These voltage signals are then fed into the A/D converters of the DS1102.

In the PMSM experimental setup, the LEM module LA 25-NP current sensors are used. The current sensors, resistors and the power supply for the current sensor are included on the current sensor board. Details of the current sensor board are provided in Appendix E.

5.3.5 Loading system

The PMSM drive loading system consists of a DC machine, a DC power supply in series with the armature side of the DC machine which carries an armature current I_a and another DC power supply which provides field excitation. Fig. 5.4 shows the configuration for the loading system.

In Fig. 5.4, the DC machine is connected in a separately excited configuration. The DC machine runs as a generator, providing load torque for the PMSM. Rated voltage is applied on the field side to provide the rated flux ϕ_f. From the voltage and current equations for the DC machine:

$$E_a = k\phi_f \omega_m \tag{5.1}$$

$$I_a = \frac{E_a - V_s}{R_a} \tag{5.2}$$

where E_a is the back-emf generated, V_s is the external DC voltage source connected in series with the armature winding to increase the load torque, $k\phi_f$ is the back-emf constant, ω_m is the motor speed and R_a is the internal armature resistance. The

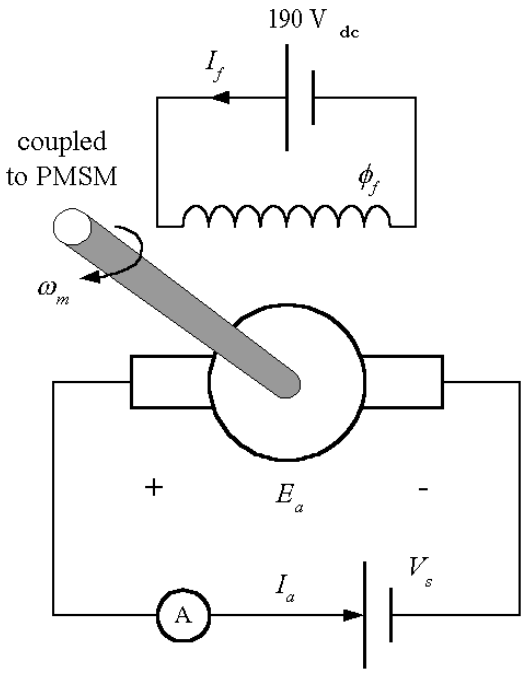

Figure 5.4: Configuration for the PMSM loading system

load torque generated τ_L is expressed as:

$$\tau_L = k\phi_f I_a = \frac{(k\phi_f)^2}{R_a}\omega_m - \frac{k\phi_f V_s}{R_a} \tag{5.3}$$

Therefore, assuming other quantities remain constant, load torque τ_L is proportional to the speed of the PMSM. Details of the DC machine are included in Appendix A.

5.3.6 Torque transducer

Although the instantaneous motor torque in the proposed scheme is obtained by means of on-line estimation, a torque transducer is used to verify the accuracy of the estimated torque. The torque transducer has a high bandwidth output of 500 Hz, which enables the detection of instantaneous torque. As a result, presence of any harmonics in the measured torque that is higher than 500 Hz will be attenuated.

The torque transducer used in the implementation of the experimental PMSM drive is MCRT® 49001V(1-2) model, with rated torque equal to 11.3 Nm, rated

speed equal to 15,000 rpm. Details of the torque transducer are provided in Appendix F.

5.4 Software Environment

The proposed control schemes on the PMSM drive are implemented using the TMS320C31 DSP. The TMS320C31 has a high speed CPU and adequate memory for software implementation. It has a 60 MHz instruction frequency enabling a high sampling rate in the drive system. Fig. 5.5 shows the interactions among the software during the DSP program execution.

As shown in Fig. 5.5, when the program source codes in C are downloaded into the DSP, the Texas Instruments (TI) C Compiler first converts the C source codes into TMS320C31 Assembly language source codes by compiling, assembling and linking of the C source code modules. Then the assembler translates the Assembly language source codes into machine language object files. The object files are then loaded into the DSP, and the DSP begins program execution. When the program execution begins, using the software COCKPIT [99], the user is able to modify the process variables, control parameters on-line, or to monitor process variables, etc. Therefore, if COCKPIT is required, it has to be first included in the user program before downloading. Another software that maintains communication with the DSP during program execution is TRACE. Using TRACE, real-time process variables can be acquired for storage or display purposes. However, unlike in COCKPIT where processing time overhead incurred is negligible relative to the sampling time, TRACE consumes a significant amount of processing time, and hence, it substantially limits the fastest sampling time of the system. Therefore, in the implementation of the proposed PMSM scheme, TRACE is not invoked so as to maintain the sampling time to be as fast as possible. Real-time process variables are acquired via the oscilloscope.

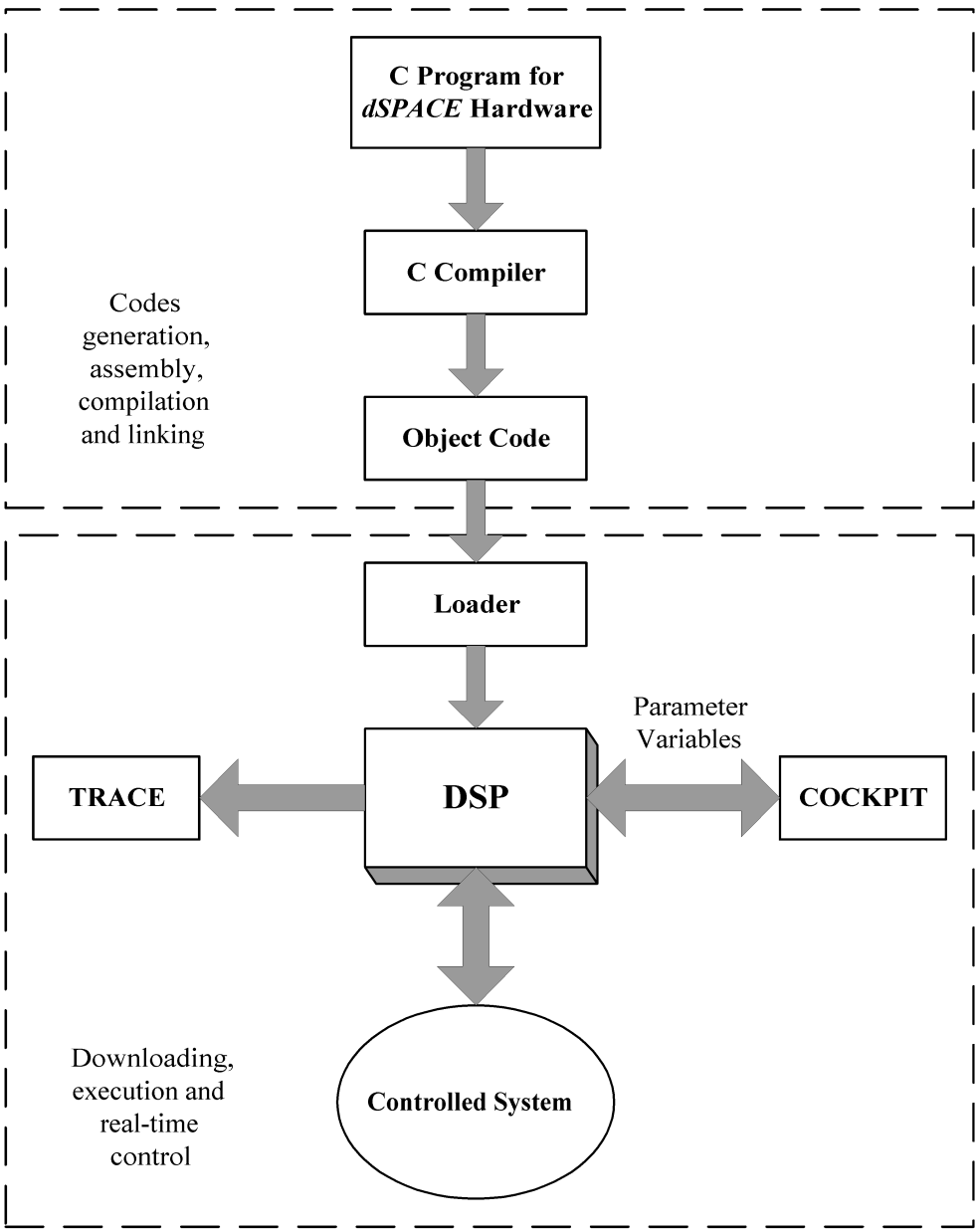

Figure 5.5: Interactions among software during DSP program execution

5.5 Control Program Algorithm

The entire control program for the implementation of the pulsating torque minimization scheme in the PMSM is written in C language [100]. While it is possible to implement the control program using *dSPACE* rapid-prototyping software tools consisting of SIMULINK, MATLAB, Real-Time Workshop (RTW) and Real-Time Interface (RTI), programming in C offers greater flexibility in the control program. Using C programming, it is possible to perform matrix manipulation such as per-

forming a low-pass filtering of a matrix with dimension 2×100 or implementing n-step ahead compensation in the learning memory matrix, but those are not possible in SIMULINK. Furthermore, using C programming, the user has the freedom to optimize the source codes so that it results in the lowest execution time; hence, achieving a fastest sampling time. However, in $dSPACE$ rapid-prototyping software, RTW automatically generates C codes from the SIMULINK block diagrams. C codes generated from RTW results in significantly higher program execution times than those in user-optimized C programs.

Fig. 5.6 describes the flowchart of the main control program that is implemented in C. The flowchart for the Interrupt Service Routine is shown in Fig. 5.7.

5.6 Conclusion

An experimental setup has been constructed to implement the DSP-based PMSM drive scheme. The setup is complete with a 1.64 kW surface-mounted PMSM, a 2.2 kW PWM inverter, a TMS320C31 digital signal processor and an integrated interface platform to provide interface between the digital and analog systems. The controller program is written in C language and downloaded into the DSP using the TI C Compiler that automatically compiles, assembles and links the C-code modules. On-line modifications of the process parameters are done using COCKPIT.

The next chapter proceeds to present the experimental results on the pulsating torque minimization schemes, which were obtained from the PMSM drive setup described in this chapter.

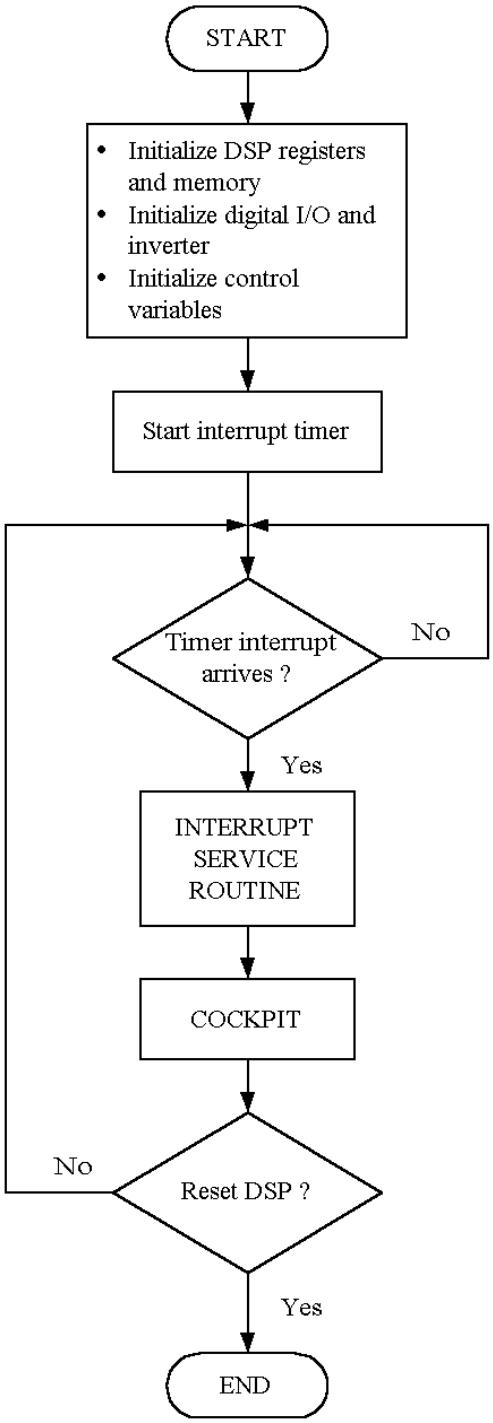

Figure 5.6: Flowchart of the main control program

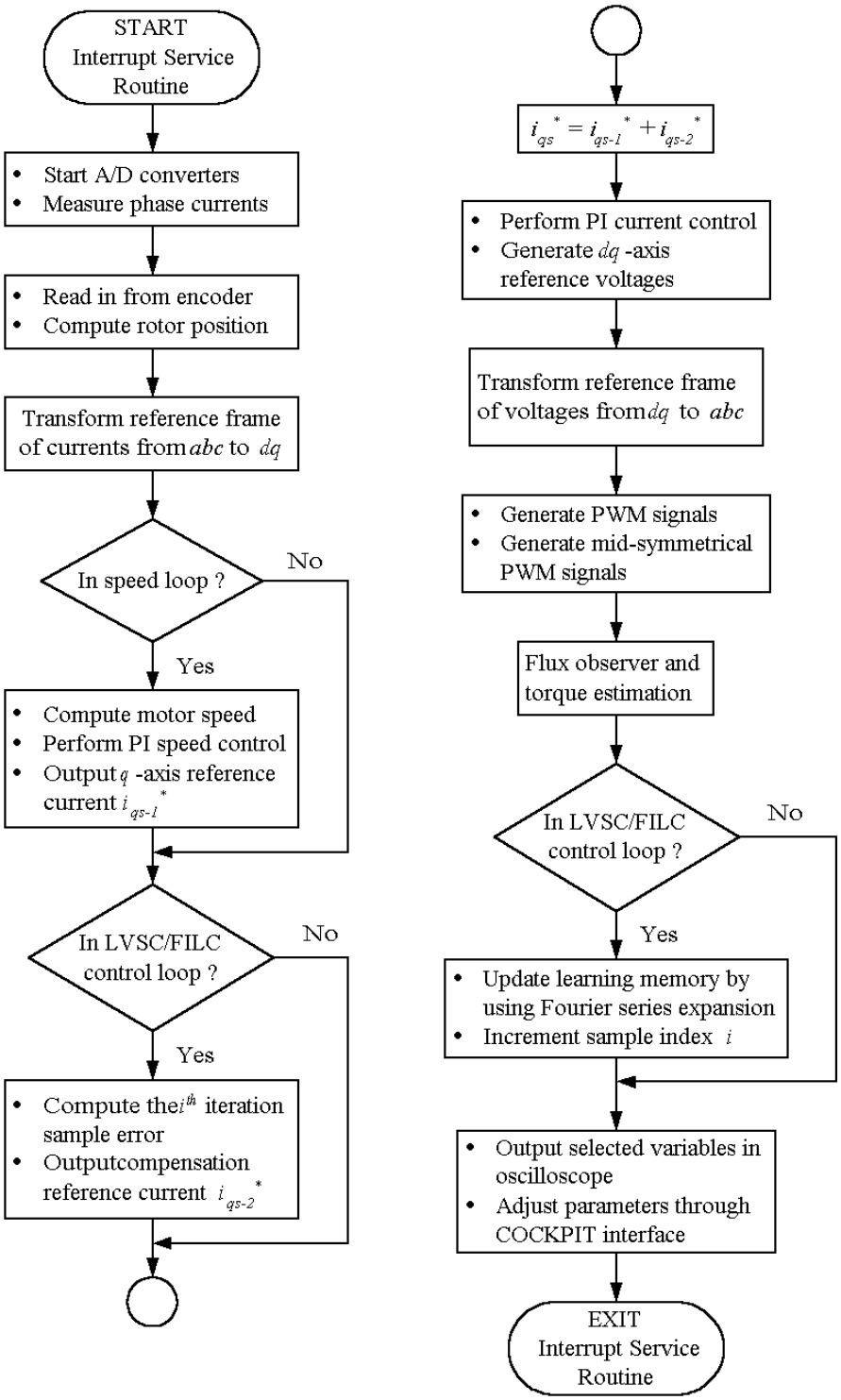

Figure 5.7: Flowchart of the Interrupt Service Routine

Chapter 6

Experimental Results

6.1 Introduction

To further evaluate the performances of the proposed LVSC and FILC schemes for pulsating torque minimization described in Chapter 3 and to verify the simulation results presented in Chapter 4, experimental tests are performed on a DSP-based PMSM drive system. The experimental setup and implementation schemes have been described in details in Chapter 5. Basically, the effectiveness of the two proposed LVSC schemes in minimizing torque (or speed) ripples is compared with that of the conventional torque control with sinusoidal current excitation or PI speed controller. While the effectiveness of the two FILC schemes is compared with that of the basic ILC schemes. Off-line determination of test motor and controller parameters such as motor rotor inertia, damping coefficient, mechanical time constant, and tuning of proportional and integral gains of the PI current and speed controllers are described in Appendix G.

As described in Chapter 4, the torque ripple factor (TRF) and speed ripple factor (SRF) are used as performance indices to evaluate the effectiveness of the proposed pulsating torque (or speed) ripples minimization schemes. The experiments were conducted under different operating conditions, with speeds ranging from 0.005 p.u.(10 rpm) to 0.05 p.u.(100 rpm) and load torques from 0.20 p.u.(1.56 Nm) to 0.795 p.u.(6.20 Nm). The TRF (or SRF) of the drive system without the pro-

posed compensation controller is first determined. Subsequently, compensation currents generated from the proposed LVSC or FILC scheme are applied and the corresponding TRF (or SRF) is re-evaluated.

Section 6.2 presents the experimental results of the proposed LVSC torque (or speed) ripples compensation schemes. In Section 6.3, the experimental results of the proposed FILC torque (or speed) ripples compensation schemes have been presented. A separate section 6.4 contributes to addressing the additional torque pulsations caused by the DC generator, which is coupled with the PMSM for loading purpose. Finally, Section 6.5 concludes this chapter.

6.2 LVSC Compensation Schemes

Three LVSC compensation schemes are tested based on the experimental setup, and the test results are compared with those obtained from the conventional control schemes:

1. LVSC pulsating torque compensation scheme with feedback signals from a torque transducer;
2. LVSC pulsating torque compensation scheme with feedback signals from torque estimator;
3. LVSC speed ripple compensation scheme.

6.2.1 LVSC pulsating torque compensation scheme with feedback signals from a torque transducer

In this scheme, the feedback torque signals are obtained by using a torque transducer which has a high-bandwidth output (500 Hz). The torque transducer is capable of providing all harmonics information in the torque signal, based on an operating speed of 100 rpm and consideration of the 12^{th} order harmonics.

Fig. 6.1 (a) shows the steady-state torque response of the conventional CR-PWM drive scheme when the operating conditions are $\omega_m = 0.025$ p.u.(50 rpm), $\tau_L = 0.205$ p.u. (1.60 Nm). The corresponding TRF is 14.23%. For the purpose of clearness, we only pick up the 1^{st}, 2^{nd}, 6^{th} and 12^{th} harmonic components in the frequency spectrum, which are of our concern. They are shown in Fig. 6.1 (b). Fig. 6.2 (a) shows the steady-state torque response of the proposed LVSC torque control scheme under the same operating conditions. With the LVSC torque ripple compensation scheme being applied, the corresponding TRF is improved from 14.23% to 2.82%, in other words, the torque ripples are reduced by a factor of 5. To verify the effectiveness of the proposed LVSC scheme under a heavy load, the PMSM is operated under a load of 0.795 p.u.(6.20 Nm) with an operating speed of 0.025 p.u.(50 rpm). Fig. 6.3 shows the steady-state torque response of the CR-PWM scheme. The corresponding TRF is 15.64%. Similarly, Fig. 6.4 shows the steady-state torque response of the proposed LVSC torque control scheme. With the compensation provided by the LVSC scheme, the corresponding TRF is improved to 4.10%.

Table 6.1 shows the numerical results of specific harmonic components obtained from the two schemes. From the results, we can see that the reduction of lower-order harmonics are significant, such as the 1^{st} and 2^{nd} components. However, the reduction of higher-order harmonic components are not significant, and LVSC even enlarges the 12^{th} harmonics a little. This is because of the chattering problem inherent with variable structure controller, although we use saturation function instead of sign function. Besides, the higher-order harmonic components are already comparatively small, which make them sensitive to system errors and noise. Compared these experimental data with those of simulation cases, we can find that the reduction in experiments is not as large as that in simulation tests. Since there are always some errors and noise existing in the practical system which

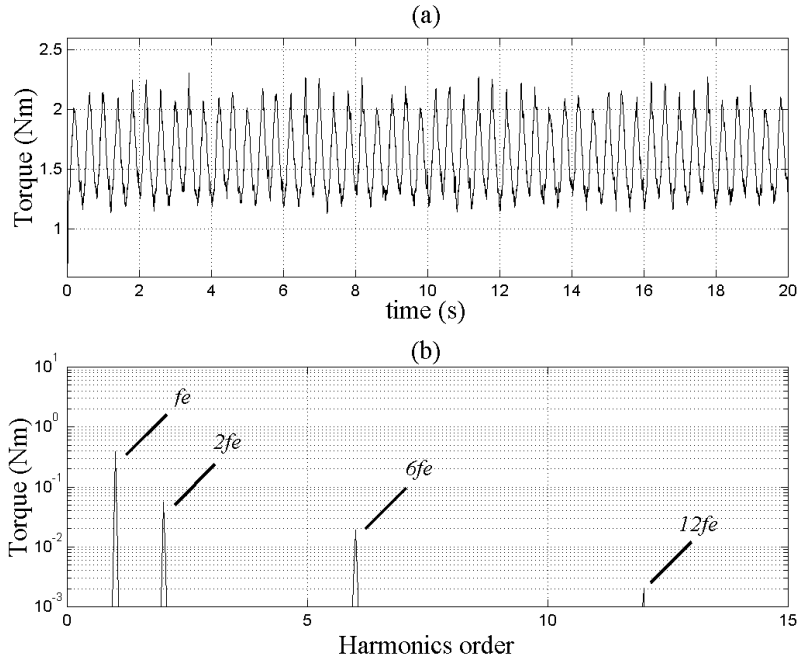

Figure 6.1: Sinusoidal current control scheme: (a) steady-state torque response (TRF=14.23%), and (b) the corresponding frequency spectrum.

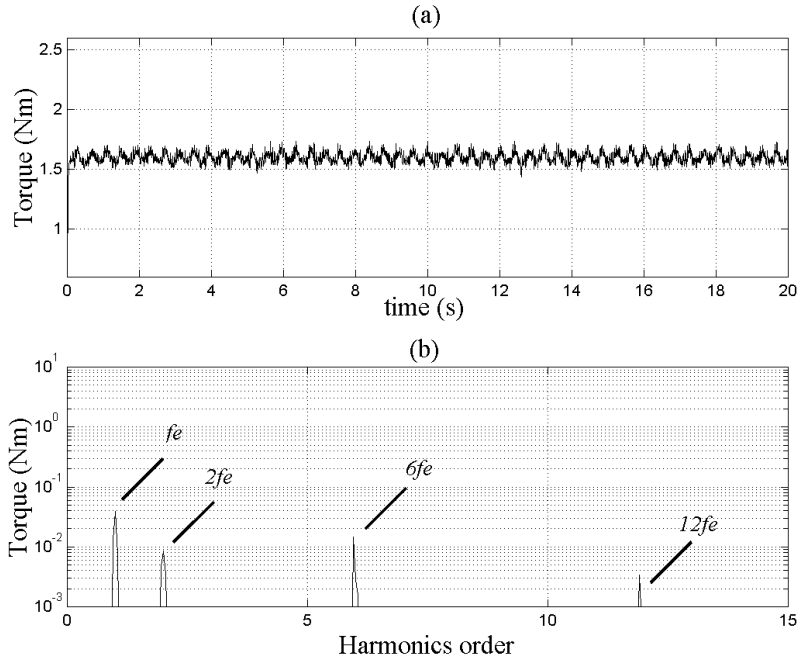

Figure 6.2: Proposed LVSC torque control scheme: (a) steady-state torque response (TRF=2.82%), and (b) the corresponding frequency spectrum.

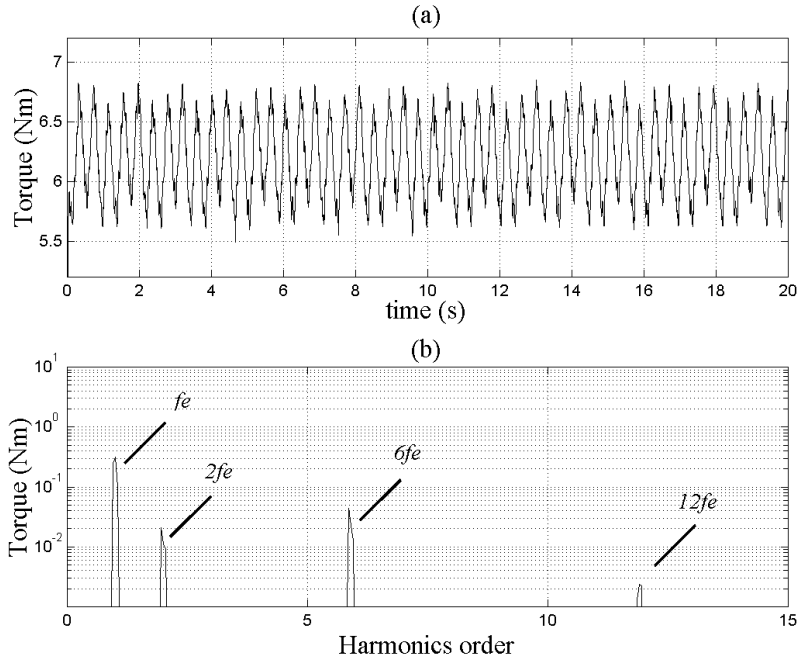

Figure 6.3: Sinusoidal current control scheme: (a) steady-state torque response (TRF=15.64%), and (b) the corresponding frequency spectrum.

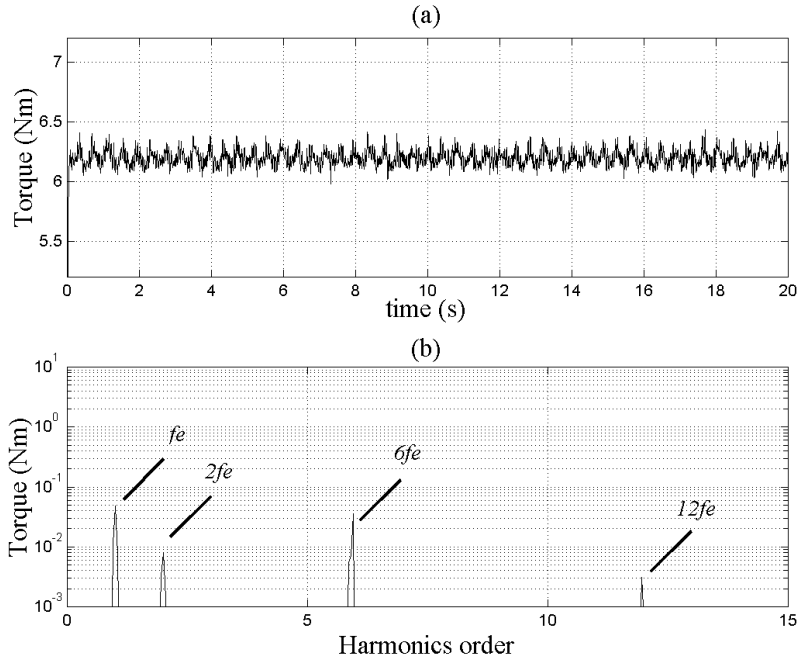

Figure 6.4: Proposed LVSC torque control scheme: (a) steady-state torque response (TRF=4.10%), and (b) the corresponding frequency spectrum.

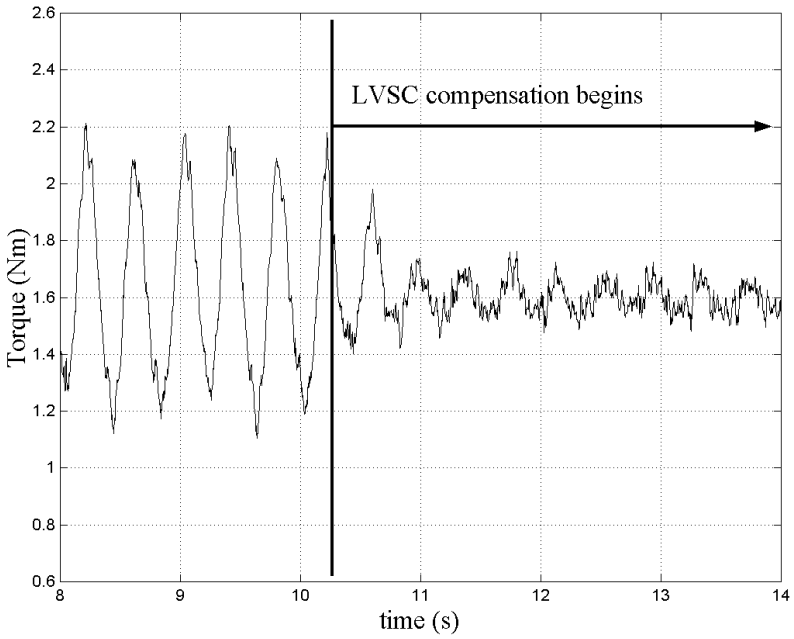

Figure 6.5: Transient torque response when the LVSC compensation scheme is activated. (ω_m=50 rpm, τ_L=1.60 Nm)

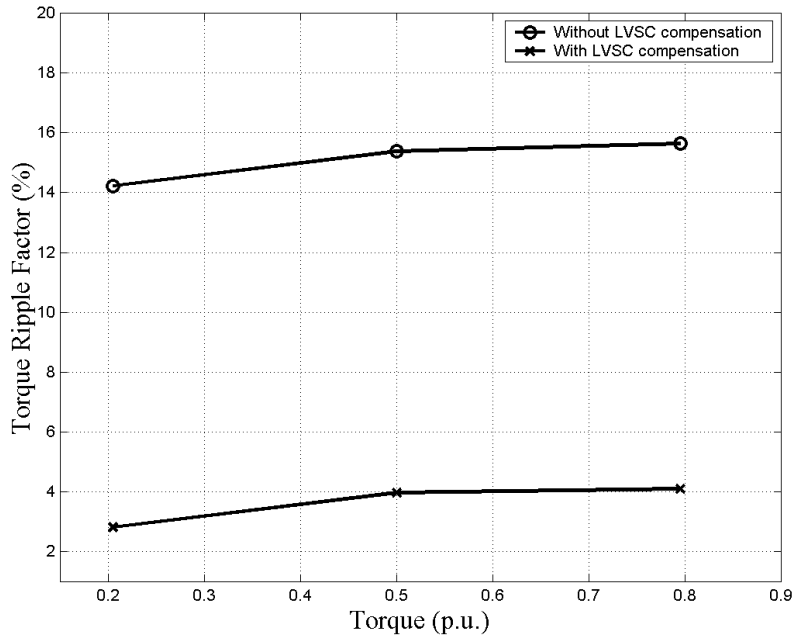

Figure 6.6: The detailed TRFs when PMSM operates at a speed of 50 rpm under different loads without and with LVSC compensation.

cannot be avoided, the pulsating torque cannot be eliminated completely in experimental investigation.

Table 6.1: Torque harmonics with or without LVSC torque compensation.

Loading conditions	Harmonics order	1^{st}	2^{nd}	6^{th}	12^{th}
Light load	without LVSC (Nm)	3.92e-1	5.66e-2	1.94e-2	2.04e-3
(0.205 p.u.)	with LVSC (Nm)	3.91e-2	8.49e-3	1.47e-2	3.38e-3
Heavy load	without LVSC (Nm)	3.16e-1	2.11e-2	4.44e-2	2.38e-3
(0.795 p.u.)	with LVSC (Nm)	4.83e-2	8.02e-3	3.56e-2	3.15e-3

Fig. 6.5 shows the transient torque response when the LVSC compensation scheme is activated. It can be seen that within three iteration periods once the LVSC scheme enabled, torque signal has reached the maximum reduction (time period can be calculated as: $T = \left(\frac{60}{\omega_m \times P_p}\right)$=0.4 sec). The values of TRF under different loading conditions are shown in Fig. 6.6. It gives the TRF when PMSM operates at a speed of 0.025 p.u.(50 rpm) under various loads (0.205 p.u., 0.50 p.u. and 0.795 p.u.) without and with LVSC compensation. According to the results, the effectiveness of the proposed LVSC pulsating torque compensation scheme is verified in suppressing torque ripple by at least three times under various steady-state operating conditions.

6.2.2 LVSC pulsating torque compensation scheme with feedback signals obtained from torque estimator

In this subsection, the effectiveness of the proposed LVSC compensation scheme based on the high gain torque estimator described in Section 3.5 has been evaluated through experimental investigations.

Fig. 6.7 (a) shows the steady-state torque response of the conventional CR-PWM drive scheme when the operating condition are $\omega_m = 0.025$ p.u.(50 rpm), τ_L

= 0.205 p.u. (1.60 Nm). The corresponding TRF is 15.0%. Fig. 6.7 (b) presents the corresponding torque response in frequency spectrum. Fig. 6.8 (a) shows the steady-state torque response of the proposed LVSC torque control scheme under the same operating conditions. With the LVSC compensation scheme applied, it is clear that the TRF is reduced from 15.0% to 1.66%. To study the effect of heavy load torque on the effectiveness of the proposed LVSC scheme, we operated the PMSM at a speed of 0.025 p.u.(50 rpm) with a load torque of 0.795 p.u.(6.20 Nm). Similarly, Fig. 6.9 shows the steady-state torque response of the CRPWM scheme, and Fig. 6.10 shows the steady-state torque response of the proposed LVSC torque control scheme. With the compensation currents provided by the LVSC scheme, the corresponding TRF is improved from 18.5% to 6.28%.

Table 6.2 gives the detailed results of specific harmonic components obtained from the two schemes. According to the data, it can be seen that the 1^{st} and 2^{nd} harmonic components are suppressed by one order of magnitude. The 6^{th} harmonics is also reduced by a factor of more than 3. The 12^{th} component is already small before applying compensation, and hence the reduction is not obvious. Fig. 6.11 gives the

Table 6.2: Estimated torque harmonics with/without LVSC torque compensation.

Loading conditions	Harmonics order	1^{st}	2^{nd}	6^{th}	12^{th}
Light load	without LVSC (Nm)	3.4e-1	3.4e-2	2.5e-3	1.3e-3
(0.205 p.u.)	with LVSC (Nm)	1.4e-2	2.3e-3	2.1e-3	1.0e-3
Heavy load	without LVSC (Nm)	3.2e-1	5.6e-2	8.9e-3	2.8e-3
(0.795 p.u.)	with LVSC (Nm)	1.5e-2	4.7e-3	2.3e-2	3.8e-3

transient response of motor torque when the LVSC compensation scheme is enabled during steady-state operation: $\omega_m = 0.025$ p.u.(50 rpm), $\tau_L = 0.205$ p.u.(1.60 Nm). It can be observed that the torque ripples reach the maximum reduction almost immediately once the proposed LVSC scheme activated. This is different from the

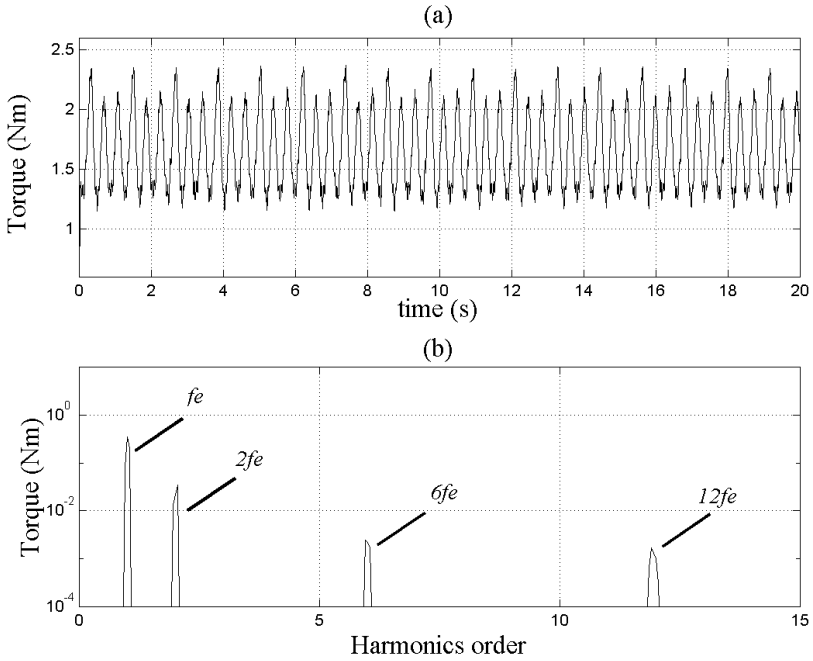

Figure 6.7: Sinusoidal current control scheme: (a) steady-state estimated torque response (TRF=15.0%), and (b) the frequency spectrum.

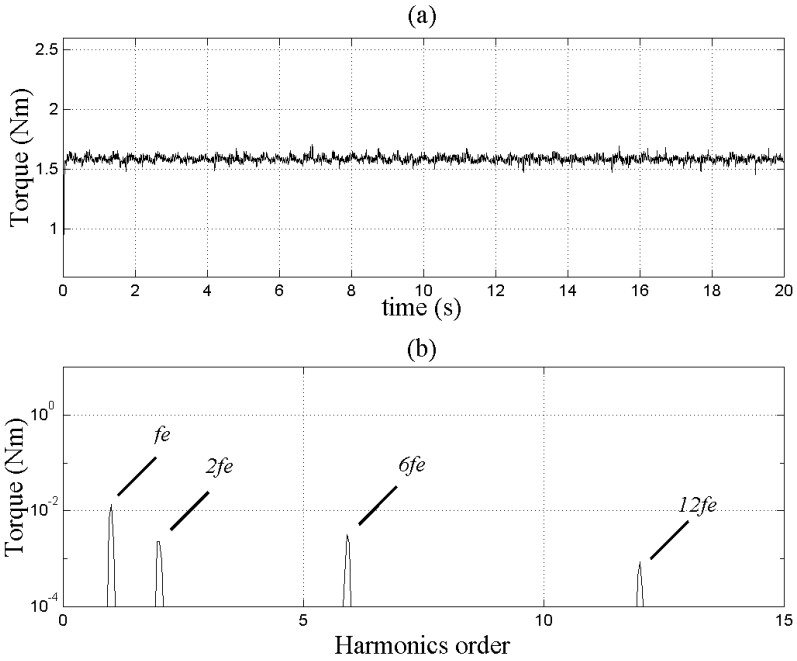

Figure 6.8: Proposed LVSC torque control scheme: (a) steady-state estimated torque response (TRF=1.66%), and (b) the corresponding frequency spectrum.

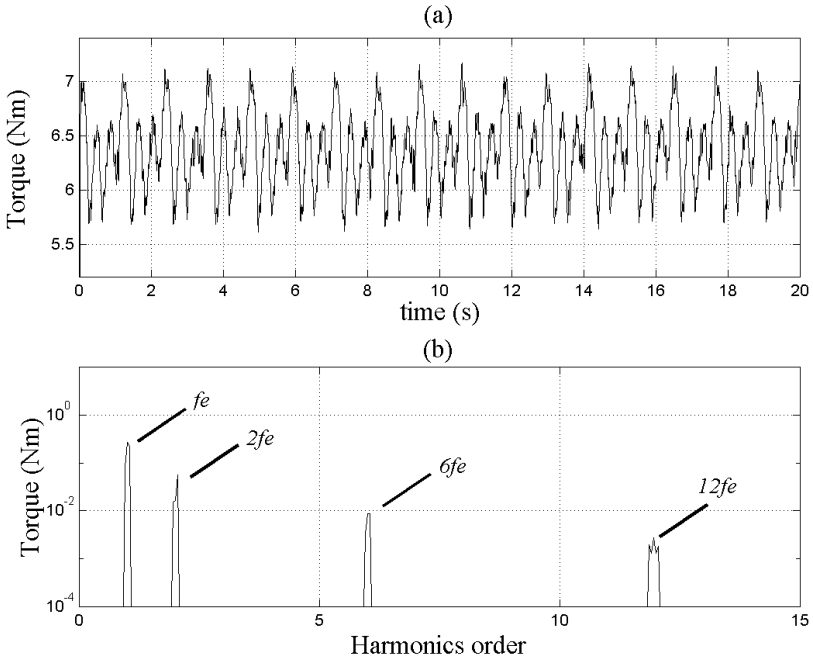

Figure 6.9: Sinusoidal current control scheme: (a) steady-state estimated torque response (TRF=18.5%), and (b) the corresponding frequency spectrum.

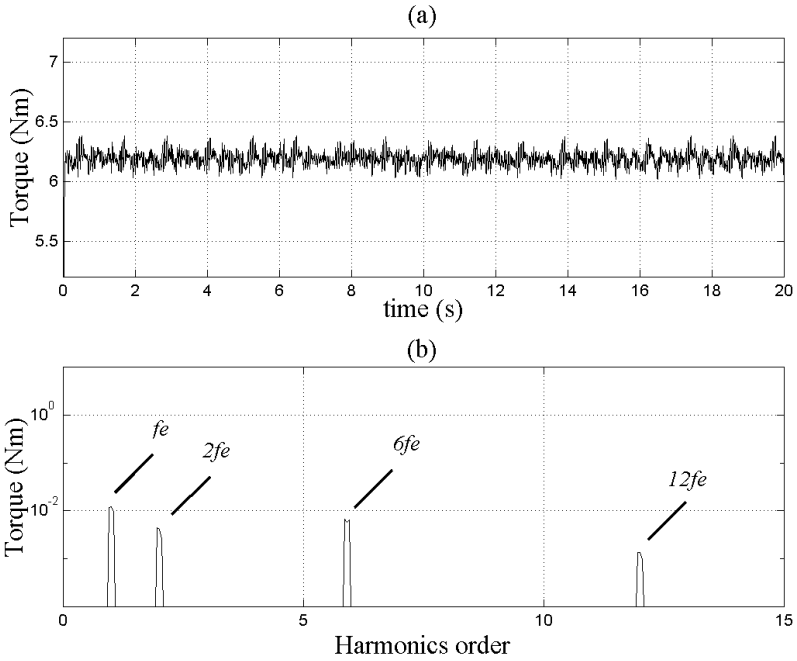

Figure 6.10: Proposed LVSC torque control scheme: (a) steady-state estimated torque response (TRF=6.28%), and (b) the corresponding frequency spectrum.

case, in which instantaneous torque signals are obtained from a torque transducer. In torque estimation, variables from electrical subsystems are used to estimate the flux linkage, and this results in a fast response of torque signals estimated (since the time constant of electrical subsystem is much smaller than that of mechanical subsystem).

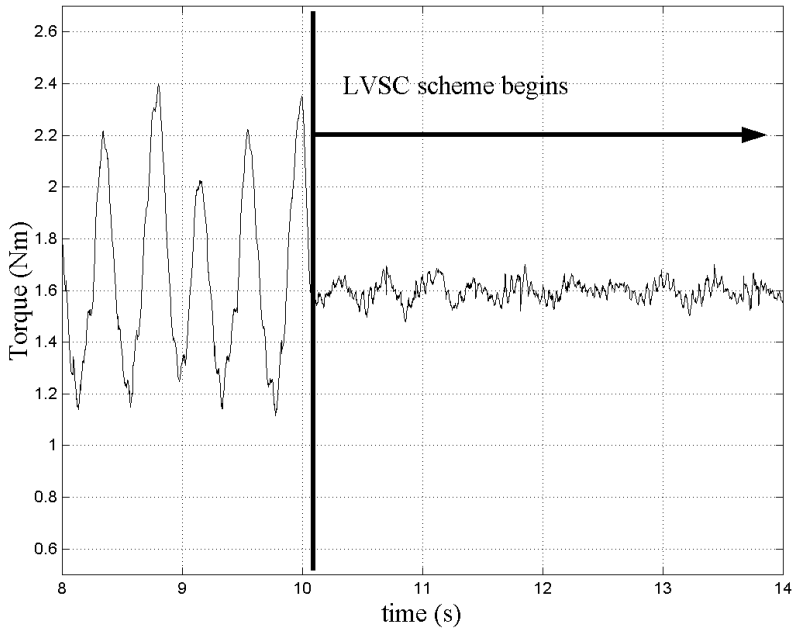

Figure 6.11: Transient torque response when the LVSC compensation scheme is activated. (ω_m=50 rpm, τ_L=1.60 Nm)

6.2.3 LVSC speed ripple compensation scheme

Figs. 6.12 to 6.15 each shows the steady-state speed response in (a) time domain and (b) the corresponding frequency spectrum. Fig. 6.12 shows the speed response when the motor runs at a speed of 0.025 p.u.(50 rpm) under a light load of 0.205 p.u.(1.60 Nm) without LVSC compensation. In this figure, a large speed oscillation can be observed with the corresponding SRF equal to 0.65%. Fig. 6.13 presents the speed waveform under the same working conditions with the LVSC speed ripple compensation scheme being applied. We can see that speed

ripple harmonics are reduced with the SRF equal to 0.25%. To validate the effectiveness of the proposed LVSC speed ripple compensation scheme under heavy loads, a case with a load of 0.795 p.u.(6.20 Nm) was tested. Figs. 6.14 and 6.15 show the steady-state speed responses under the same operating conditions: ω_m = 0.025 p.u.(50 rpm), τ_L = 0.795 p.u.(6.20 Nm). In this case, the SRF is reduced from 0.78% to 0.27% with the proposed LVSC speed ripple compensation scheme being applied.

Table 6.3 gives the values of specific harmonic components obtained from both schemes. The numerical values of SRF under different operating speeds are shown in Fig. 6.16. The figure gives the SRFs when PMSM operates at different speeds (0.005 p.u., 0.025 p.u. and 0.05 p.u.) under a light load of 0.205 p.u.(1.60 Nm) without and with LVSC compensation scheme. According to the results, the effectiveness of the proposed LVSC schemes is verified in suppressing speed ripples under various steady-state operating conditions. As in Fig. 6.16, it can be seen that the SRF is relatively high when motor runs at 50 rpm, since at this speed the peak-to-peak speed ripple reaches comparatively high and so does SRF [80] (at $\omega_e = \sqrt{K_I/J} = \sqrt{0.35/0.0025} = 11.83$ rad/s (37.7 rpm), speed ripple reaches maximum).

Table 6.3: Speed harmonics with or without LVSC speed compensation.

Loading conditions	Harmonics order	1^{st}	2^{nd}	6^{th}	12^{th}
Light load	without LVSC (rpm)	5.75	4.51e-1	7.63e-2	7.00e-2
(0.205 p.u.)	with LVSC (rpm)	6.40e-1	3.50e-1	4.97e-2	4.07e-2
Heavy load	without LVSC (rpm)	5.34	5.49e-1	1.71e-1	1.54e-2
(0.795 p.u.)	with LVSC (rpm)	4.20e-1	2.85e-1	1.32e-1	1.95e-2

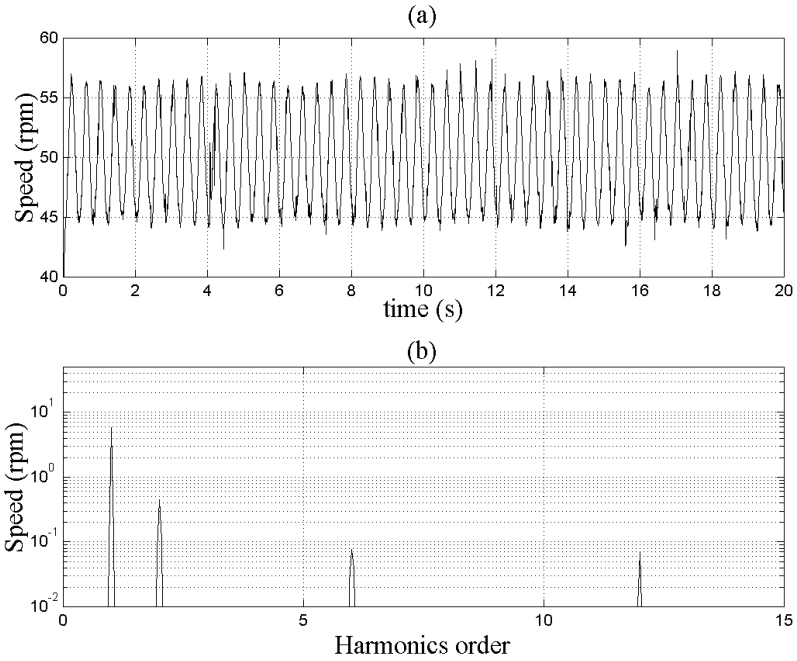

Figure 6.12: Conventional PI speed control scheme: (a) steady-state speed response (SRF=0.65%), and (b) the corresponding frequency spectrum.

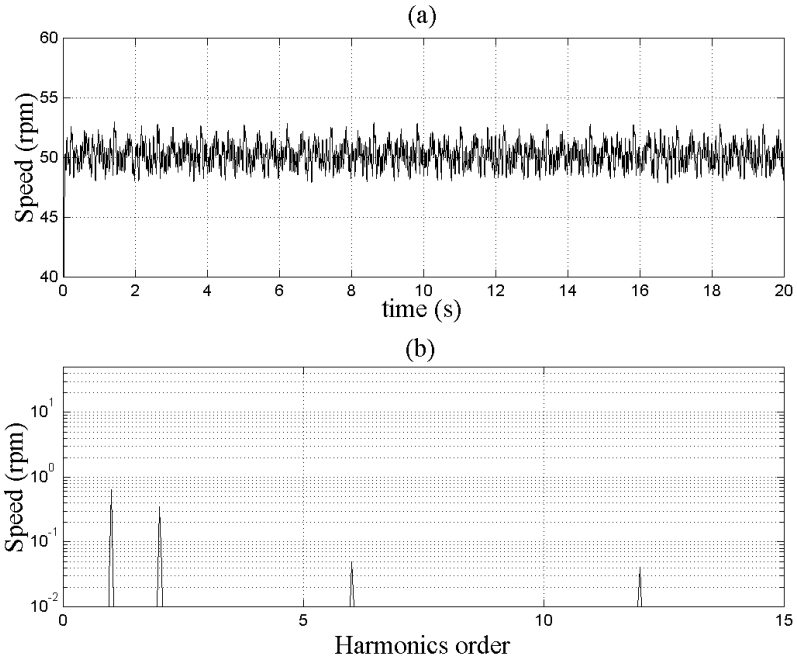

Figure 6.13: LVSC speed control scheme: (a) steady-state speed response (SRF=0.25%), and (b) the corresponding frequency spectrum.

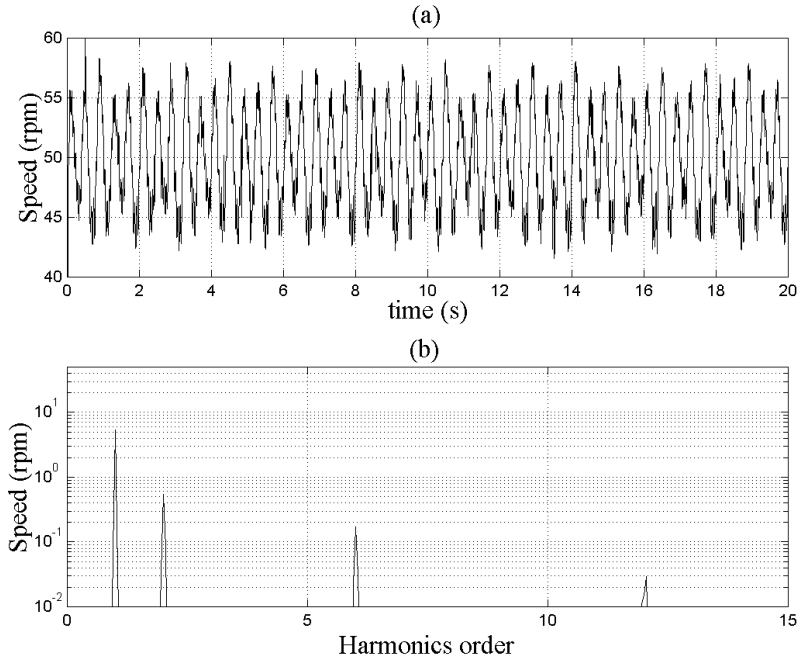

Figure 6.14: Conventional PI speed control scheme: (a) steady-state speed response (SRF=0.78%), and (b) the corresponding frequency spectrum.

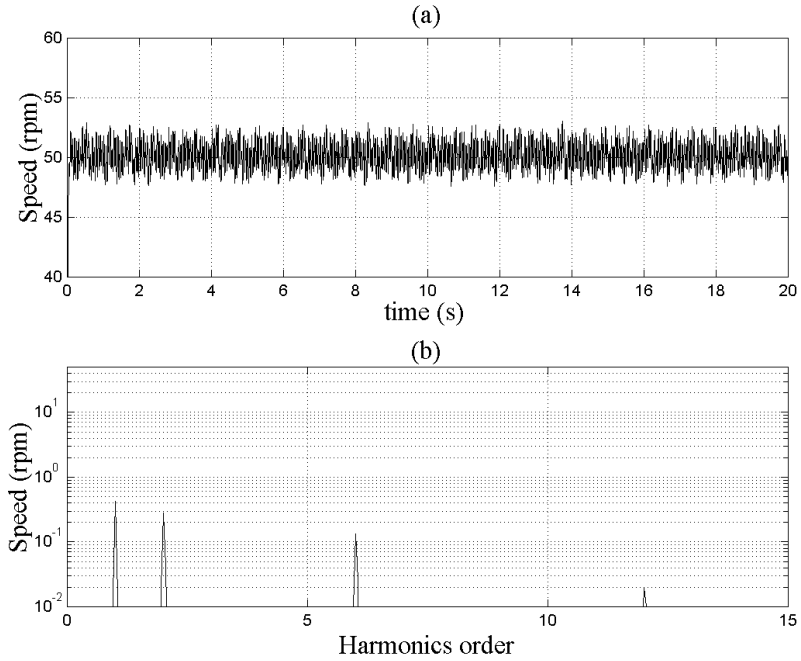

Figure 6.15: LVSC speed control scheme: (a) steady-state speed response (SRF=0.27%), and (b) the corresponding frequency spectrum.

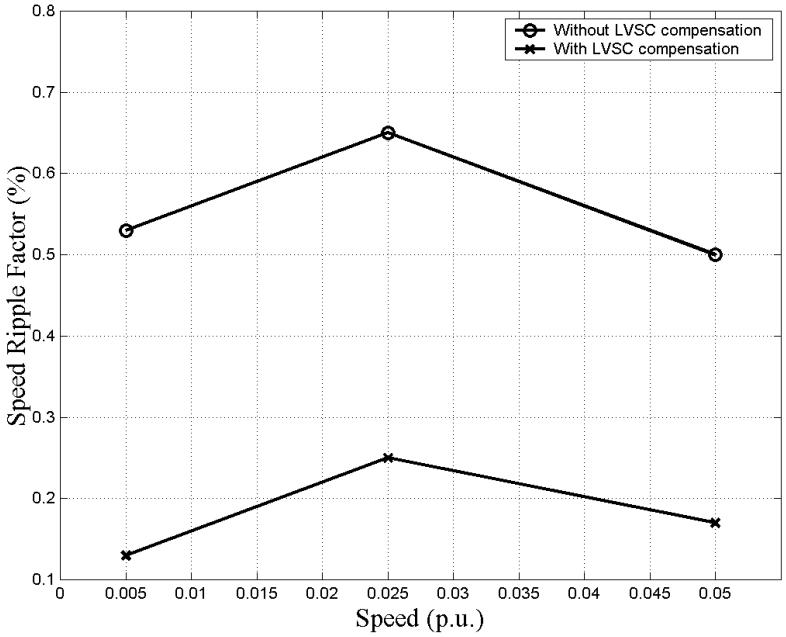

Figure 6.16: SRFs of different speeds under a light load of 1.60 Nm without and with LVSC compensation.

6.3 FILC Compensation Schemes

Similarly, there are three FILC compensation schemes tested, and the test results are compared with those obtained from the basic ILC schemes:

1. FILC pulsating torque compensation scheme with feedback signals obtained from a torque transducer;

2. FILC pulsating torque compensation scheme with feedback signals obtained from torque estimator;

3. FILC speed ripple compensation scheme.

6.3.1 FILC pulsating torque compensation scheme with feedback signals obtained from a torque transducer

Figs. 6.17 to 6.22 each shows the steady-state torque signals in (a) time domain and (b) the corresponding frequency spectrum (the 1^{st}, 2^{nd}, 6^{th} and 12^{th} harmonic components). Fig. 6.17 shows the torque response when the motor was operated at a speed of 0.025 p.u.(50 rpm) under a light load of 0.205 p.u.(1.60 Nm) without ILC compensation. It can be seen that the torque consists of significant ripples and the corresponding TRF is approximately 14.23%. Figs. 6.18 and 6.19 present the torque signals under the same working conditions with the basic ILC and FILC compensation schemes, respectively. With the compensation schemes being applied, it is clear that the TRF is reduced from 14.23% to 4.3% for the ILC scheme (Fig. 6.18) and 3.9% for the FILC scheme (Fig. 6.19).

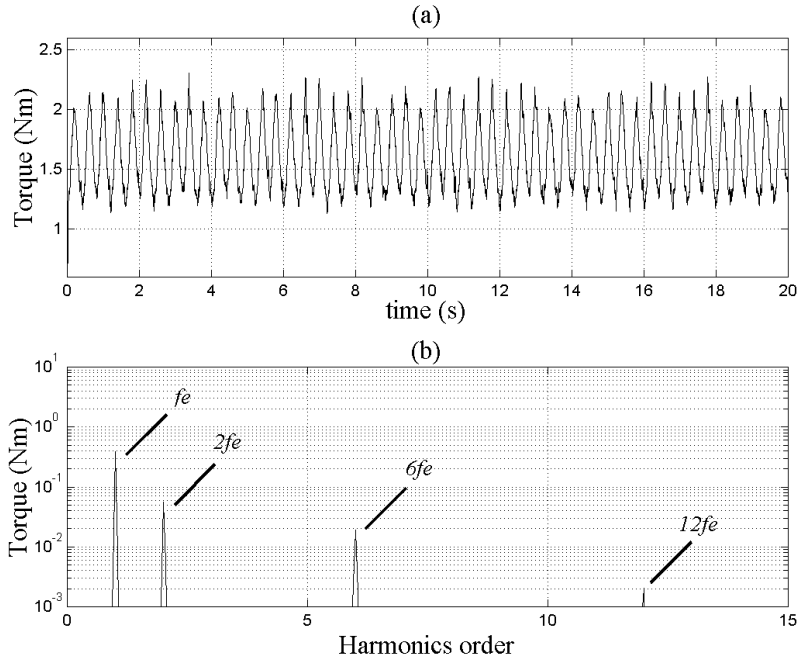

Figure 6.17: Sinusoidal current control scheme: (a) steady-state torque response (TRF=14.23%), and (b) the corresponding frequency spectrum.

Figs. 6.20 to 6.22 are arranged in the same sequence, and the operating con-

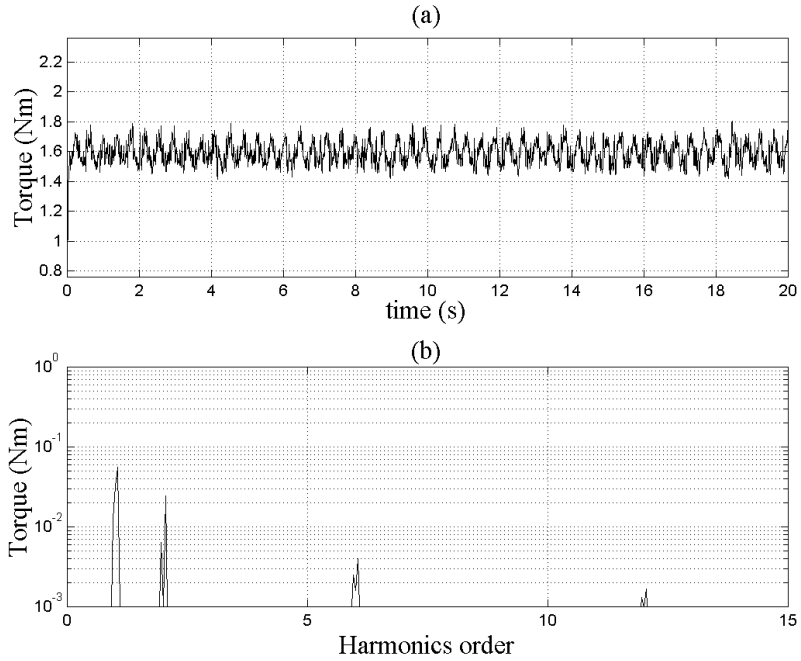

Figure 6.18: Basic ILC torque control scheme: (a) steady-state torque response (TRF=4.3%), and (b) the corresponding frequency spectrum..

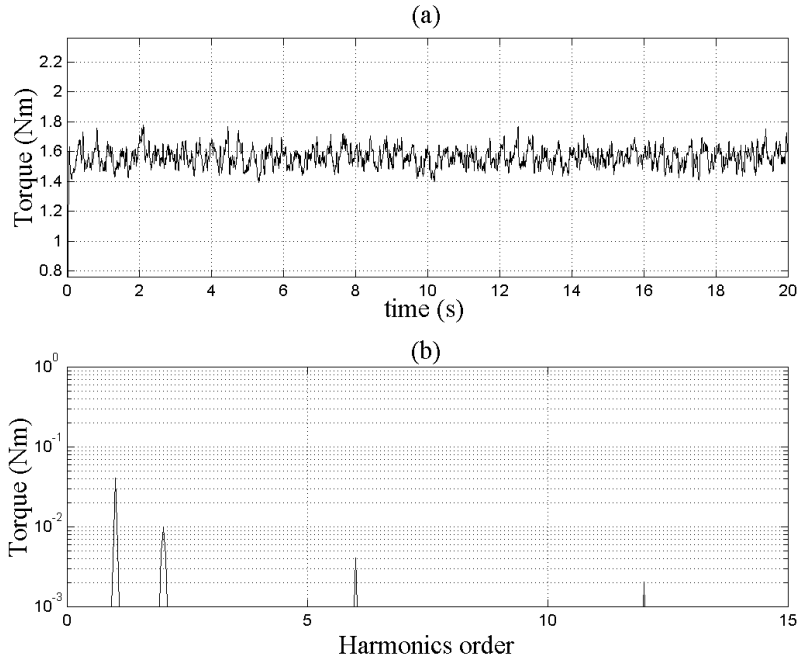

Figure 6.19: Proposed FILC torque control scheme: (a) steady-state torque response (TRF=3.9%), and (b) the corresponding frequency spectrum.

ditions of these figures are $\omega_m = 0.025$ p.u.(50 rpm), $\tau_L = 0.795$ p.u.(6.20 Nm). In these cases the corresponding TRF is suppressed from 15.64% to 4.8% and 4.5%, respectively. We can see that pulsating harmonics were reduced with the application of the ILC control scheme, and a further reduction is possible by using the frequency-domain learning method. In this case, the 6^{th} harmonic component after compensated by the ILC scheme is not much suppressed as that in the light load case. This is because when motor operates under heavier loads, the DC generator is coupled and excited for loading purpose, and the resultant torque pulsations induced from the generator side that mainly consist of non-integer multiple harmonics become larger. These harmonics cannot be compensated by the ILC scheme, because they are not integer multiples of the fundamental frequency. Table 6.4 gives the values of specific harmonics obtained from three schemes.

Table 6.4: Torque harmonics with or without ILC/FILC torque compensation.

Loading conditions	Harmonics order	1^{st}	2^{nd}	6^{th}	12^{th}
Light load (0.205 p.u.)	without ILC (Nm)	3.92e-1	5.66e-2	1.94e-2	2.04e-3
	with ILC (Nm)	5.5e-2	2.4e-2	4.0e-3	1.6e-3
	with FILC (Nm)	4.0e-2	9.5e-3	4.0e-3	2.0e-3
Heavy load (0.795 p.u.)	without ILC (Nm)	3.16e-1	2.11e-2	4.44e-2	2.38e-3
	with ILC (Nm)	6.8e-2	1.6e-2	4.3e-2	5.0e-3
	with FILC (Nm)	3.7e-2	1.0e-2	7.8e-3	2.0e-3

Fig. 6.23 gives the transient response of motor torque when the FILC compensation scheme is enabled during steady-state operation: $\omega_m = 0.025$ p.u. (50 rpm), $\tau_L = 0.20$ p.u.(1.56 Nm). It can be observed that after 4 iteration periods, the torque ripple reaches the maximum reduction. The transient response of motor torque can be seen from Fig. 6.24 when the reference torque is changed from 3.83 Nm to 3 Nm with the FILC controller applied. In this case, although the motor speed is changed due to the reduction of reference torque, the FILC scheme

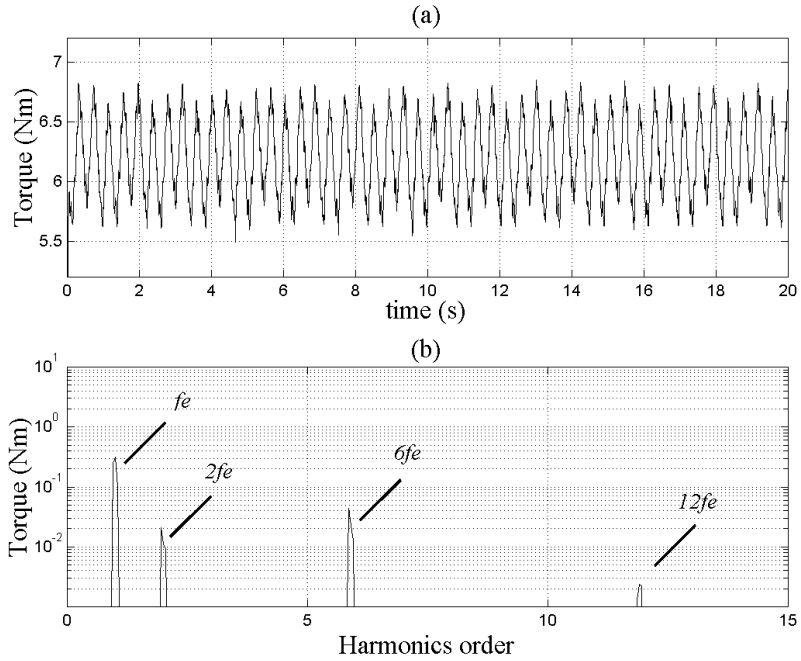

Figure 6.20: Sinusoidal current control scheme: (a) steady-state torque response (TRF=15.64%), and (b) the corresponding frequency spectrum.

is not affected because the memory size in the previous controller is fixed in accordance with electrical angle θ_e, instead of being calculated according to the actual speed. The numerical values of TRF for different operating speeds are shown in Fig. 6.25. It gives the TRF when PMSM is operated at different speeds (0.0125 p.u., 0.025 p.u., 0.0375 p.u. and 0.05 p.u.) under a heavy load of 0.64 p.u.(5.00 Nm) without or with ILC/FILC compensation. According to the results, the effectiveness of the proposed FILC schemes is verified in suppressing torque ripple by at least three times under various steady-state operating conditions.

Apparently, the FILC scheme is better than the basic ILC scheme implemented with a forgetting factor. This is because the basic learning cannot eliminate errors completely due to the introduction of forgetting factor. On the other hand, Fourier series expansion keeps the necessary information of the integer harmonics present in control signal, while removing those white noise through the integration of coefficients over the entire learning period. However, ideally it is

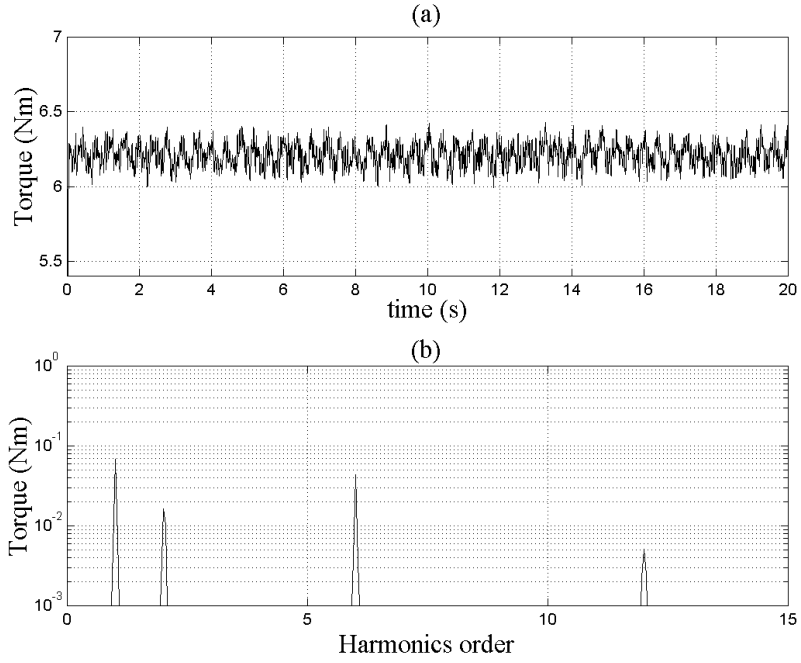

Figure 6.21: Basic ILC torque control scheme: (a) steady-state torque response (TRF=4.8%), and (b) the corresponding frequency spectrum.

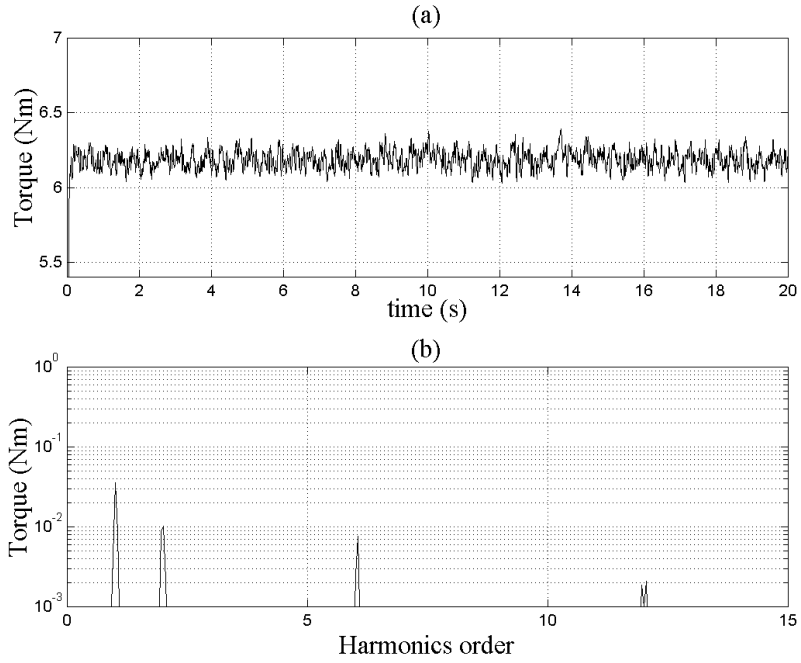

Figure 6.22: Proposed FILC torque control scheme: (a) steady-state torque response (TRF=4.5%), and (b) the corresponding frequency spectrum.

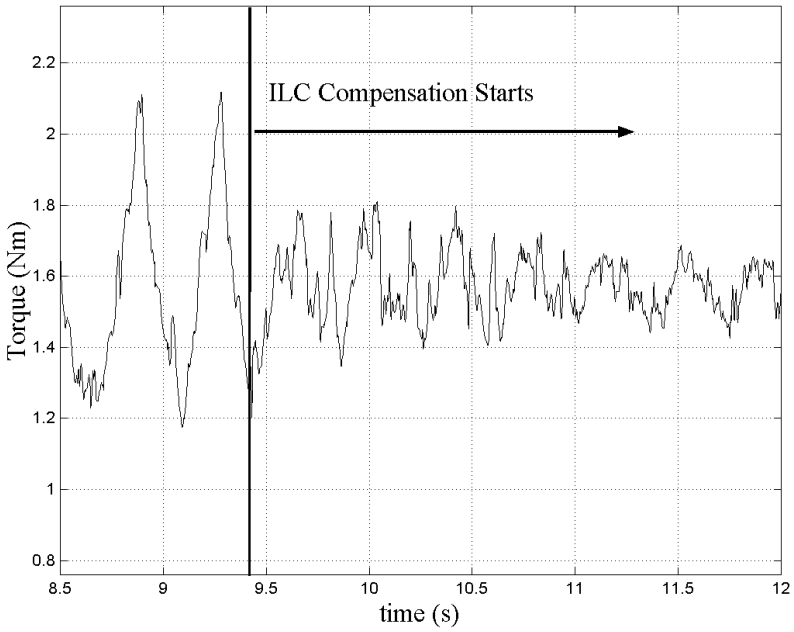

Figure 6.23: The transient torque response when the FILC compensation scheme is activated (ω_m=50 rpm, τ_L=1.56 Nm).

expected that with frequency-domain learning implementation the torque ripple can be completely eliminated, it cannot be achieved practically and needs further investigations.

6.3.2 FILC pulsating torque compensation scheme with feedback signals obtained from torque estimator

Fig. 6.26 shows the estimated torque responses without FILC compensation in (a) time domain and (b) the corresponding frequency spectrum when motor operates at a speed of 0.025 p.u.(50 rpm) under a light load of 0.205 p.u.(1.60 Nm). It can be seen that the torque consists of significant ripples and the corresponding TRF is 15.0%. Fig. 6.27 presents the torque responses under the same working conditions with FILC compensation. With the FILC compensation scheme applied, the TRF is reduced to 3.4%, in other words, the torque ripples are suppressed by a factor of more than 4. Subsequently, the effect of increasing the load torque on

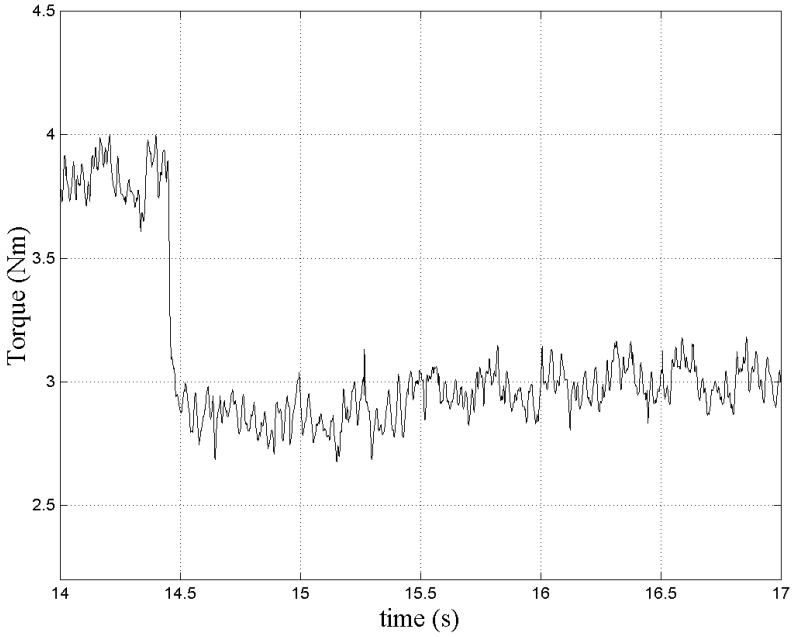

Figure 6.24: The transient torque response when the load torque is reduced from 3.83 Nm to 3 Nm with FILC scheme always on.

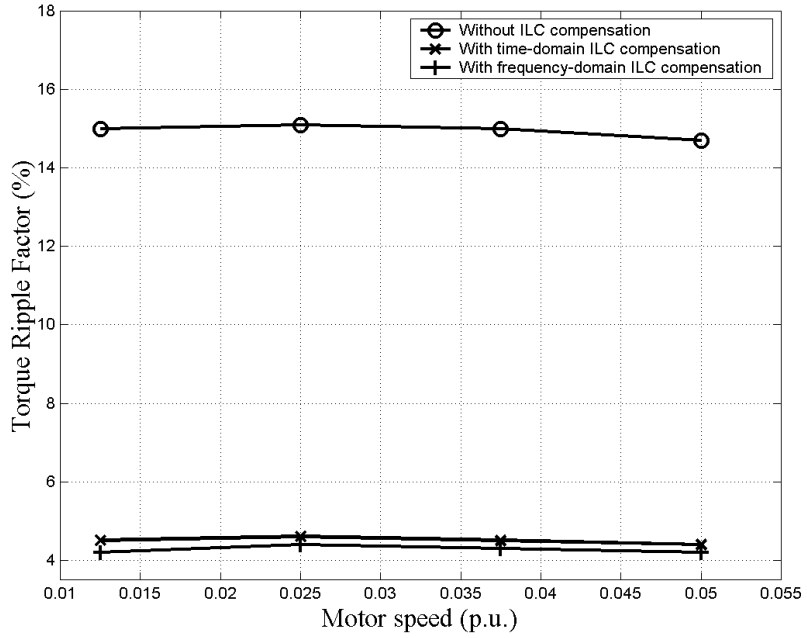

Figure 6.25: The detailed TRFs when PMSM operates at different speeds under a heavy load of 5.00 Nm without or with ILC/FILC compensation.

the effectiveness of the proposed FILC scheme has been studied. Operating the PMSM at a speed of 0.025 p.u.(50 rpm), a load torque of 0.795 p.u.(6.20 Nm) is applied to the motor. Fig. 6.28 shows the estimated torque responses without FILC compensation in (a) time domain and (b) the corresponding frequency spectrum. Fig. 6.29 shows the torque responses with FILC compensation under the same working conditions. In this case, the corresponding TRF is suppressed from 18.5% to 4.0%. The detailed values of specific harmonic torque components are shown in Table 6.5.

Table 6.5: Estimated torque harmonics with or without FILC torque compensation.

Loading conditions	Harmonics order	1^{st}	2^{nd}	6^{th}	12^{th}
Light torque (0.205 p.u.)	without FILC (Nm)	3.4e-1	3.4e-2	2.5e-3	1.3e-3
	with FILC (Nm)	2.6e-2	4.4e-3	1.7e-3	1.3e-3
Heavy load (0.795 p.u.)	without FILC (Nm)	3.2e-1	5.6e-2	8.9e-3	2.8e-3
	with FILC (Nm)	3.2e-2	4.9e-3	4.3e-3	1.3e-3

6.3.3 FILC speed ripple compensation scheme

Figs. 6.30 to 6.35 each shows the steady-state speed response in (a) time domain and (b) the corresponding frequency spectrum. Fig. 6.30 shows the speed waveform when the motor is operated at a speed of 0.025 p.u.(50 rpm) under a light load of 0.205 p.u.(1.60 Nm) without ILC compensation. In this figure, a large speed oscillation can be observed with the corresponding SRF equal to 0.65%. Figs. 6.31 and 6.32 present the speed waveforms under the same working conditions with ILC and FILC compensation schemes, respectively. Speed ripples are reduced with the SRF equal to 0.15% after the basic ILC scheme being activated. Further reduction is possible by using the frequency domain learning method with the SRF reduced to 0.10%.

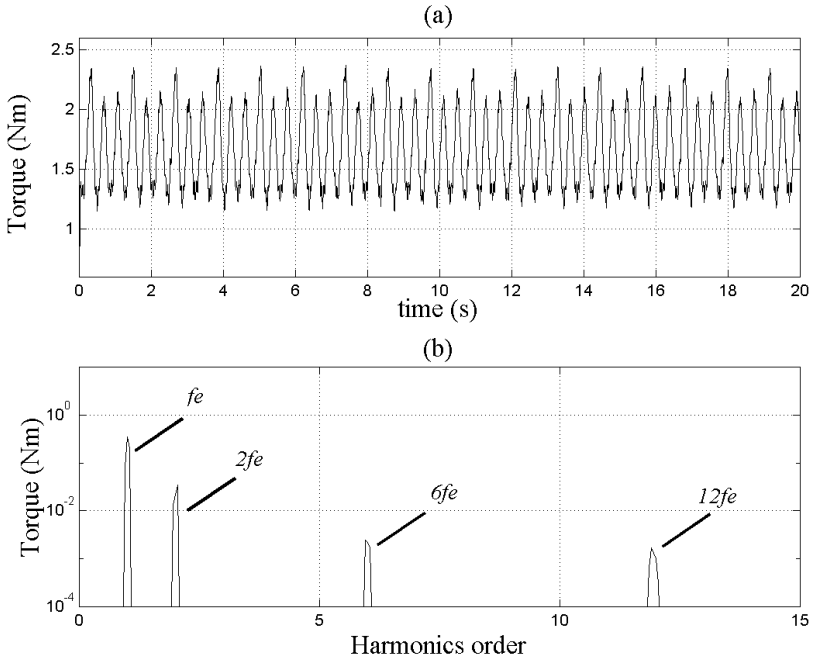

Figure 6.26: Sinusoidal current control scheme: (a) steady-state estimated torque response (TRF=15.0%), and (b) the corresponding frequency spectrum.

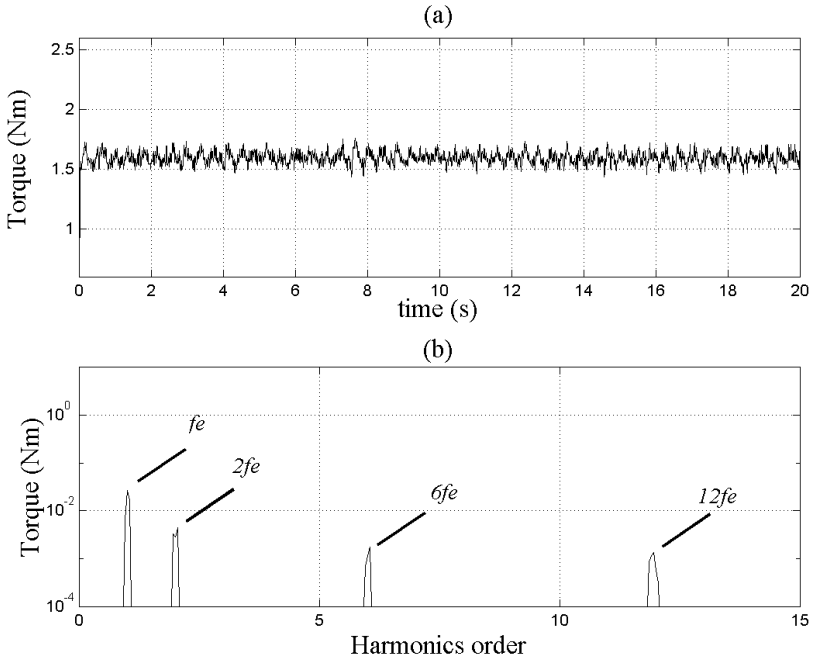

Figure 6.27: Proposed FILC torque control scheme: (a) steady-state estimated torque response (TRF=3.4%), and (b) the corresponding frequency spectrum.

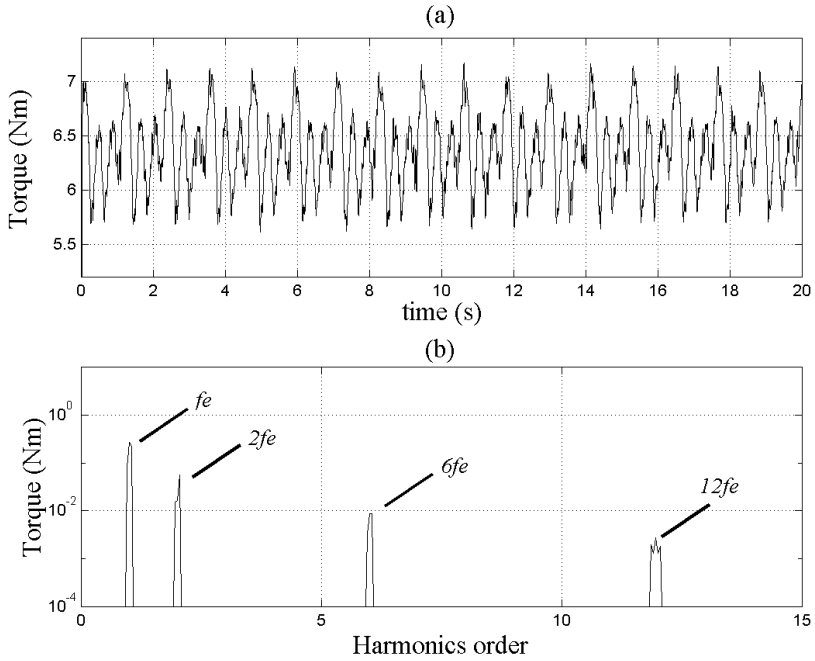

Figure 6.28: Sinusoidal current control scheme: (a) steady-state estimated torque response (TRF=18.5%), and (b) the corresponding frequency spectrum.

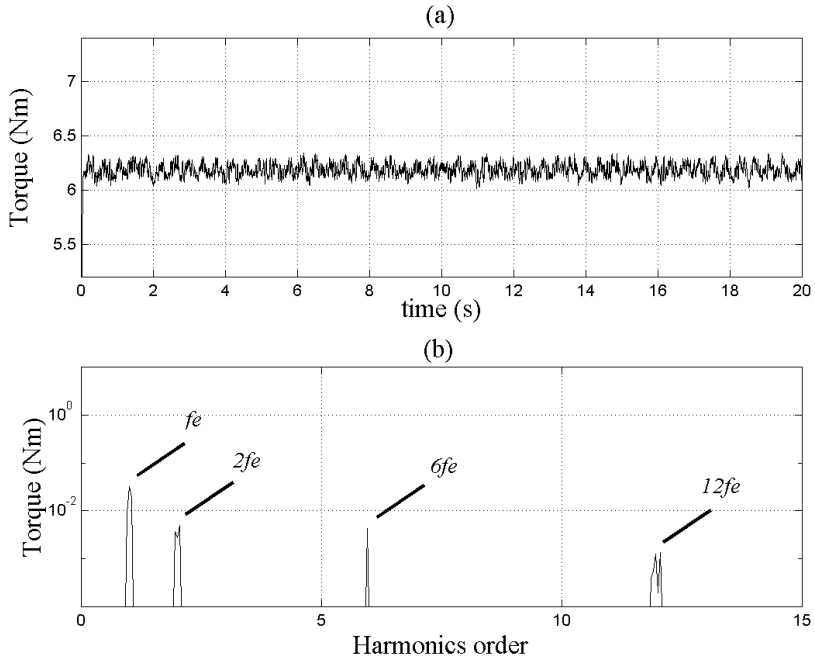

Figure 6.29: Proposed FILC torque control scheme: (a) steady-state estimated torque response (TRF=4.0%), and (b) the corresponding frequency spectrum.

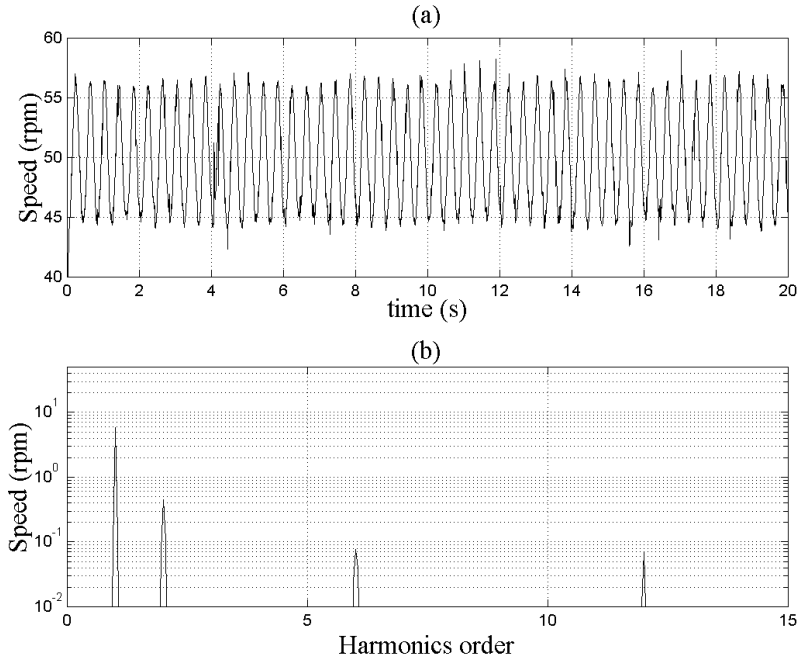

Figure 6.30: Conventional PI speed control scheme: (a) steady-state speed response (SRF=0.65%), and (b) the corresponding frequency spectrum.

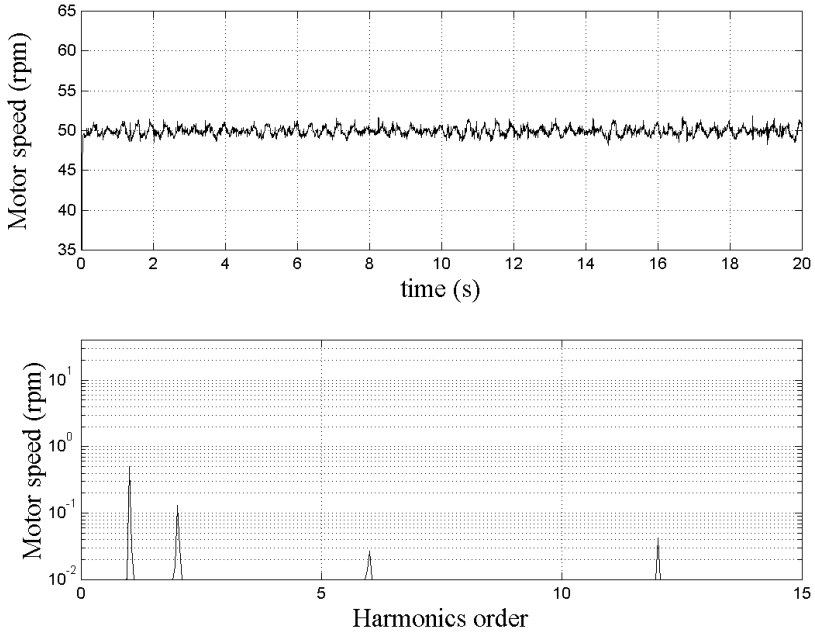

Figure 6.31: Basic ILC speed control scheme: (a) steady-state speed response (SRF=0.15%), and (b) the corresponding frequency spectrum.

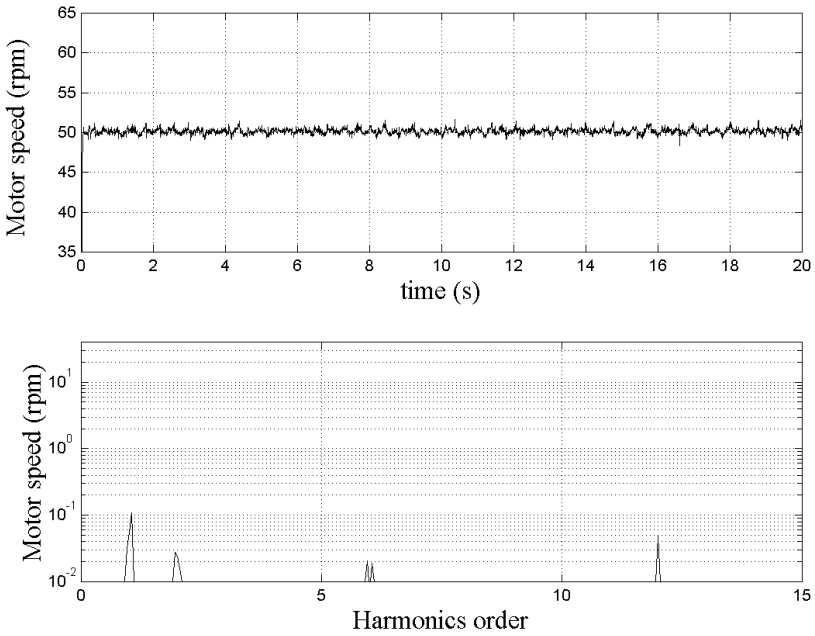

Figure 6.32: Proposed FILC speed control scheme: (a) steady-state speed response (SRF=0.10%), and (b) the corresponding frequency spectrum.

Figs. 6.33 to 6.35 are arranged in the same sequence, and the operating conditions for these figures are $\omega_m = 0.025$ p.u.(50 rpm), $\tau_L = 0.795$ p.u.(6.20 Nm). In this case, the SRF is reduced from 0.78% to 0.47% with ILC speed ripple compensation scheme and to 0.32% with FILC compensation scheme. It can be seen that again both the proposed schemes are able to compensate for the 1^{st} and 2^{nd} harmonic components to a greater extent. However, the reduction in the 6^{th} and 12^{th} components is not so considerable as that in the light load case. This is because when motor operates under heavy loads, the torque pulsations induced from the load side (DC generator) that mainly consist of non-integer multiple harmonics become greater. They are reflected back in speed ripples, which cannot be compensated by the ILC schemes due to their non-integer multiples of the fundamental frequency nature.

The numerical values of SRF under different operating speeds are shown in Fig. 6.36. The figure gives the SRFs when PMSM is operated at different speeds

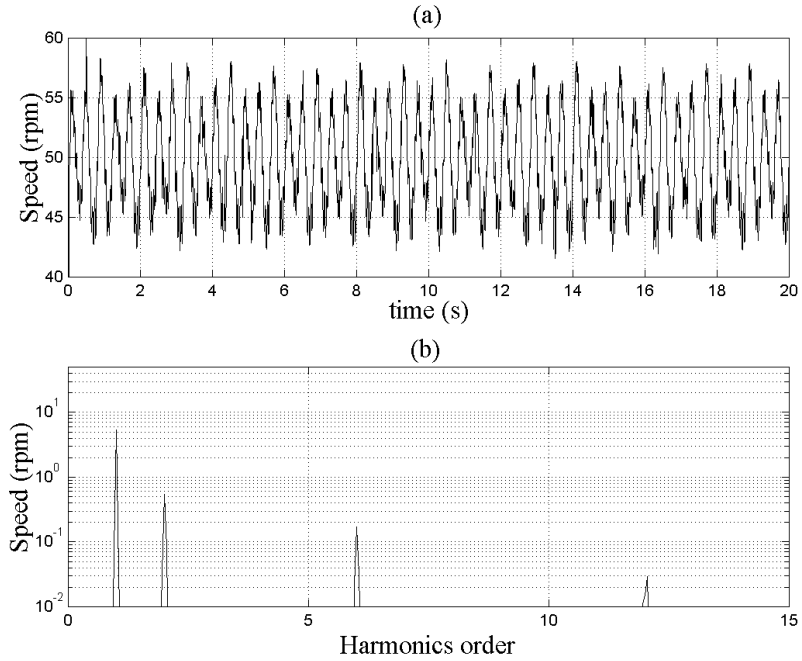

Figure 6.33: Conventional PI speed control scheme: (a) Steady-state speed response (SRF=0.78%), and (b) the corresponding frequency spectrum.

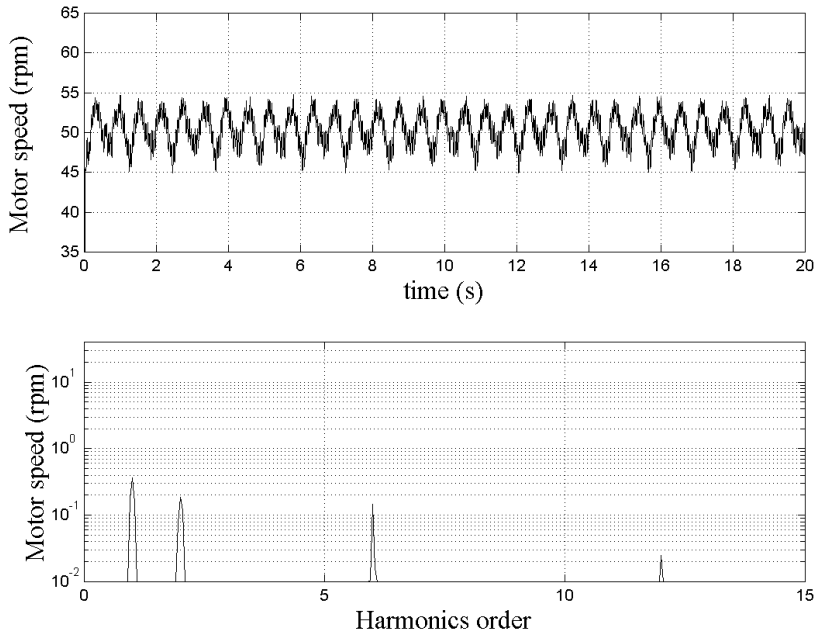

Figure 6.34: Basic ILC speed control scheme: (a) Steady-state speed response (SRF=0.47%), and (b) the corresponding frequency spectrum.

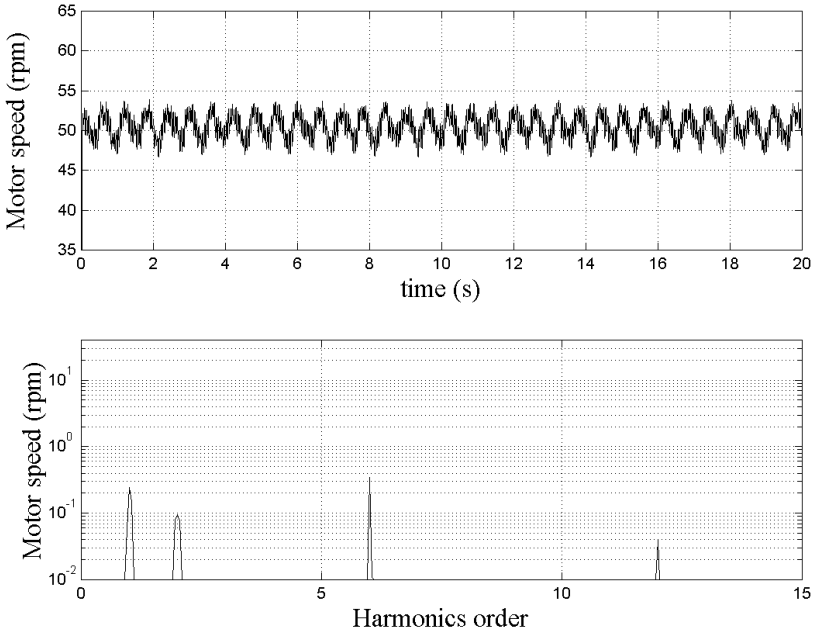

Figure 6.35: Proposed FILC speed control scheme: (a) Steady-state speed response (SRF=0.32%), and (b) the corresponding frequency spectrum.

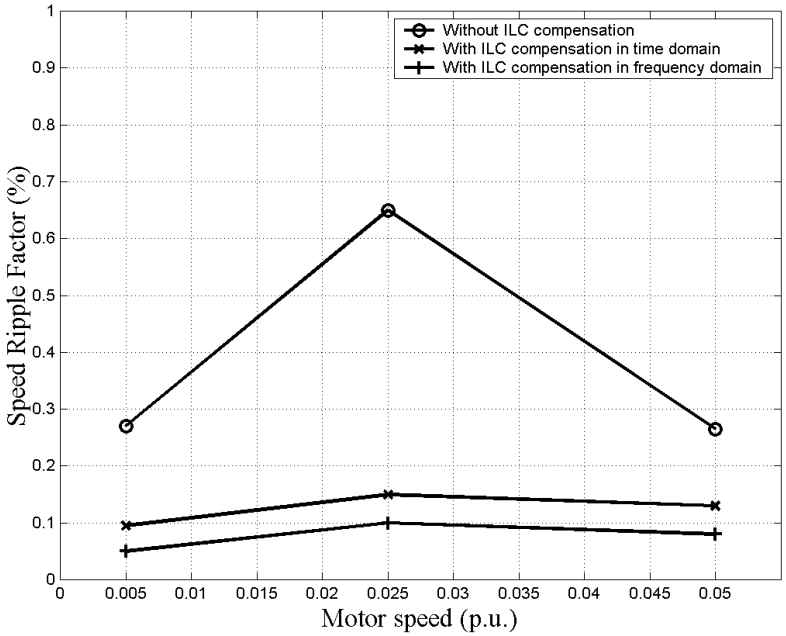

Figure 6.36: SRFs of different speeds under a light load of 1.60 Nm without, with ILC and FILC compensation.

(0.005 p.u., 0.025 p.u. and 0.05 p.u.) under a light load of 0.205 p.u.(1.60 Nm) without or with ILC/FILC compensation schemes. According to the results, the effectiveness of the proposed FILC scheme is verified in suppressing speed ripples under various steady-state operating conditions. Furthermore, it can be observed that the FILC scheme is better than the basic ILC scheme as the theory predicts. However, still there is a disadvantage in the frequency domain learning when it faces the problem caused by the existence of those non-integer harmonics induced from the load side.

6.4 Torque Pulsations Induced by the Load

It is necessary to distinguish those torque ripples caused by loading mechanism from the ones induced by the PMSM, which are of our interest. For this purpose, we decouple the PMSM from the DC machine, which is originally used as the load, excite the DC machine to work in the motoring mode at 50 rpm, and observe the torque signal by using a torque transducer. Fig. 6.37 shows the frequency spectrum of the resultant torque pulsations induced by the DC machine alone. It can be seen that some non-integer harmonics are present in the torque waveforms, among which the 0.65^{th} and 7.35^{th} harmonics are dominant. In addition, energy distributed around the 7^{th} and 8^{th} harmonics are quite apparent. Figs. 6.38 and 6.39 show the frequency spectrum of speed response without compensation under the light load and heavy load respectively. In the former figure, we can observe that the integer multiple harmonics are the most dominant components, while in the latter one, non-integer harmonics, the 0.65^{th} and 7.35^{th} components become invincible. In fact, these components are the same dominant harmonics which appear in Fig. 6.37, since they are induced by the non-ideal load mechanism when the DC machine is excited for heavy load purpose.

It should be noted that the learning control schemes are supposed to reduce

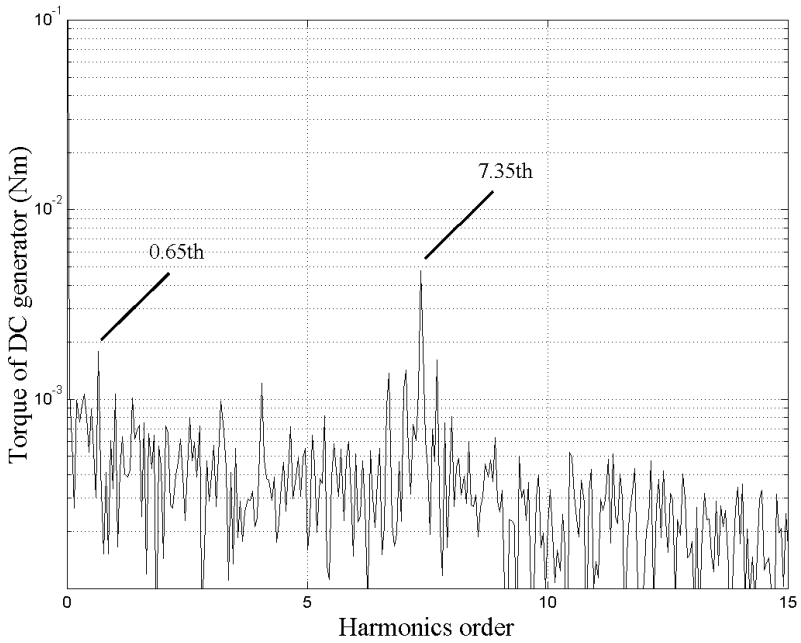

Figure 6.37: Frequency spectrum of torque pulsations induced by the DC generator.

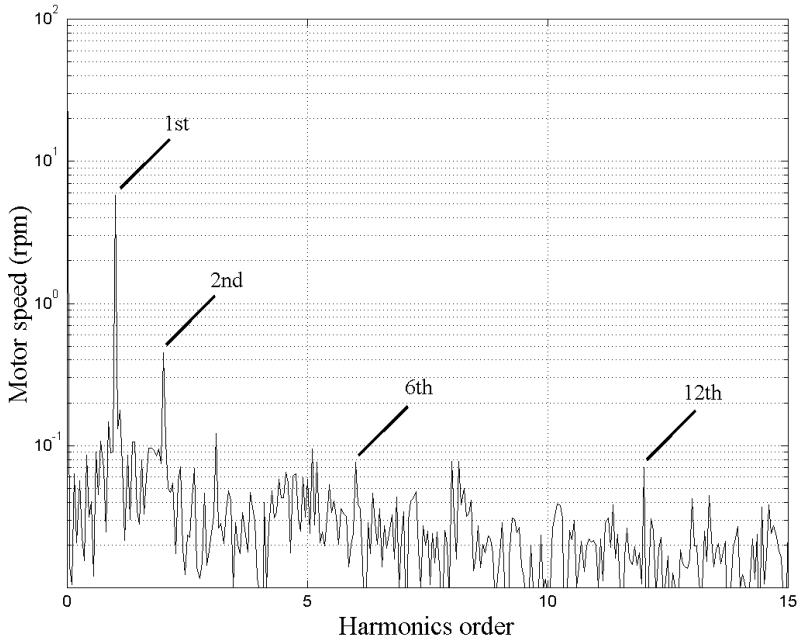

Figure 6.38: Frequency spectrum of steady-state speed response without compensation under the light load.

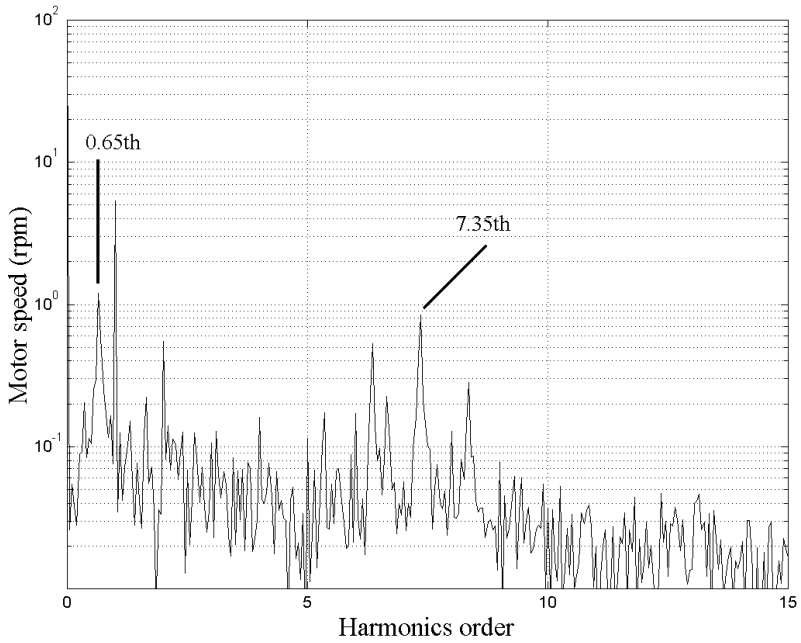

Figure 6.39: Frequency spectrum of steady-state speed response without compensation under the heavy load.

torque (or speed) harmonics, which are integer multiples of fundamental frequency. This is because ILC is designed in face of removing periodic disturbance in the input, and it has no effect on non-periodic disturbance. In our case, torque oscillations are periodic in nature. Thus, we define the time period as the basic period in the ILC schemes implementation so as to remove most of these ripples. However, those non-integer harmonics induced from the load side are ripples that do not share that basic time period with others, which makes them impossible to be eliminated by using ILC. To solve this problem, we can multiple the basic time period such that those non-integer harmonics become 'integer' in corresponding with the new period. However, this will prolong the converging time of learning process, and such method is noneffective in case of pseudo harmonics, because it is impossible to find its time period.

This non-ideal loading mechanism, namely the appearance of non-integer torque harmonics further degrades the performance of the proposed controllers,

particularly the frequency-domain learning method. Although Fourier-based learning mechanism is capable of further reduction of periodic ripples, it also induces a distorted approximation of these non-integer harmonics. Such distortion is caused by the mismatch between the time period of Fourier transformation and those of non-integer harmonics. As a result, these wrong information further induces the error accumulation during the learning process, which makes the ILC scheme implemented in frequency domain less desirable when facing the non-ideal situation of load mechanism. This also explains why the 6^{th} harmonics has been increased a little in Fig. 6.35, since the distortion of error information affects the local bandwidth and generates locally wrong control signals to compensate for the speed ripples.

6.5 Conclusion

In this chapter, experimental results obtained from a PMSM drive system are presented for the evaluation of the effectiveness of the two proposed LVSC schemes and the two proposed FILC schemes to minimize torque (or speed) ripples. In all these schemes, the performances of the proposed LVSC and FILC schemes are compared with the those of the conventional drive control schemes (torque control scheme using sinusoidal current excitation or closed-loop PI speed control) or those of the basic ILC schemes. From the experimental results, the following observations can be obtained:

- The proposed LVSC schemes and FILC schemes effectively reduce the torque and speed ripples, and improve the TRF and SRF by at least 50% as compared to those of the conventional schemes without compensation schemes.
- Frequency-domain iterative learning control schemes can further improve torque and speed ripples as compared to those basic ILC schemes, because of the elimination of forgetting factor, which is necessary for robustness in the

latter.

- While these learning control schemes effectively compensate all torque ripple disturbances that are periodic in nature, non-periodic disturbances and non-integer multiple harmonics in the torque remain largely uncompensated. The reason for this needs further investigations and have been proposed as future research work.

Chapter 7

Extended Summary and Conclusions

7.1 Conclusions

This thesis deals with a sequence of studies on application of iterative learning control strategies on pulsating torque ripple reduction of PM synchronous motors. Smooth, and ripple-free motor torque is a highly desirable feature of the PMSM drives for high-performance applications. However, PMSM drives do suffer from parasitic torque pulsations that originate from flux harmonics, cogging, current offsets, current scaling error and phase unbalancing. In this research work, two novel pulsating torque minimization schemes for the PMSM using the concepts of learning variable structure control (LVSC) and frequency-domain iterative learning control (FILC) are proposed, implemented and evaluated. Both algorithms are improvements based on iterative learning control (ILC).

A literature review of various schemes on torque ripple minimization in PMSM drives has been presented in Chapter 1. Broadly, these techniques can be divided into two different groups: (a) on the motor design aspects and the other, (b) on active control of stator current excitations. From the motor design viewpoint, skewing the stator slots and other motor design features reduce the cogging torque to a certain extent but do not completely eliminate it. Furthermore, these methods increase the complexity of the motor design and construction, making them

unacceptable for low-cost high volume production. Under the second approach of active stator currents excitation, most of the methods require sufficiently accurate priori information of the motor parameters. These may not be possible given the uniqueness of each motor due to manufacturing tolerances. From the literature review, it is can be concluded that none of the available techniques can sufficiently minimize torque ripples in the PMSM drive. Therefore, a more simple yet effective approach is required. Recognizing the effectiveness of the iterative learning control in suppressing periodic disturbances, in the face of modelling uncertainties and non-linearities, two torque controllers based on LVSC and FILC are employed to achieve torque ripple minimization.

Mathematical models of the PMSM are presented in both *a-b-c* and *d-q* reference frames in Chapter 2. The individual components in the electromagnetic torque have been clearly expressed. The motor torque comprises of the cogging torque, mutual-inductance torque, self-inductance torque and EMF torque. It is well known that EMF torque, which results from the interaction of the back-emf with the stator currents in the motor, is the main contribution to the electromagnetic torque, while the other three components are relatively insignificant in PMSMs. A mathematical model of the pulsating torque in PMSMs has also been presented. It is noted that the harmonics in the back-emf is the main cause of the torque ripples. Other sources of torque ripples include the cogging torque, and those arising from the drive scheme (termed as secondary phenomena). Those include dc offset and current scaling errors. A detailed analysis on the torque ripples are presented in Chapter 2. This research work focuses on minimizing these torque ripples so that the resulting electromagnetic torque is smooth and ripple free.

Subsequently, in Chapter 3, the concepts of the learning variable structure control (LVSC) and frequency-domain iterative learning controller (FILC) are used in the design of the proposed torque and speed controllers, to minimize the torque

and speed ripples, respectively. Two different control schemes based on either LVSC or FILC are proposed.

In the first scheme, the LVSC/FILC torque controller is applied in conjunction with the conventional open-loop torque control scheme with sinusoidal current excitation. Based on the error signal between the desired and actual motor torque, the LVSC/FILC scheme generates appropriate compensating current i^*_{qs-2} to compensate the torque ripples. As the instantaneous motor torque is required by the proposed torque controller, either a torque transducer with high-bandwidth output can be used to measure the signal or an on-line high gain torque estimator is implemented to calculate the signal.

In the second scheme, we focus our attention on speed ripples. In the above torque control scheme, instantaneous torque signals are required for feedback information, and hence either a torque transducer or a torque estimator is necessary to implement the control scheme. Such methods either increase the final cost of motor drive system or increase the complexity of the control algorithm. On the other hand, a speed ripple compensation scheme can avoid disadvantages mentioned above, and meanwhile achieve pulsating torque minimization indirectly. Furthermore, knowing that the PI speed controller is not able to completely suppress or eliminate the speed ripples, we look at the possibility of designing an additional speed controller based on the LVSC/FILC scheme which can help to suppress the speed ripples. The proposed scheme is incorporated in the speed loop and applied in parallel with the PI speed controller. Based on the error signal between the desired and actual motor speed, the LVSC/FILC scheme generates appropriate compensating current i^*_{qs-2} to compensate the speed ripples.

Having presented the LVSC and FILC schemes, simulation studies were performed as reported in Chapter 4 to investigate the effectiveness of the proposed schemes in reducing torque and speed ripples. A *d-q* model of the plant is used

in the simulation tests. Components of the torque ripples (flux harmonics, dc offsets and current scaling) are added in the simulation studies and the proposed LVSC/FILC schemes are then applied. The simulation results obtained demonstrate that in both proposed schemes, there is significant reduction in the torque and speed ripples. In general, the LVSC/FILC scheme improves the performance of the system by an order of magnitude.

To further validate the effectiveness of the proposed LVSC and FILC schemes, experimental studies were performed on a DSP-based PMSM drive setup. This experimental setup is described in Chapter 5 and experimental results are presented in Chapter 6. The experimental tests performed are over a wide range of motor operating speeds and load torques. The performances of the drive schemes using the proposed LVSC compensation are compared with those of the conventional speed or torque control schemes. While the performances of the schemes based on the FILC compensation are compared with those of the basic ILC compensation schemes. Similar with the results obtained in the simulation studies, the experimental tests show that both proposed LVSC and FILC schemes are effective in suppressing the torque (or speed) ripples. Further reduction in torque (or speed) ripples is possible by using the FILC compensation compared with the results obtained from ILC schemes. From the experimental studies, it is evident that the proposed LVSC and FILC schemes effectively improve the TRF and SRF of the conventional drive schemes by at least 50%. Furthermore, it is demonstrated that both schemes achieve minimization of the torque (or speed) ripples to an acceptable level in a reasonably short time.

It is evident from the experimental studies that while the proposed schemes effectively compensate all torque ripple disturbances that are periodic in nature, non-periodic disturbances in the torque remain largely uncompensated. Nevertheless, this is a well-known drawback of the schemes based on iterative learning

control—they can only compensate for periodic disturbances. Finally, from the experimental test results, it is apparent that the implemented LVSC and FILC algorithms are robust to measurement noise, errors in re-initialization and presence of un-modelled disturbances (that gives rise to dominant, non-periodic disturbances).

7.2 Future Work

To further improve the proposed LVSC and FILC schemes in minimizing the periodic torque and speed ripples, the following proposals are made:

1. By employing a more advanced current controller of larger bandwidth and tracking capabilities, the inner control loop can track more accurately the reference currents generated by the proposed scheme. This would enable the drive scheme employing the proposed learning compensation to work even at higher operating speeds.

2. The problem that non-periodic disturbances and harmonics with non-integer multiple of the fundamental frequency exist in the PMSM drive system can be studied. A certain controller which is capable of eliminating those harmonics can be designed and implemented together with the LVSC or FILC scheme to further reduce torque or speed ripples.

3. An adaptive learning controller where the learning gains can be adaptively changed in accordance to the magnitude of the tracking error can be included in the FILC scheme. In such schemes, at the beginning of the iteration, the learning gain can be made conservatively small so as to ensure stability. As the learning progresses, the tracking error decreases in magnitude and hence, the learning gain can be increased so as to facilitate an enhanced convergence as compared with the scheme where a fixed learning gain is employed.

4. The injection of harmonic components into drive current can reduce the rms

value of phase current. Although such reduction is slight, it still degrades the operating performance of the PMSM. A certain method is expected to solve this problem.

Bibliography

[1] T. M. Jahns and W. L. Soong, "Pulsating torque minimization techniques for permanent magnet AC motor drives - A review (Invited Paper)," *IEEE Trans. Industrial Electronics*, vol. 43, no. 2, pp. 321-330, April 1996.

[2] R. M. Crowder, "Electric drives and their controls," *Monographs in Electrical and Electronic Engineering*, Oxford Science Publications, 1995.

[3] J. Holtz, "Pulsewidth modulation for electronic power conversion," *Proc. of the IEEE*, vol. 82, no. 8, pp. 1194-1214, Aug. 1994.

[4] G. D. Sousa and B. K. Bose, "A fuzzy set theory based control of a phase-controlled converter DC machine drive," *IEEE Trans. Industry Applications*, vol. 30, no. 1, pp. 34-44, 1994.

[5] S. Weerasooriya and M. A. El-Sharkawi, "Identification and control of a DC motor using back-propagation neural networks," *IEEE Trans. Energy Conversion*, vol. 6, no. 6, pp. 663-669, 1991.

[6] F. Blaschke, "The principle of field orientation as applied to the new TRANSVEKTOR closed-loop control system for rotating-field machines," *Siemens Review*, vol. 34, pp. 217-220, May 1972.

[7] I. Takahashi and T. Noguchi, "A new quick response and high efficiency control strategy of an induction motor," in *Record IEEE Industry Applications Society Annual Meeting*, 1985, pp. 496-502.

[8] S. Rajaram, S. K. Panda and K. S. Lock, "Performance comparison of feedback linearised controller with PI controller for PMSM speed regulation," in *Proc. 1996 IEEE Power Electronics, Drives and Energy Systems for Industrial Growth Conf.*, pp. 353-359.

[9] R. Krishnan, "Selection criteria for servo motor drives," *IEEE Trans. Industry Applications*, vol. 23, no. 2, pp. 270-275, March/April 1987.

[10] P. Pillay, "Modelling, simulation and analysis of permanent magnet synchronous and brushless DC motor drives," Ph.D. dissertation, Dept. Elec. Eng., Virginia Polytechnic Institute and State University, USA, 1987.

[11] N. Mohan, T. M. Undeland and W. P. Robbins, *Power electronics*, John Wiley & Sons, 1995.

[12] I. Boldea and S. A. Nasar, *Electric drives*, CRC Press Library of Congress Cataloging-in-Publication Data, 1999.

[13] G. R. Slemon, "Electrical machines for variable frequency drives," *Proc. of the IEEE*, vol. 82, no. 8, pp. 1123-1139, Aug. 1994.

[14] M. Sagawa, S. Fujimura, N. Togawa, H. Yamamoto and Y. Matsura, "New material for permanent magnets on a base of Nd and Fe (Invited Paper)," *Journal of Applied Physics*, vol. 55, no. 6, pp. 2083-2087, March 1984.

[15] R. Gabriel, W. Leonhard and C. J. Nordby, "Field-oriented control of a standard AC motor using microprosessors," *IEEE Trans. Industy Applications*, vol. 16, pp. 186-192, Mar./Apr. 1980.

[16] N. Matsui and M. Shigyo, "Brushless DC motor control without position and speed sensors," *IEEE Trans. Industry Applications*, vol. 28, no. 1, pp. 120-127, Jan./Feb. 1992.

[17] K. Rajashekara, A. Kawamura and K. Matsuse (editors), *Sensorless control of AC motor drives*, IEEE Press, 1996, section 2, pp. 259-379.

[18] L. Chang, "Comparison of AC drives for electric vehicles - A report on experts' opinion survey," *IEEE Aerospace and Electronics Magazine*, pp. 7-11, Aug. 1994.

[19] G. R. Slemon, "High-efficiency drives using permanent magnet motors," in *Proc. 1993 IEEE Industrial Electronics, Control & Instrumentation (IECON'93)*, vol. 2, pp. 725-730.

[20] A. Cheok and N. Ertugrul, "A model-free fuzzy-logic-based rotor position sensorless switched reluctance motor drive," in *Record of IEEE Industry Applications Society Annual Meeting*, 1996, vol. I, pp. 76-83.

[21] T. M. Jahns, "Motion control with permanent magnet AC machines (Invited Paper)," *Proc. of the IEEE*, vol. 82, no. 8, pp. 1241-1251, Aug., 1994.

[22] H. Le-Huy, R. Perret and R. Feuillet, "Minimization of torque ripple in brushless DC motor drives," *IEEE Trans. Industry Applications*, vol. 22, no. 4, pp.748-755, July/Aug. 1986.

[23] J. Cros, J. M. Vinassa, S. Clenet, S. Astier and M. Lajoie-Mazenc, "A novel current control strategy in trapezoidal emf actuators to minimize torque ripples due to phase commutations," in *Proc. European Conf. Power Electronics Applications (EPE)*, Brighton, UK, vol.4, 1993, pp. 266-271.

[24] C. S. Berendsen, G. Champenois and A. Bolopion, "Commutation strategies for brushless DC motors: Influence on instant torque," *IEEE Trans. Power Electronics*, vol. 8, no. 2, pp. 231-236, April 1993.

[25] R. Carlson, M. Lajoie-Mazenc and J. Fagundes, "Analysis of torque ripple due to phase commutation in brushless DC machines," *IEEE Trans. Industry Applications*, vol. 28, no. 3, pp. 632-638, 1992.

[26] S.-J. Kang and S.-K. Sul, "Direct torque control of brushless DC motor with non-ideal trapezoidal back emf," *IEEE Trans. Power Electronics*, vol. 10, no. 6, pp. 796-802, Nov. 1995.

[27] C. French and P. Acarnley, "Direct torque control of permanent magnet drives," *IEEE Trans. Industry Applications*, vol. 32, no. 5, pp. 1080-1088, Sept./Oct. 1996.

[28] Y.-H. Kim, Y.-S. Kook and Y. Ko, "A new technique of reducing torque ripples for BDCM drives," *IEEE Trans. Industrial Electronics (Letters to the Editor)*, vol. 44, no. 5, pp. 735-739, Oct. 1997.

[29] M. Yoshida, Y. Murai and M. Takada, "Noise reduction by torque ripple suppression in brushless dc motor," in *Proc. 1998 IEEE Power Electronics Specialists Annual Conf. (PESC'98)*, vol. 2, pp. 1397-1401.

[30] Y. Sozer and D. A. Torrey, "Adaptive torque ripple control of permanent magnet brushless DC motors," in *Proc. 13th Annual Power Electronics Conference and Exposition (APEC'98)*, vol. 1, 1998, pp. 86-92.

[31] T. S. Low, "Permanent magnet motors for direct-drive applications," *Automation News*, Nov. 1987, pp. 14-17.

[32] B. H. Ng, M. F. Rahman, T. S. Low and K. W. Lim, "An investigation into the effects of machine parameters on torque pulsations in a brushless DC drive," in *Proc. IEEE Industrial Electronics, Control & Instrumentation Conf. (IECON'88)*, Oct. 1988, pp. 749-754.

[33] S. Davies and D. Chen, "High performance brushless dc motors for direct drive robot arm," *PCIM*, Aug. 1985, pp. 35-38.

[34] J. De La Ree and Jaime Latorre, "Permanent magnet machines torque considerations," in *Record of IEEE Industry Applications Society Annual Meeting*, 1988, pp. 32-37.

[35] J. De La Ree and N. Boules, "Torque production in permanent magnet synchronous motors," *IEEE Trans. Industry Applications*, vol. 25, no. 1, pp. 107-112, Jan./Feb. 1989.

[36] M. Jug, B. Hribernik, A. Hamler, M. Trlep and B. Kreca, "Investigation of reluctance torque of brushless DC motor," in *Proc. Intl. Conf. Elec. Machines*, Boston, 1990, pp. 132-137.

[37] D. C. Hanselman, "Effect of skew, pole count and slot count on brushless motor radial force, cogging torque and back emf," in *Proc. IEE Electrical Power Appl.*, vol. 144, no. 5, Sept. 1997, pp. 325-330.

[38] K. J. Binns, F. B. Chaaban and A. A. K. Hameed, "Major design parameters of a sold canned motor with skewed magnets," in *IEE Proc.*, vol. 140, no. 3, May 1993, pp. 161-165.

[39] R. Carlson, A. A. Tavares, J. P. Bastos and M. Lajoie-Mazenc, "Torque ripple attenuation in permanent magnet synchronous motors," in *Record of IEEE Industry Applications Society Annual Meeting*, 1989, pp. 57-62.

[40] Z. Q. Zhu and D. Howe, "Analytical prediction of the cogging torque in radial-field permanent magnet brushless motors," *IEEE Trans. Magnetics*, vol. 28, no. 2, pp. 1371-1374, March 1992.

[41] B. Ackermann, J. H. H. Janssen, R. Sottek and R. I. Van Steen, "New technique for reducing cogging torque in a class of brushless DC motors," in *IEE Proc.*, vol. 139, Part B, no. 4, July 1992, pp. 315-320.

[42] A. Kaddouri and H. Le-Huy, "Analysis and design of a slotless NdFeB permanent-magnet synchronous motor for direct drive," in *Record of IEEE Industry Applications Society Annual Meeting*, 1992, pp. 271-278.

[43] B. Nogarede and M. Lajoie-Mazenc, "Torque ripple minimization methods in sinusoidal fed synchronous permanent magnet machines," in *Proc. IEE Electrical Machines & Drives Conf.*, Sept. 1991, pp. 41-45.

[44] S.-K. Chang, B.-K. Kang, J.-S. Ryu, and J.-S. Seol, "The effects of the distribution of residual magnetization on the cogging torque and switching signals in permanent magnet (PM) motors," *IEEE Tran. Magnetics*, vol. 38, no. 2, pp. 1217-1220, Mar. 2002.

[45] M. Goto and K. Kobayashi, "An analysis of th cogging torque of a DC motor and a new technique of reducing the cogging torque," *Elect. Eng. in Japan*, vol. 103, no. 5, pp. 113-120, 1983.

[46] K. Kobayashi and M. Goto, "A brushless DC motor of a new structure with reduced torque fluctuations," *Elect. Eng. in Japan*, vol. 105, no. 3, pp. 104-112, 1985.

[47] C. Chan, J. Jiang, G. Chen, X. Wang and K. Chau, "A novel polyphase multipole square-wave permanent magnet motor drive for electric vehicles," *IEEE Trans. Industry Applications*, vol. 30, no. 5, pp. 1258-1266, Sept./Oct. 1994.

[48] C. Studer, A. Keyhani, T. Sebastian and S. K. Murthy, "Study of cogging torque in permanent magnet machines," in *Record of IEEE Industry Appli-*

cations Society Annual Meeting, New Orleans, Louisiana, vol. 1, Oct. 1997, pp. 42-49.

[49] A. Miraoui, L. De Fang and J. M. Kauffmann, "Performance analysis of permanent magnet brushless DC motor," in *Proc. IEE Elec. Machines & Drives Conf.*, Oxford, Sept. 1993, pp. 371-375.

[50] C. A. Borghi, D. Casadei, A. Cristofolini, M. Fabbri, and G. Serra, "Minimizing torque ripple in permanent magnet synchronous motors with polymer-bonded magnets," *IEEE Tran. Magnetics*, vol. 38, no. 2, pp. 1371-1377, Mar. 2002.

[51] B.-J. Brunsbach, G. Henneberger and Th. Klepsch, "Compensation of torque ripple," in *Proc. IEE Electrical Machines & Drives Conf.*, Oxford, Sept. 1993, pp. 588-593.

[52] C. Clenet, Y. Lefevre, N. Sadowski, S. Astier and M. Lajoie-Mazenc, "Compensation of permanent magnet motors torque ripple by means of current supply waveshapes control determined by finite element method," *IEEE Tran. Magnetics*, vol, 29, no. 2, pp. 2019-2023, Mar. 1993.

[53] E. Favre, L. Cardoletti and M. Jufer, "Permanent-magnet synchronous motors: A comprehensive approach to cogging torque suppression," *IEEE Trans. Industry Applications*, vol. 29, no. 6, pp. 1141-1149, Nov./Dec. 1993.

[54] A. P. Wu and P. L. Chapman, "Cancellation of torque ripple due to nonidealities of permanent magnet synchronous machine drives," *Proc. of IEEE 34th Annual Conferece on Power Electronics Specialist (PESC'03)*, vol. 1, June 2003, pp. 256 -261.

[55] D. C. Hanselman, "Minimum torque ripple, maximum efficiency excitation of brushless permanent magnet motors," *IEEE Trans. Industrial Electronics*, vol. 41, no. 3, pp. 292-300, June 1994.

[56] J. Holtz and L. Springob, "Identification and compensation of torque ripple in high-precision permanent magnet motor drives (Invited paper)," *IEEE Trans. Industrial Electronics*, vol. 43, no. 2, pp. 309-320, April 1996.

[57] F. Colamartino, C. Marchand and A. Razek, "Torque ripple minimization in permanent magnet synchronous servodrive," *IEEE Trans. Energy Conversion*, vol. 14, no. 3, pp. 616-621, Sept. 1999.

[58] S. J. Park, H. W. Park, M. H. Lee and F. Harashima, "A new approach for minimum-torque-ripple maximum-efficiency control of BLDC motor," *IEEE Trans. Industrial Electronics*, vol. 47, no. 1, pp. 109-114, Feb. 2000.

[59] T. S. Low, C. Bi and K. T. Chang, "Motor 'identity' - a motor model for torque analysis and control," *IEEE Trans. Industrial Electronics*, vol. 43, no. 2, pp. 285-291, April 1996.

[60] G. Ferretti, G. Magnani and P. Rocco, "Modeling, identification and compensation of pulsating torque in permanent magnet AC motors," *IEEE Trans. Industrial Electronics*, vol. 45, no. 6, pp. 912-920, Dec. 1998.

[61] T. S. Low, T. H. Lee, K. J. Tseng and K. S. Lock, "Servo performance of a BLDC drive with instantaneous torque control," *IEEE Trans. Industry Applications*, vol. 28, no. 2, pp. 455-462, March/April 1992.

[62] H. Melkote and F. Khorrami, "Torque ripple attenuation for brushless DC motors via adaptive variable structure control," in *Proc. 1998 IEEE Decision & Control Conf.*, Tampa, Florida, Dec. 1998, pp. 4640-4645.

[63] S. K. Chung, H. S. Kim, C. G. Kim and M.-J. Youn, "A new instantaneous torque control of PM synchronous motor for high-performance direct-drive applications," *IEEE Trans. Power Electron.*, vol. 13, no. 3, pp. 388-400, May 1998.

[64] V. Petrović, R. Ortega, A. M. Stanković, and G. Tadmor, "Design and implementation of an adaptive controller for torque ripple minimization in PM synchronous motors," *IEEE Trans. Power Electronics*, vol. 15, no. 5, pp. 871-880, Sept. 2000.

[65] S. O. Bogosyan and M. Gokasan, "Adaptive torque ripple minimization of permanent magnet synchronous motors for direct drive applications," in *Proc. 1995 IEEE Industry Applications Society Annual Meeting (IAS'95)*, vol. 1, 1995, pp. 231-237.

[66] S. O. Bogosyan, M. Gokasan, A. Sabanovic, "Robust-adaptive linearization with torque ripple minimization for a PMSM driven single link arm," in *Proc. 1997 IEEE Industrial Electronics, Control & Instrumentation International Conf. (IECON'97)*, vol. 1, Nov. 1997, pp. 9-14.

[67] B. H. Lam, S. K. Panda and J.-X. Xu, "Reduction of Periodic Speed Ripples in PM Synchronous Motors using Iterative Learning Control," in *Proc. IEEE Intl. Conf. Industrial Electronics, Control & Instrumentation (IECON'2000)*, Nagoya, Japan.

[68] T. S. Low, K. J. Tseng, T. H. Lee, K. W. Lim and K. S. Lock, "Strategy for the instantaneous torque control of permanent-magnet brushless DC drives," in *IEE Proc.*, vol. 137, Part B, no. 6, Nov. 1990, pp. 355-363.

[69] H.-J. Gutt, F. D. Scholl and J. Blattner, "High precision servo drives with DSP-based torque ripple reduction," in *Proc. of the 4th IEEE AFRICON (AFRICON'96)*, vol. 2, Sept. 1996, pp. 632-637.

[70] K.-Y. Cho, J.-D. Bae, S.-K. Chung and M.-J. Youn, "Torque harmonics minimisation in permanent magnet synchronous motor with back emf estimation," in *Proc. IEE - Electrical Power Appl.*, vol. 141, no. 6, Nov. 1994, pp.323-330.

[71] V. Petrovic, R. Ortega, A. M. Stankovic and G. Tadmor, "An adaptive controller for minimization of torque ripple in PM synchronous motors," in *Proc. 1998 IEEE Power Electronics Specialists Conf. (PESC'98)*, vol. 1, 1998, pp. 113-118.

[72] N. Matsui, T. Makino and H. Satoh, "Autocompensation of torque ripple of direct drive motor by torque observer," *IEEE Trans. Industry Applications*, vol. 29, no. 1, pp. 187-194, Jan./Feb. 1993.

[73] F. Parasiliti, R. Petrella and M. Tursini, "Torque ripple compensation in permanent magnet synchronous motors based on Kalman filter," in *Proc. IEEE International Symposium on Industrial Electronics (ISIE'99)*, vol. 3, 1999, pp. 1333-1338.

[74] J. Zhao, M. J. Kemper and F. S. van der Merwe, "On-line control method to reduce mechanical vibration and torque ripple in reluctance synchronous machine drives," in *Proc. 1997 IEEE Industrial Electronics, Control & Instrumentation Conf. (IECON'97)*, vol. 1, pp. 126-131.

[75] J.-W. Choi, S.-S. Lee, S.-Y. Yu and S.-J. Jang, "Novel periodic torque ripple compensation scheme in vector controlled AC motor drives," in *Proc. of the*

13th Annual IEEE Applied Power Electronics Conference (APEC'98), vol. 1, 1998, pp. 81-85.

[76] A. Stotsky and I. Kolmanovsky, "Simple unknown input estimation techniques for automotive applications," in *Proc. of the 2001 American Control Conf.*, June 2001, Arlington, VA, vol. 5, pp. 3312-3317.

[77] P. C. Krause and O. Wasynczuk, *Electromechanical motion devices*, New York: McGraw-Hill Book Co., 1989.

[78] P. C. Krause, *Analysis of electric machinery*, New York: McGraw-Hill Book Co., 1987.

[79] R. P. Deodhar, D. A. Staton, T. M. Jahns and T. J. E. Miller, "Prediction of cogging torque using the flux-mmf diagram technique," in *Record of the 30th IEEE Industry Applications Meeting (IAS'95)*, vol. 1, 1995, pp. 693-700.

[80] D.-W. Chung and S.-K. Sul, "Analysis and compensation of current measurement error in vector-controlled AC motor drives," *IEEE Trans. Industry Applications*, vol. 34, no. 2, pp. 340-345, March/April 1998.

[81] D. Antic, J. B. Klaassens and W. Deleroi, "Side effects in low-speed AC drives," *Record of IEEE 25th Annual Power Electronics Specialists' Conference (PESC'94)*, vol. 2, 1994, pp. 998-1002.

[82] S. Arimoto, S. Kawamura and F. Miyazaki, "Bettering operation of dynamic systems by learning: A new control theory for servo mechanism and mechatronics systems," in *Proc. of the 23rd IEEE Conf. on Decision and Control*, Las Vegas, NV, 1984, pp. 1064-1069.

[83] S. Kawamura, F. Miyazaki and S. Arimoto, "Realization of robot motion based on a learning method," *IEEE Trans. Systems, Man, and Cybernetics*, vol. 18, no. 1, pp. 126-134, Jan./Feb. 1988.

[84] K. L. Moore, M. Dahleh and S. P. Bhattacharyya, "Iterative learning for trajectory control," in *Proc. of the IEEE 28th Conf. on Decision and Control*, Tampa, Florida, Dec. 1989, pp. 860-865.

[85] S. S. Garimella and K. Srinivasan, "Application of iterative learning control to coil-to-coil control in rolling," *IEEE Trans. Control Systems Technology*, vol. 6, no. 2, pp. 281-293, March 1998.

[86] Y. Chen, J. -X. Xu, T. H. Lee and S. Yamamoto, "An iterative learning control in rapid thermal processing," in *Proc. of the IASTED Intl. Conf. on Modeling, Simulation and Optimization (MSO'97)*, Singapore, 1997, pp. 189-192.

[87] Z. Bien and J.-X. Xu, *Iterative learning control—analysis, design, integration and applications*. Boston: Kluwer Academic Publishers, 1998.

[88] S. Arimoto, T. Naniwa and H. Suzuki, "Robustness of P-type learning control with a forgetting factor for robotic motions," in *Proc. of the 29th IEEE Conf. on Decision and Control*, Honolulu, Hawaii, Dec. 1990, pp. 2640-2645.

[89] J.-X. Xu and W.-J. Cao, "Learning variable structure control approaches for repeatable tracking control tasks," *Automatica*, vol. 37, issue 7, pp. 997-1006, July 2001.

[90] Y. Nanjo and S. Arimoto, "Experimental studies on robustness of a learning method with forgetting factor for robotic motion control," in *Proc. of the 5th IEEE Intl. Conf. on Advanced Robotics (ICAR'91)*, vol. 1, 1991, pp. 699-704.

[91] S. Arimoto, T. Naniwa and H. Suzuki, "Selective learning with a forgetting factor for robotic motion control," in *Proc. of the IEEE Intl. Conf. on Robotics and Automation*, Sacramento, California, vol. 1, April 1991, pp. 728-733.

[92] K. H. Lee and Z. Bien, "Initial condition problem of learning control," in *IEE Proc. - D*, vol. 138, no. 6, Nov. 1991, pp. 525-528.

[93] S. Boming, "An iterative learning control," M.Eng. thesis, Dept. Elect. Eng., National University of Singapore, 1997.

[94] J.-X. Xu, W.-J. Cao, "Learning variable structure control approaches for repeatable tracking control tasks," *Automatica*, vol. 37, issue 7, pp. 997-1006, July 2001.

[95] S. Wade, M. W. Dunnigan and B. W. Williams, "Simulation of induction machine vector control and parameter identification," in *Proc. of the 5th Intl. Conf. on Power Electronics and Variable-Speed Drives*, London, UK, Oct. 1994, pp. 42-27.

[96] B. H. Lam, "Torque Ripples Minimization in PMSM Drive," M.Eng. thesis, Dept. Elect. & Comp. Eng., National University of Singapore, 2001.

[97] dSPACE, *Floating-Point Controller Board - DS1102, User's Guide*, v.3.3.1, 1996.

[98] Z.-H. Liang, "Sliding-Mode Control of Induction Motor Servo Drive," M.Eng. thesis, Dept. Elect. & Comp. Eng., National University of Singapore, 1999.

[99] dSPACE, *COCKPIT - Instrument Panel, User's Guide*, v.3.3.1, 1996.

[100] Texas Instruments, *TMS320C31 - User's Guide*, 1998.

List of Publications

1. "Periodic speed ripples minimization in PM synchronous motors using repetitive learning variable structure control," in *Proc. of the 4th Asian Control Conference (ASCC 2002)*, Sept. 2002, Singapore, pp. 1670-1675.

2. "Reduction of periodic torque ripples in PM synchronous motors using learning variable structure control," in *Proc. of the 28th Annual Conference of the IEEE Industrial Electronics Society (IECON'02)*, vol. 2, Nov. 2002, pp. 1032-1037.

3. "Periodic speed ripples minimization in PM synchronous motors using repetitive learning variable structure control," *Instrumentation, Systems and Automation Society (ISA) Trans.*, vol. 42, no. 4, pp. 605-614, Oct. 2003.

4. "Periodic torque ripples minimization in PMSM using learning variable structure control based on a high gain torque observer," accepted for presentation by *the 29th Annual Conference of the IEEE Industrial Electronics Society (IECON'03)*, Apr. 2003.

5. "Torque ripple minimization in PM synchronous motors using iterative learning control," accepted for publication by *IEEE Trans. Power Electronics*, May 2003.

6. "Speed ripple minimization in PM synchronous motors using iterative learning control," conditionally accepted for publication by *IEEE Trans. Energy*

Conversion, May 2003.

7. "Torque ripples reduction in PMSM using frequency-domain ILC based on a high gain torque estimator," accepted for presentation by *the 5th International Conference on Power Electronics and Drive Systems (PEDS'03)*, June 2003.

8. "Periodic torque ripples minimization in PMSM using learning variable structure control based on a high gain torque observer," submitted for review to *IEE Proc. Electric Power Applications*, May 2003.

Appendix A

Motor Ratings and Parameters

1. **PMSM Ratings**

Table A.1: Ratings of the PMSM used in this research work

PMSM model: control techniques surface mounted type E	
Rated power (kW)	1.64
Rated speed (rpm)	2000
Rated voltage (line-to-line V_{rms})	380 - 480
Rated current (A_{rms})	3.25

2. **Parameters of the PMSM**

Table A.2: Parameters of the PMSM used in this research work

Parameter	**Value**
Stator resistance (Ω/phase)	2.125
Stator inductance (mH/phase)	11.6
Total inertia (PMSM rotor + DC motor rotor) ($kg{\cdot}m^2$)	0.0025
Viscous coefficient of friction ($Nm/(rad{\times}s^{-1})$)	0.001

3. DC Motor Ratings and Parameters

Table A.3: Ratings and parameters of the DC motor used in this research work

DC motor model: Leroy Somer TYP MF 112	
Power (kW)	2.2
Speed (rpm)	2400
Armature voltage (V_{dc})	180
Armature current (A_{dc})	14
Field voltage (V_{dc})	190
Field current (A_{dc})	0.58

Appendix B

Architecture of DS1102

As shown in Fig. B.1, the DS1102 controller board contains a main DSP TMS320C31, a slave DSP TMS320P14 based digital I/O subsystem, a 4-channel A/D converter, a 4-channel D/A converter and a 2-channel incremental encoder interface. The main DSP executes the computation in the user-programs at a frequency of 60 MHz. All the inputs and outputs of the above peripheral devices are contained in the I/O connector of the board.

The DS1102 board is built around the Texas Instruments TMS320C31 floating-point DSP. It contains 128K words memory fast enough to allow zero wait state operation. Several peripheral subsystems are implemented to support a wide range of digital signal processing applications.

The TMS320C31 supports a total memory space of 16M 32-bit words including program, data, and I/O space. All off-chip memory and I/O can be accessed by the host even while the DSP is running thus allowing easy system setup and monitoring.

The DS1102 hardware is designed for flexible use at minimum program overhead by implementing functions in hardware otherwise often performed by software. The host interface contains a bus-width converter mapping two 16-bit host accesses into a single 32-bit transfer ont eh DSP-bus to avoid data transfer inconsistencies. Detailed description on the board and its connectors are given in *dSPACE* User's Guide "Floating-Point Controller Board - DS1102".

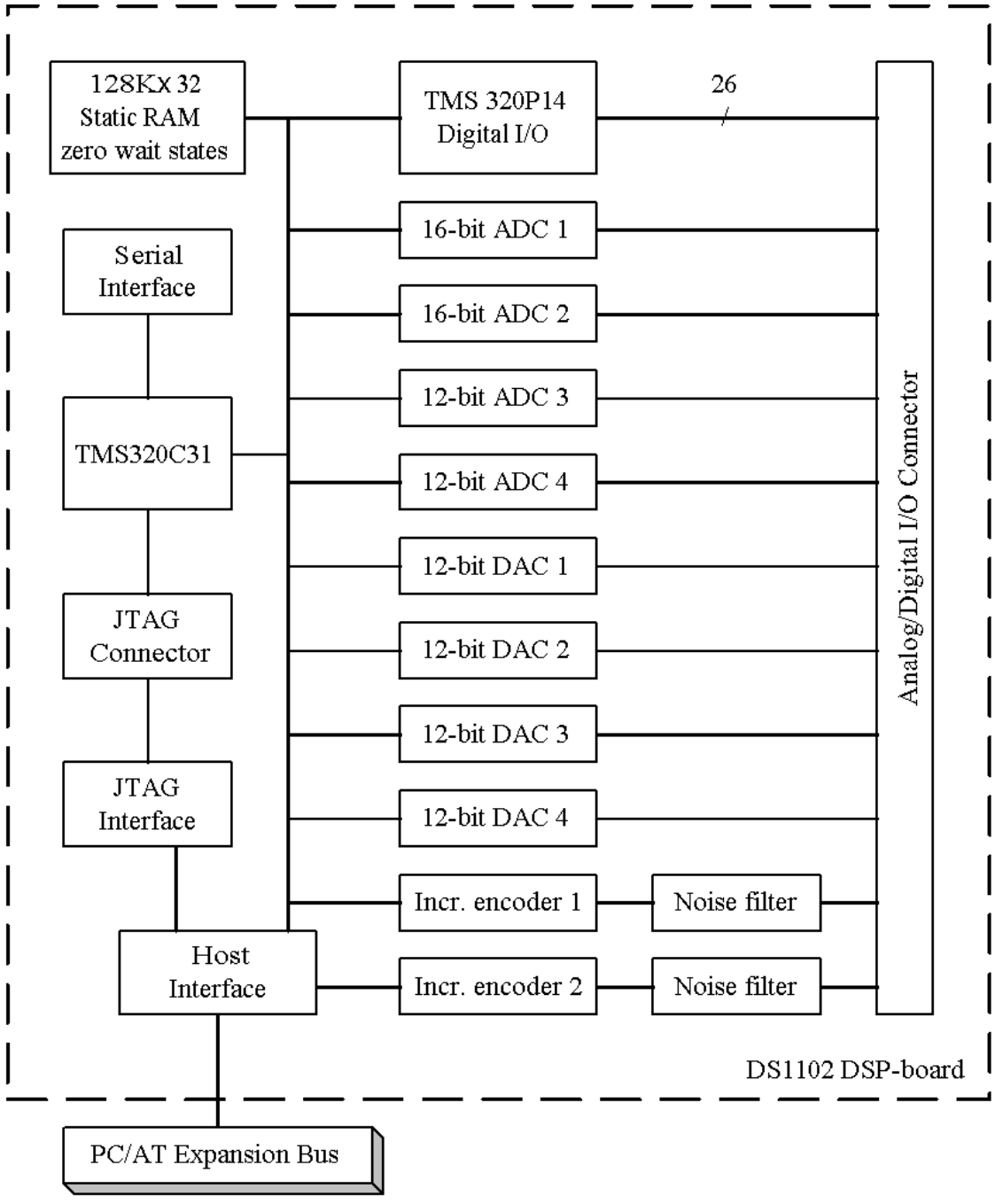

Figure B.1: Architecture of DSP DS1102 controller board.

Appendix C

Inverter

1. **Specifications**

   - **Input**: 3-phase, 380-415 V, 50-60 Hz
   - **Output**: 3-phase, 0-380/415 V
   - **Power**: up to 2.2 kW (3 HP)

2. **Description**

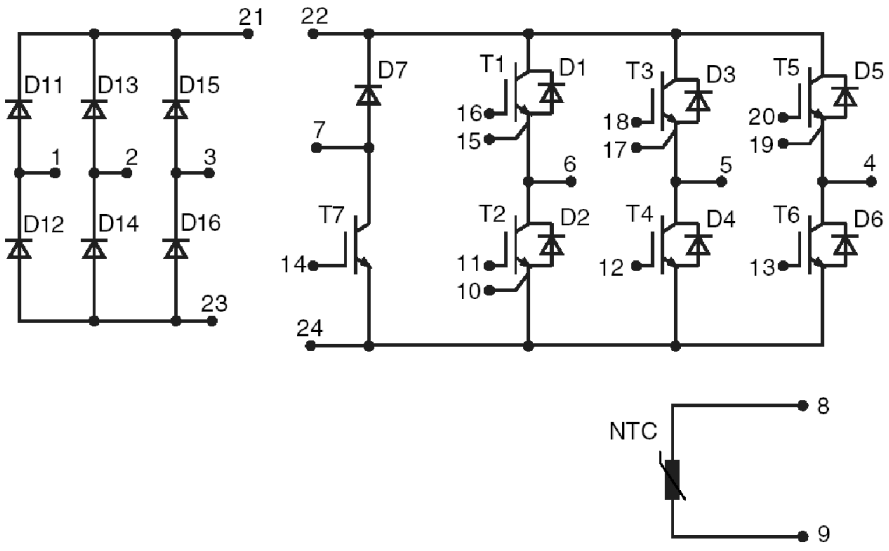

Figure C.1: Schematic diagram of MUBW 10-12A7.

- **IGBT module–MUBW 10-12A7 (IXYS)**

  The IGBT module comprises a 3-phase uncontrolled rectifier, six IGBT switches, one IGBT for braking and a built-in NTC thermistor for temperature sensing.

- **DC-link capacitors & transformer board**

  Fig. C.1 shows the schematic diagram of IXYS module. The DC-link capacitor is connected across pins 22-23. An NTC thermistor is connected in between pins 21-22 to limit the in-rush current. A low ohmic shunt is connected in between pins 23-24 for over-current sensing. Two resistor are connected in series across pins 22-24 as a voltage divider for over-voltage sensing. The transformers are powered from single-phase mains and provide floating power sources to the driver board.

- **Driver board**

  The driver board comprises voltage regulators (78L15), opto-couplers (HCPL4503, H11L1), gate drivers (TC4429), braking control and protection circuits. The connections in between the driver board and the IGBT module or transformer board are made by wires of twisted pairs. The driver board is connected with the Control-PWM Card via a shield flat-ribbon cable.

Appendix D

Interface Platform

The interface platform is built in between the DSP card and motor section and it is named as "racking system". Control signals from the DSP card and feedback signals from the motor section are processed and buffered through this racking system.

The racking system comprises the following:

1. An industrial 19" rack

   The rack is a 19" industrial standard rack made of aluminum. It is equipped with card guides and is used with Euro cards (160 mm×100 mm).

2. A set of Euro cards including a Digital-I/O Card, a Control-PWM Card and three or four Analog-signal Cards

   - *Digital-I/O Card*

     It buffers the digital I/O signals from the DSP card and distributes them to other cards, or buffers the signals from the absolute encoder.

   - *Control-PWM Card*

     It processes the PWM signals from the DSP card, transfers them to the inverter and receives the Fault signal from the inverter.

   - *Analog-signal Card*

     It processes the analog feedback signals from the drive section, filters out the noise, amplifies the signal and buffers it for the DSP card.

3. An Euro-card power supply

   The Euro-card power supply is powered from mains and provides +5 V and ±12 V for the digital and analog circuitry on the cards.

4. A back-plan PCB

   All the Euro cards share the digital I/O signals, +5 V and ±12 V power sources via the back-plane PCB.

Appendix E

Current Sensor

The sensor box is an aluminum case with a general sensor board installed inside. It is placed in between the inverter and the PMSM for measuring the motor currents. Two current sensors are mounted on the board for measuring the phase-a and -b currents. Current sensors are LEM PCB-mounted sensors. Their primary sides are connected with the output terminals of the inverter through a shielded cable. One end of the cable is soldered on the sensor board and the other is plugged in the output terminals of the inverter. On the secondary side of the sensors, measurement outputs are converted to voltage signals through resistors and then connected to the insulated BNC connectors via wires of twisted pairs. The sensor board has its own ± 15 V power source which is powered from single-phase mains.

Table E.1: Parameters of current sensors.

Part No.	Current Ratio (Pri/Sec)	Resistor on Primary-side	Resistor on Secondary-side
LA25-NP	1 A/1 mA	None	300 Ω

Appendix F

Torque Transducer

In the experimental investigations, an MCRT® 49001V(1-2)-CFA-15000 non-contact dc operated torque transducer is used.

When installed between a driver and its load, dc operated torquemeters measure be-directional static (stall) and dynamic shaft torque. Torque sensing employs field proven, strain gage technology. A corrosion resistant, one-piece stainless shaft is gaged with one or more bridges. The bridge measures torque and cancels signals from bending and thrust loads. Careful temperature compensation eliminates zero, span and calibration drift.

Rotary transformers connect the rotating gages to stationary, dc-to-dc torquemeter circuitry. They provide high quality non-contact signal coupling to the rotating gages. Rotary transformers don't generate noise or wear. They are immune to ambient noise, vibration, lubricants and other hostile environments.

RFI shielded circuitry and the 5-volt output provide high noise immunity. Simple cabling yields calibration and balance truly free of cable effects. There are no slip rings, brushes, radio transmitters and other limited-life, noise-generating elements. Their elimination further increases performance and reliability. Moreover, the robust, non-ferrite design suits these torquemeters for diesel and other hostile environments.

The following table lists condensed specifications of the torque transducer used in our experimental work.

Table F.1: Specifications of torque transducer.

Non-linearity (% of full scale)	±0.07
Hysteresis (% of full scale)	±0.07
Non-repeatability (% of full scale)	±0.03
Output tracking (% of full scale)	±0.05
Clockwise torque (full scale output)	+5 V
Counterclockwise torque (full scale output)	-5 V
Minimum resistive load (full scale output)	10 kΩ
Maximum capacity load (full scale output)	0.05 μF
Electrical over-range (% of full scale)	±40
Bandwidth	high freq. output: dc to 500 Hz
	low freq. output: dc to 1 Hz
Zero control range (% of full scale)	±5
Span control range (% of full scale)	±5
Supply voltage	11 to 26 Volts dc
Supply current	40 mA
Torque range	11.3 Nm
Torque overload	45.2 Nm
Speed rating	0 to ±15,000 rpm
Shaft stiffness	2418.2 Nm/rad

Appendix G

System commissioning

Off-line determinations of the system parameters that are required for the experimental studies are performed. Parameters such as motor inertia, damping coefficient, optimal proportional and integral gains of the PI current and speed controllers are evaluated. The following briefly describes the results of these off-line systems commissioning on the PMSM drive.

1. **Current controller**

   Using the method of iteration (trial and error), the PI current controller gains that produce satisfactory transient and steady-state current tracking are determined. The finalized P and I gains are 40 and 800, respectively, for both d- and q-axes current controllers.

2. **Speed controller**

   Using the same method as in the current controller, the P and I gains are for the speed controller are determined, and the values are 0.035 and 0.35, respectively.

3. **System time constant**

   The PMSM drive is fed with a reference torque signal, which is equal to the rated torque. Under open-loop condition, the motor is allowed to accelerate to the rated speed. The system time constant is then evaluated as the time taken for the motor to acquire a speed of (1-e^{-1}) or 63.2% of the rated speed

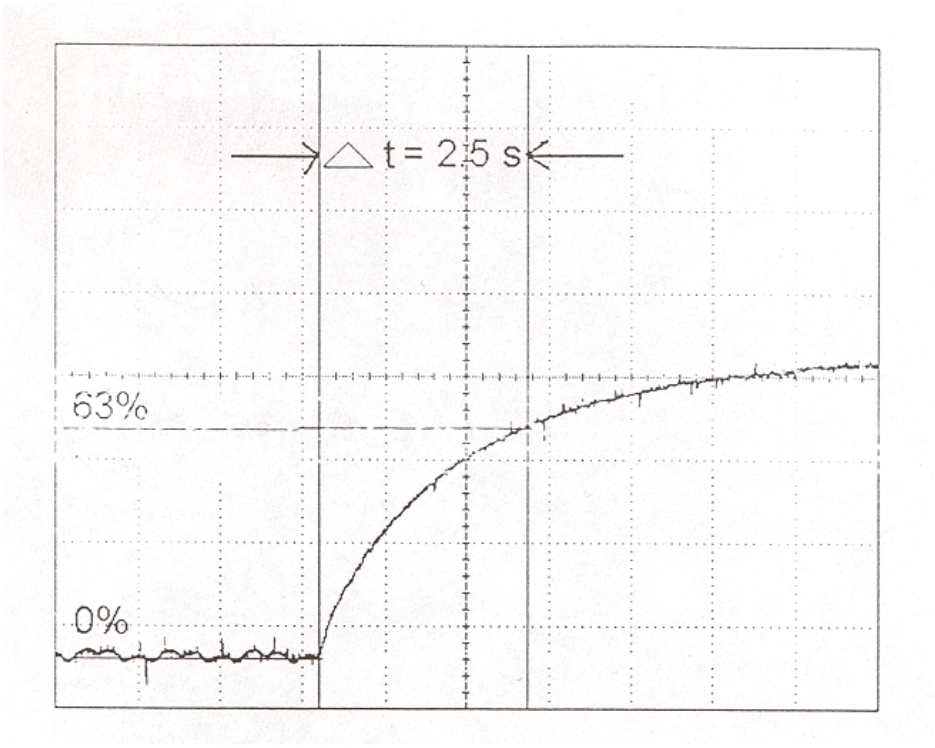

Figure G.1: Speed response of the PMSM following a step input of rated torque. Time constant, $\tau_c = \Delta t$=2.5 s (x-axis:1 s/div, y-axis:500 rpm/div).

from the start of the acceleration. Fig. shows the motor speed response under the rated torque. From the figure, time constant, $\tau_c = 2.5$ s.

4. **Coefficient of friction**

   The motor is operated as different speeds, under no-load torque condition. The motor torque signal corresponding to each operating speed is plotted as a function of the motor speed (i.e. x-axis: motor speed in rads^{-1} and y-axis: motor torque in Nm). From the gradient of the torque-speed relationship, the coefficient of friction, B, is determined as 0.001 Nm/rads^{-1}.

5. **System (rotor and load) inertia**

   From the determined values of time constant, τ_c, and frictional coefficient, B, the system inertia can be determined from the equation:

$$\tau_c = J/B \quad \Rightarrow \quad J = B\tau_c = 0.0025\ kgm^2. \tag{G.1}$$